Proton Transfer in Hydrated Molecular Ions

By

Kaye Andrea Archer

BS Applied Physics, Armstrong Atlantic State University, 2010

BS Mathematical Sciences, Armstrong Atlantic State University, 2010

Submitted to the Graduate Faculty of

The Dietrich School of Arts and Sciences in partial fulfillment

of the requirements for the degree of

Doctor of Philosophy

University of Pittsburgh

2019

UNIVERSITY OF PITTSBURGH

DIETRICH SCHOOL OF ARTS AND SCIENCES

This dissertation was presented

by

Kaye Andrea Archer

It was defended on

July 10, 2019

and approved by

Daniel S. Lambrecht, Assistant Professor, Department of Chemistry

Sean Garrett-Roe, Associate Professor, Department of Chemistry

John A. Keith, Assistant Professor, Department of Chemical and Petroleum Engineering

Dissertation Director: Kenneth D. Jordan, Richard King Mellon Professor and Distinguished Professor of Computational Chemistry, Department of Chemistry

Proton Transfer in Hydrated Molecular Ions

Kaye A. Archer, PhD

University of Pittsburgh, 2019

In this work I employ quantum and mixed quantum mechanical/molecular mechanical techniques to describe proton transfer in solvated molecular ions. I explore the role of solvation in facilitating proton-coupled electron transfer in pyridine·$(H_2O)_{n}^{-}$. The underlying physics which accounts for the differences observed in the N−H region of the infrared spectra of pyridine · $(H_2O)_{n=3}^{-}$ when compared to the $n \geq 4$ clusters, is also explored. Theoretical challenges encountered when calculating one-dimensional potential energy surfaces are examined. The merits of mapping the potential energy surface of $H^+(H_2O)_{21}$ by employing the multistate empirical valence-bond model are evaluated by calculating isomerization pathways.

Table of Contents

List of Tables

List of Figures

List of Equations

Preface

I would like to thank Dr. Kenneth D. Jordan for patience and guidance, my fellow group members as well as the SAM team both past and present for informative conversions and suggestions. I would like to thank Dr. George C. Shields who started me down the computational chemistry path in the first place and Dr. Reña Robinson for support over my PhD experience.

For my family:

Rickford, Ingrid, Camille, Kim, Crystal, Deane, Dominick, Samalexis & Sammy

Especially Dad & Mom: you dreamt more for me than I could

My sisters & brother: you were the 'wind beneath my wings'

You are my heart and soul

1.0 Introduction

Water is ubiquitous in nature and acts as a solvent in many reactions. One such reaction is proton transfer. Proton transfer features in many areas of chemistry and biology such as acid–base chemistry, electrolyte chemistry, atmospheric chemistry, macromolecular assembly such as in proteins and DNA, and in microbiological systems such as in mitochondrial respiration, ATP biosynthesis and enzyme catalysis. Proton transfer in these areas is influenced by the solvent water molecules hydrating the molecules and/or molecular ions which feature in these reactions. The solvent water molecules form a hydrogen-bond network. This network provides pathways for proton transfer to occur.

Calculations of proton transfer in molecular gas phase ions are presented in this thesis. Energy differences, such as electron affinities and barrier heights, are leveraged extensively in this work since it dictates the chemistry of the hydrated molecular ions. Electron affinities are employed to determine whether changes in the nature of the anion has occurred. The mobile proton allows diabatic states that depend on the location of the excess proton to be sampled. State mixing can be expected. In Chapter 3.3.0, this features in the potential energy surface as an avoided crossing. In the studies presented in Chapter 2.0 and 3.3.0, proton-coupled electron transfer occurs between the waters hydrating the pyridine anion forming $C_5H_6N–H\cdot OH^{-}\cdot(H_2O)_n$. To determine how proton transfer impacts the nature of the ground state anion in pyridine–water cluster anions, the nature of the ground and excited anionic states of the molecular clusters were considered. Molecular anions considered in this work are of two types – valence-bound and dipole-bound. Evolution of the anion is observed along the proton transfer coordinate. The excess electron is first

bound in the dipole field of the pyridine and hydrating water molecules, then it becomes valence-bound occupying a π^* orbital of the pyridine molecule.

Typically, potential energy curves are employed to demonstrate changes to a chemical system over a coordinate of interest. Utilizing post-Hartree-Fock theories to generating potential energy curves presents a challenge. The difficulty occurs in the neighborhood of avoided crossings where the energy difference between electronic states is small. Consequently, wavefunction convergence is difficult. In the neighborhood of the avoided crossing, two electronic configurations are possible due to a narrow energy separation. Hartree-Fock [1–3] is a single reference method which post-Hatree-Fock methods employ as an initial approximation to which electron correlation is added. Therefore, if the Hartree-Fock guess is incorrect post HF treatments will inherit this error. We therefore employ equation-of-motion electron affinity coupled-cluster singles doubles (EOM-EA-CCSD) [4,5] theory which circumvents the difficulties encountered at avoided crossings and recovers the requisite electron correlation needed to accurately model dipole-bond anions.

In Chapter 4.0, we calculate isomerization pathways for $H^+(H_2O)_{21}$. We assume that proton transfer can feature in high-energy $H^+(H_2O)_{21}$ isomerization pathways. Therefore, a model allowing protons to be associated with different water monomers is employed. Isomerization pathways are calculated to determine the accuracy of the model. There are several approaches for calculating minimum energy pathways which include the calculation of the Hessian, either directly or by employing quasi-Newton techniques [6], which partially construct an approximate inverse Hessian via a recursive algorithm. Another approach is to employ nudged elastic band (NEB) [7,8]. NEB is a chain-of-states approach that discretizes the reaction pathway. It employs quasi-Newtonian methods to converge configurations along the pathway in order to identify stationary

point corresponding to transition and intermediate states. Mapping out the $H^+(H_2O)_{21}$ potential energy surface is computationally expensive (though not prohibitively so) due to the complexity of the potential. In Chapter 4.0 the multistate empirical valence-bond model (MS-EVB) [9,10] is employed to study $H^+(H_2O)_{21}$.

This thesis is laid out in the following manner: the rest of the introduction will serve as an overview of approximations for solving the Schrodinger equation mentioned in the text. Chapter 2.0 will focus on proton-coupled electron transfer in pyridine – water anions and Chapter 3.3.0 will explore the challenges to theory this chemical system presents. Chapter 4.4.0 will focus on the challenges encountered by employing the MS-EVB method to calculate minimum energy isomerization pathway between protonated water twenty-one isomers and evaluates the usefulness of the MS-EVB model for mapping the $H^+(H_2O)_{21}$ potential energy surface.

1.1 Approximations to Schrodinger Equation

There are two representations at the disposal of the computational chemist, in increasing order of computational cost and complexity, they are the adiabatic and diabatic representation each with its own merit based on the potential energy feature of interest.

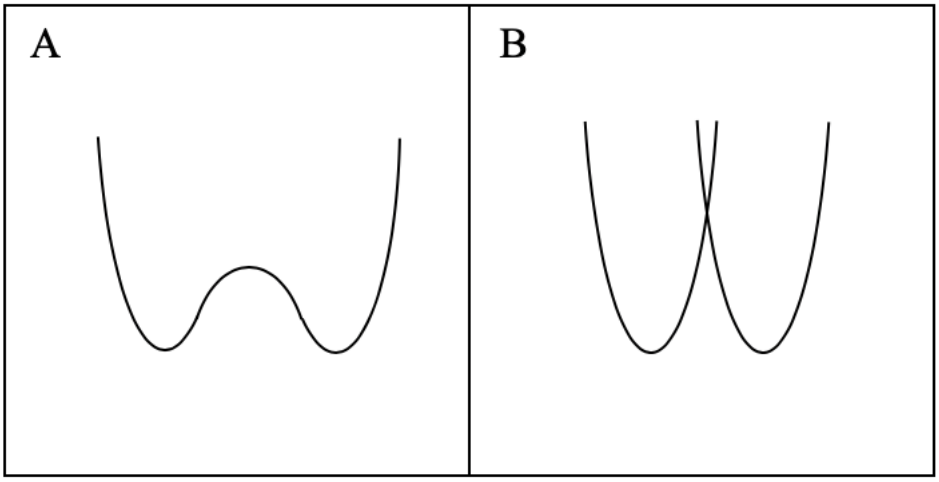

Figure 1: Comparison of potential energy curves calculated within the adiabatic and diabatic representations. In panel A is a diagram of a double well potential energy curve that results from mixing of diabatic states. Panel B shows the pure diabatic states that feature in panel A and B.

1.1.1 Born-Oppenheimer Approximation

The most commonly employed (ab initio) computational techniques within the adiabatic framework (that retain the atomic/molecular picture) are those which are predicated on the Born-Oppenheimer approximation. This approach employs the notion that the electronic and nuclear degrees of freedom are separable due their differing time scales which arise from their large mass difference and sufficient energy separation. This leads to the postulate of the product wavefunction:

$$\Psi(\mathbf{r},\boldsymbol{\omega};\ \mathbf{R}) = \varphi_{el}(\mathbf{r},\boldsymbol{\omega};\ \mathbf{R})\chi_N(\mathbf{R}) \qquad \mathbf{1}$$

i.e. the total wavefunction can be factorized as the product of the nuclear, $\chi_N(\mathrm{R})$, and electronic, $\varphi_{el}(\mathrm{r},\omega;\ \mathrm{R})$, wavefunctions with the electronic wavefunction being parametrically dependent on the nuclear coordinates, R and dependent on electronic coordinates, r, and spin, ω.

The total Hamiltonian (in atomic units) is defined:

$$\widehat{H}_T(\mathbf{r},\mathbf{R}) = T_{\mathrm{nuc}}(\mathbf{R}) + V(\mathbf{r},\mathbf{R}) = T_{\mathrm{nuc}}(\mathbf{R}) + H_{\mathrm{el}} + V_{N-N}(\mathbf{R}) \qquad \mathbf{2}$$

Multiplying by $\langle\Psi(\mathbf{r},\mathbf{R})$from the left and integrating:

$$\left\langle\varphi_{el}(\mathbf{r},\boldsymbol{\omega};\ \mathbf{R})\left|\widehat{H}_T(\mathbf{r},\mathbf{R})\right|\Psi(\mathbf{r},\mathbf{R})\right\rangle = E_T\chi_N(\mathbf{R}) \qquad \mathbf{3}$$

an expression containing the non-adiabatic coupling is obtained:

$$\begin{aligned} E_T\chi_N(\mathbf{R}) = -\frac{1}{2}\sum_i [&\langle\varphi_i(\mathbf{r},\boldsymbol{\omega};\mathbf{R})|\nabla_R^2\ \varphi_i(\mathbf{r},\boldsymbol{\omega};\mathbf{R})\rangle\chi_N(\mathbf{R}) \\ &+ 2\langle\varphi_i(\mathbf{r},\boldsymbol{\omega};\mathbf{R})|\nabla_R\varphi_i(\mathbf{r},\boldsymbol{\omega};\mathbf{R})\rangle\nabla_R\chi_N(\mathbf{R}) + \nabla_R^2\chi_N(\mathbf{R})] \\ &+ V_j(\mathbf{R})\,\chi_N(\mathbf{R}) \end{aligned} \qquad \mathbf{4}$$

$\{\varphi_i(\mathbf{r},\boldsymbol{\omega};\mathbf{R})\}$ are eigenfunctions of the electronic Hamiltonian, H_{el}, and the non-adiabatic coupling between electronic and nuclear degrees of freedom is given by: $\Lambda = -2\mathrm{T}_{(1)}\nabla_R - \frac{1}{2}\mathrm{T}_{(2)}$ where $\mathrm{T}_{(1)}$ ($\mathrm{T}_{(1)}$=$\nabla_R\varphi_i(\mathbf{r},\boldsymbol{\omega};\mathbf{R})$) contains the derivative or adiabatic coupling elements and $\mathrm{T}_{(2)}$ ($\mathrm{T}_{(2)}$ =

$\nabla_R^2\ \varphi_i(\mathbf{r}, \boldsymbol{\omega}; \mathbf{R})$) contain the scalar coupling elements (coupling between eigenstates through the kinetic energy term of the electronic Hamiltonian, H_{el}). The resulting equation is:

$$0 = [T_{\mathrm{nuc}} + \Lambda + V - E]\chi(\mathbf{R}) \qquad \mathbf{5}$$

$$0 = \left[-\left(\nabla + T_{(1)}\right)^2 + V - E\right]\chi(\mathbf{R}) \qquad \mathbf{6}$$

Under the Born-Oppenheimer approximation the non-adiabatic coupling, Λ, is zero. This approximation breaks down at avoided crossings and conical intersections where the coupling between electronic and nuclear degrees of freedom is non-negligible.

1.1.2 Group Born-Oppenheimer Approximation

When a group of states are close enough in energy to mix but are energetically well separated from the remaining electronic states, then only in a block (of the adiabatic coupling matrix) do electronic states mix. The energy separations between the group of electronic states, g are small, coupling between electronic and nuclear degrees of freedom is therefore strong (and constitutes a breakdown in the Born-Oppenheimer approximation but confined to the block i.e. non-adiabatic) and the non-adiabatic representation or the group Born-Oppenheimer approximation is obtained [11]:

$$0 = \left[-\frac{1}{2}\left(\nabla + T_{(1,g)}\right)^2 + T_{ji}^{(3,g)}(R) - E\right]\chi(\mathbf{R}) \qquad \mathbf{7}$$

In this framework, adiabatic coupling is "turned on" within the block and "turned off" elsewhere. $T_{(1,g)}$ contain the adiabatic coupling of the block of electronic states, g. The potential is then equivalent to a dressed potential of the block of electronic states, $V^{(g)}$, to give, $T_{ji}^{(3,g)}$ [12]:

$$T_{ji}^{(3,g)}(\mathbf{R}) = V_i^{(g)}(R)\delta_{ij} + \frac{1}{2}\langle\nabla\varphi_j|\left(1-\hat{P}_g\right)|\nabla\varphi_i\rangle \qquad \mathbf{8}$$

where $\hat{P}_g$, is a projector onto the selected block.

1.1.3 Diabatic Representation

When states are degenerate a singularity exist in the derivative couplings, $T_{(1,g)}$, and presents a challenge for the Born-Oppenheimer approximation. In perturbation theory, a singularity results because derivative coupling depends inversely on the energy separation of electronic states. The diabatic representation is more appropriate and is constructed so as to provide smooth potential energy and coupling surfaces. The diabatic basis is obtained via a unitary transformation, $\mathbb{U}$, in the vector space of electronic states so that the derivative and scalar coupling is zero:

$$\chi^{(a)} = \mathbb{U}\chi^{(d)} \qquad \mathbf{9}$$

The diabatic potential energy is

$$V^{(d)} = \mathbb{U}^{+} V \mathbb{U} \qquad \textbf{10}$$

and

$$\left[\left(V^{(d)} - E\right) - T_{\text{nuc}}\right]\chi^{(d)} = 0 \qquad \textbf{11}$$

The impact of the unitary transform is that derivative and scalar coupling terms are eliminated with the coupling being described by off-diagonal elements of $V^{(d)}$. This approach is computationally expensive since this depends on having access to a complete set of adiabatic states. This is not feasible; in practice, a quasi-diabatic representation in achieved by attempting to minimize (within a predefined tolerance) the derivative coupling.

1.1.4 Ab Initio Adiabatic Approximations of the Schrödinger Equation

A fundamental problem in modern quantum mechanics is the inability to provide an exact solution to the Schrödinger equation (SE) for (most) systems with more than one electron due to the inseparability of the electron-electron term of the SE. This, however, has not limited the practical uses for ab initio methods. Development of new approximations, both ab initio and empirical in nature, along with continued increase in available computing power has made quantum mechanical applications routine.

One of the earliest methods employed within the Born-Oppenheimer approximation, is the Hartree-Fock method which models each electron as moving independently in the average potential of the remaining electrons. This approximation is said to be uncorrelated and in general

accounts for more than 99% of the total energy. The Hartree-Fock method serves as an initial estimation for post-Hartree-Fock methods that recover electron correlation such as configuration interaction (CI), second-order Møller-Plesset (MP2) [13] theory and coupled-cluster (CC) theory. [14] Determining how to leverage the approximations mentioned above is critical to probing proton transfer in solvated molecular ions. This work employs a variety of ab initio methods and an empirical force field to explore proton transfer in molecular cluster ions. In Chapters 2.0 and 3.3.0, we apply density functional theory (DFT) [15–18] and equation-of-motion coupled cluster (EOM-CC) [5,19,20] to study proton transfer in micro-hydrated pyridine anions.

1.1.4.1 Hartree-Fock Approximation

The Hartree-Fock (HF) method is a wavefunction technique employed to describe chemical systems as a function of electronic coordinates, r, and spin, ω, given a set of nuclear coordinates, R (i.e. the electronic wavefunction is parametrically dependent on the nuclear coordinates):

$$\Psi(\boldsymbol{\xi};\mathbf{R}) = \Psi(\mathbf{r},\boldsymbol{\omega};\mathbf{R});\ \omega \in \{\alpha,\beta\} \qquad \mathbf{12}$$

The HF equations are formulated as a pseudo-eigenvalue problem where the eigenvalues and eigenfunctions are molecular orbital energies and functions. Chemical systems are fermionic in nature and therefore the wavefunction must be antisymmetric:

$$\Psi(\xi_1,\xi_2,\dots,\xi_N;\mathbf{R}) = -\Psi(\xi_2,\xi_1,\dots,\xi_N;\mathbf{R}) \qquad \mathbf{13}$$

and adhere to Pauli's exclusion principle. The wavefunction is expressed as a Slater determinant of one-electron wavefunctions:

$$\Psi(\boldsymbol{\xi};\mathbf{R}) = \frac{1}{\sqrt{N!}}\begin{vmatrix} \phi_1(\xi_1) & \phi_2(\xi_1) & \cdots & \phi_N(\xi_1) \\ \phi_1(\xi_2) & \phi_2(\xi_2) & \cdots & \phi_N(\xi_2) \\ \vdots & \vdots & \ddots & \vdots \\ \phi_1(\xi_N) & \phi_2(\xi_N) & \cdots & \phi_N(\xi_N) \end{vmatrix} \quad \textbf{14}$$

Computational methods employed to solve the Schrödinger equation in this thesis express the one-electron wavefunction as a sum of products of atom-centered Gaussian functions, $\psi(R)$ and a spin function, $\sigma(\xi)$:

$$\phi(\boldsymbol{\xi}) = \sum_i c_i \psi_i(\mathbf{R})\sigma(r,\omega) \quad \textbf{15}$$

where:

$$\sigma(\omega) = \begin{cases} \sigma(\alpha): \left| s = \frac{1}{2}, m_s = \frac{1}{2} \right\rangle \\ \sigma(\beta): \left| s = \frac{1}{2}, m_s = -\frac{1}{2} \right\rangle \end{cases} \quad \textbf{16}$$

The HF electronic Hamiltonian operating on one-electron spin orbitals consists of one- and two-electron terms:

$$h(1)\chi_i(1) + \sum_{j\neq i}\left[\int d\mathbf{r}_2 \left|\chi_j(2)\right|^2 \mathbf{r}_{12}^{-1}\right]\chi_j(1) - \sum_{j\neq i}\left[\int d\mathrm{r}_2 \chi_j^*(2)\chi_i(2)\mathbf{r}_{12}^{-1}\right]\chi_i(1) = \epsilon_i\chi_i(1) \quad \textbf{17}$$

which can be re-expressed in terms of the electron – electron Coulomb operator, $\mathcal{J}_j(1)$ and exchange operator, $\mathcal{K}_j(1)$, respectively and form the Fock operator:

$$f(1)|\chi_i\rangle = \left[h(1) + \sum_j \mathcal{J}_j(1) - \mathcal{K}_j(1)\right]|\chi_i(1)\rangle = \epsilon_i|\chi_i(1)\rangle \quad \textbf{18}$$

since:

$$[\mathcal{J}_i(1) - \mathcal{K}_i(1)]|\chi_i(1)\rangle = 0 \quad \textbf{19}$$

where the one electron operator, $h(i)$ (in atomic units) is

$$h(i) = -\frac{1}{2}\nabla_i^2 - \sum_A \frac{Z_A}{\mathrm{r}_{iA}} \quad \textbf{20}$$

A more detailed derivation may be found in Ref.[21]

1.1.4.2 Electron Correlation Energy

The difference between the ground state energy, E_0, and the Hartree-Fock energy, E_{HF}, is called the correlation energy (relativistic effects are not taken into consideration in this work):

$$E_c = E_0 - E_{HF} \quad \textbf{21}$$

The Hartree-Fock energy accounts for most of the exact energy. The missing portion is critical for correct chemical properties which include correct geometric configurations, reaction barrier heights and electron affinities. In many cases the Hartree-Fock method offers a good initial qualitative description. The goal of post-Hartree-Fock methods is to recover the correlation energy (since only same spin correlation is included) improving chemical accuracy.

1.1.4.3 Kohn-Sham Density Functional Theory

Kohn–Sham density functional theory [15] (KS-DFT) approximates the energy as a function of electronic density, ρ. KS-DFT leverages the self-consistent-field approach of Hartree, [22] Slater [23] and Roothaan [24] to calculate orbitals and a many electron wavefunction which is employed to calculate electronic density. KS–DFT energy is partitioned thus:

$$E[\rho] = T_S[\rho] + V_{Ne}[\rho] + J[\rho] + E_{xc}[\rho] \quad \textbf{22}$$

$E_{xc}[\rho]$ is the exchange correlation functional, $T_s[\rho]$ is the Kohn-Sham (KS) kinetic energy which is expressed in terms of a set of KS orbitals $\{\phi_i\}$, which are employed to describe the ground-state electronic density:

$$\rho(\mathrm{r}) = \sum_i |\phi_i(\mathrm{r})|^2 \quad \textbf{23}$$

$$T_s[\rho] = -\frac{1}{2}\sum_i \langle \phi_i | \nabla_i^2 | \phi_i \rangle \quad \textbf{24}$$

$V_{Ne}[\rho]$ and $J[\rho]$ are the nucleus-electron Coulomb energy and repulsive electron-electron energy respectively.

$$V_{Ne}[\rho] = -\int d\mathrm{r}\rho(\mathrm{r}) \sum_A \frac{Z_A}{|\mathrm{r} - \mathrm{R}^A|} \quad \textbf{25}$$

$$J[\rho] = \frac{1}{2}\int d\mathrm{r}' \int d\mathrm{r} \frac{\rho(\mathrm{r})\rho(\mathrm{r}')}{|\mathrm{r} - \mathrm{r}'|} \quad \textbf{26}$$

where r and r´ are electronic degrees of freedom. The form of the exchange-correlation functional, $E_{xc}[\rho]$, is not explicitly known but can be expressed in a constraint formulation [25] or via the adiabatic connection. [26,27] Density exchange-correlation functionals are arranged in a hierarchy referred to as a Jacob's ladder.[28] Each successive rung increases in complexity with the goal of providing better non-local electron correlation description.

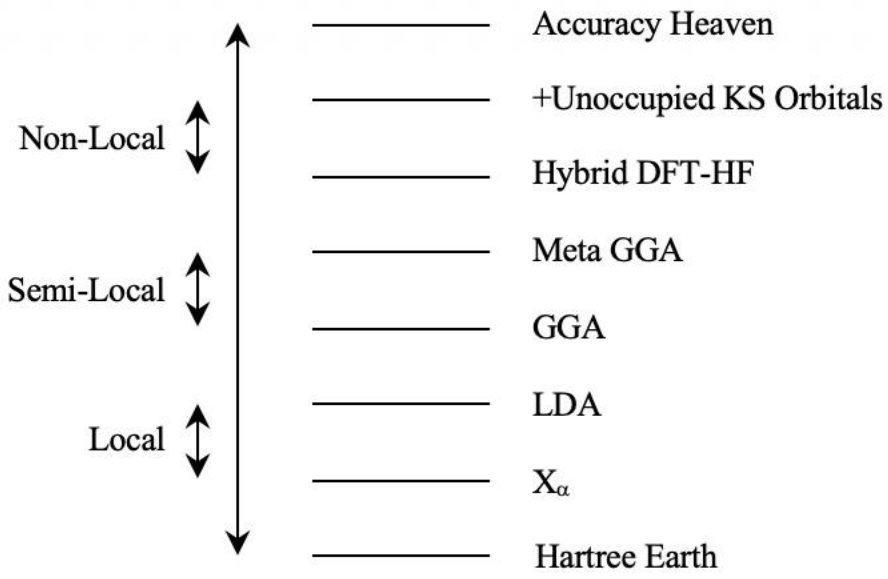

Figure 2: Jacob's ladder of density functional approximations, adapted from the work of Zbiri et al.[29]

The lowest rung, referred to as the local density approximation (LDA), expands the exchange-correlation functional in terms of the ground state electronic density:

$$E_{xc}^{LDA}[\rho] = \int drn\,(r)\varepsilon_{xc}[\rho(r)] \qquad \textbf{27}$$

The second rung, referred to as the generalized gradient approximation (GGA), includes the first derivative of the electron density in the exchange-correlation functional.

$$E_{xc}^{\mathrm{GGA}}[\rho] = \int drn\,(r)\varepsilon_{xc}[\rho(r), \nabla\rho(r)] \qquad \textbf{28}$$

The third rung referred to as meta-GGAs, which includes second derivatives of electron density:

$$E_{xc}^{\text{Meta}-\text{GGA}}[\rho] = \int drn\,(\text{r})\varepsilon_{xc}[\rho(r), \nabla\rho(r), \Delta\rho(\text{r})] \qquad \textbf{29}$$

Higher rungs include hybrid DFT – HF functionals where a percentage of exact exchange (from Hartree-Fock) is employed to describe non-local exchange. While previous rungs required input from occupied orbitals, higher than the 5th rung requires functionals which include unoccupied orbitals, as seen in the random-phase approximation originally of Bohm and Pines. [30–32]

Origin of the Self-Interaction Error

In DFT the exact result is dependent on the use of the exact exchange-correlation functional. In practice, errors arise due to the approximate nature of exchange-correlation functionals. The exchange-correlation functional is the source of the self-interaction error (SIE) when an electron interacts with its own mean-field. [33,34] DFT fails in circumstances where accurate treatment for non-locality of exchange-correlation is crucial as in dissociation and non-bonding interactions. Several strategies have been employed to correct SIE, which include employing GGA's and meta-GGA density functional. It has been accepted that the use of both GGA and meta-GGA functionals alone cannot capture dispersion effects accurately [35–37] or completely remove SIE problem. This is especially true for the study of the hydrated molecular ions presented in this thesis.

Density functional theory (DFT) is used widely for modeling large systems since it offers attractive scaling (when compared to wave-function methods) while recovering electron correlation effects in an approximate manner. Though it is accepted that SIE can be partially remedied by including exact exchange, as in the hybrid GGA, partitioning of density functionals to employ 100% HF exchange for long-range cannot completely compensate for the non-locality

of the correlation hole fundamental to the exchange-correlation functional. Empirical dispersion correction in tandem with a hybrid GGA functional is used in Chapter 2.0.

Empirical Dispersion Correction Approximations

Failure of standard DFT for long-range dispersion interactions has been well documented in the literature. [38–45]. DFT approximation models [46–54] for accurate London dispersion interactions [55–57] are critical for accurate descriptions of physical and chemical properties of heterogenous water clusters. Dispersion interactions can be empirically defined as attractive contributions to the van der Waals (vdW)-type interaction potential between atoms and molecules that are not directly bonded to each other. [49] Generalized gradient approximation (GGA) functionals such as BLYP [58,59], their hybrids such as B3LYP [59,60], which partially replace local exchange with non-local HF exchange (referred to as exact exchange), and meta-GGAs do not reproduce long-range dispersion interactions.[49,61] Dispersion interactions are a purely electron correlation effect and are non-local in nature. To alleviate long-range electron correlation deficiencies most empirical dispersion correction models introduce an additive term [62]:

$$E_{\text{disp}} = -\sum_{i,j}^{N_{at}} \frac{C_6^{ij}}{\mathrm{R}_{ij}^6} \qquad \textbf{30}$$

that is, the leading term from the more general pairwise-additive description of dispersion interactions, which can be represented as a summation of the form:

$$E_{\text{vdW}} = \sum_{i,j}^{N_{at}} \left(-\frac{C_6^{ij}}{\mathrm{R}_{ij}^6} - \frac{C_8^{ij}}{\mathrm{R}_{ij}^8} - \frac{C_{10}^{ij}}{\mathrm{R}_{ij}^{10}} - \cdots \right) \qquad \textbf{31}$$

C_6, C_8, C_{10} are dipole-dipole, dipole-quadrupole and dipole-octupole plus quadrupole-quadrupole dispersion coefficients, respectively.

Dispersion interactions of order n=6 persist at long-range where negligible wavefunction overlap is expected. It is now known that both semilocal and hybrid functionals fail to capture the long-range tail of dispersion interactions.[47,63] In this section, we focus on the dispersion correction of Grimme [48,64] employed in this work. A more comprehensive review of dispersion corrections can be found in Dilabio et al. [65]

Grimme's DFT-D2 Dispersion Correction

Grimme's DFT-D2 [47] dispersion correction is additive:

$$E_{\mathrm{DFT-D2}} = E_{\mathrm{KS-DFT}} + E_{\mathrm{disp}} \quad \textbf{32}$$

The empirical dispersion correction functional form employed in Grimme's DFT-D2 [47] is:

$$E_{\mathrm{disp}} = -s_6 \sum_{i,j}^{N_{at}} \frac{C_6^{ij}}{\mathrm{R}_{ij}^6} f_{\mathrm{damp}}(\mathrm{R}_{ij}) \quad \textbf{33}$$

where N_{at}, is the number atoms; s_6, is a global scaling factor; C_6^{ij}, is the geometric mean of the dispersion coefficients for a given atom pair, (i, j), which has the form:

$$C_6^{ij} = \sqrt{C_6^i C_6^j} \quad \textbf{34}$$

The damping function, $f_{\mathrm{damp}}(\mathrm{R}_{ij})$, employed to prevent near singularities for small interatomic distances, R_{ij}, is given by [66]:

$$f_{\mathrm{damp}}(\mathrm{R}_{ij}) = \left(1 + e^{\alpha\left(\frac{\mathrm{R}_{ij}}{\mathrm{R}_0} - 1\right)}\right)^{-1} \quad \textbf{35}$$

R_0, is the sum of atomic vDW radii. α, the steepness parameter is assigned the value 20. The C_6^{ij} and R_0 parameters employed to calculate dispersion corrected physical properties for heterogenous water clusters in this work are presented in Table 1 below. Dispersion coefficients, C_6^i, are derived from PBE0 [67,68] atomic ionization potential and static dipole polarizability calculations:

$$C_6^i = 0.05\, N I_p^i \alpha^i \quad \textbf{36}$$

The proportionality constant, 0.05, was employed to reproduce binding energy and bond distances of rare gas dimers and select third row complexes.[66] N is assigned 2 and 10 for period 1 and 2 elements respectively. I_p^i is the atomic ionization potential and α^i is the static dipole polarizability of atom i. It should be noted that DFT–D2 was parameterized [47] to be used with the GGA functional, B97 of Becke. [69]

Table 1: Dispersion coefficients and vdW radii parameters employ in BLYP–D2 and B3LYP–D2 calculations.

Atom	C_6 (Jnm^6mol^{-1})	R_0 (Å)
C	1.75	1.452
N	1.23	1.387
O	0.70	1.342
H	0.14	1.001

Highly parameterized meta GGA functionals such as M06-2X [70] capture electron correlation effects in the medium range ≤ 5Å but underperform in the long-range > 5Å when compared to PBE0 [71] plus D2 [47] dispersion correction. It is worth mentioning, that when compared to M05-2X [72], M06-2X and B97-D [73], [47,69] the dispersionless density function (dlDF) method of Szalewicz et al., [74] which is semilocal in nature, plus the Grimme D2 [47] dispersion correction, perform better due to then uniform treatment of long-range interactions.

Grimme's DFT-D3 Dispersion Correction

The DFT-D3 energy is given by [66]:

$$E_{\mathrm{DFT-D3}} = E_{\mathrm{KS-DFT}} + E_{\mathrm{disp}} \quad \textbf{37}$$

where the dispersion correction is a sum of two- and three- body dispersion interaction correction:

$$E_{\mathrm{disp}} = E_{\mathrm{disp}}^{(2)} + E_{\mathrm{disp}}^{(3)} \quad \textbf{38}$$

The two-body contribution is given by:

$$E_{\text{disp}}^{(2)} = -\sum_{ij}\sum_{n=6,8,10,\ldots} s_n \frac{C_n^{ij}}{\mathrm{R}_{ij}^n} f_{\alpha,n}(\mathrm{R}_{ij}) \qquad \textbf{39}$$

where C_n^{ij} refers to the nth order (n = 6, 8, 10, …) dispersion coefficient for atom pair (i, j).

In this iteration of Grimme's dispersion correction [48] the s_6 global scaling parameter is 1, i.e. there is no scaling unless it is employed in conjunction with a doubly-hybrid density functional then $s_6 < 1$. Higher order two-body contribution, n = 8, 10 etc., are scaled. It was found that including n = 8 contributions resulted in increased accuracy, while including n = 10 contributions and beyond did not.[48] To avoid double counting in the region where there is overlap of charge density the n = 8 term is scaled by a damping function. Employing different damping functions allows n = 6 and n = 8 contributions to influence only the long and medium regimes respectively.[75] The functional form of the damping function is as follows: [73,76]

$$f_{\alpha,n}(\mathrm{R}_{ij}) = \left(1 + 6\left(\frac{\mathrm{R}_{ij}}{s_{\mathrm{R}_0^{ij},n}\mathrm{R}_0^{ij}}\right)^{-\alpha_n}\right)^{-1} \qquad \textbf{40}$$

$s_{\mathrm{R}_0^{ij},n}$, is the order dependent scale factor of the R_0^{ij} cutoff radii for the atom pair (i, j).The steepness parameter α_n was not fitted but taken to be $\alpha_{n+2} = \alpha_n + 2;\ \alpha_6 = 14$.

The three-body contribution is given by the Axilrod–Teller–Muto triple dipole dispersion [56,77,78] scaled by a damping function:

$$E^{(3)} = \sum_{ijk} f_{\alpha,(3)}\left(\overline{\mathrm{R}}_{ijk}\right) \frac{C_9^{ijk}\left(3\cos\theta_i \cos\theta_j \cos\theta_k + 1\right)}{\left(\mathrm{R}_{ij}\mathrm{R}_{jk}\mathrm{R}_{ik}\right)^3} \qquad \textbf{41}$$

θ_i, θ_j, and θ_k are the internal angles of the triangles formed by R_{ij}, R_{jk} and R_{ik}, and C_9^{ijk} is the triple dipole constant. For any atom triplet if the internal angles are < 90·° the three-body contribution is repulsive. The form of the damping function is the same as that employed in the two-body term: the parameters employed are $\alpha = 16$ and s_r = 4/3. $\overline{\mathrm{R}}_{ijk}$ is the geometric averaged radii and R_0^{ijk} is taken to be less short range that the dipole-quadrupole two-body terms. Kohn-Sham – time-dependent density functional theory (KS–TD DFT) was employed to calculate dipole-dipole dispersion coefficients for atom pairs using the Casimir-Polder formula. Higher order terms are calculated recursively. It is within this framework that (coordination number) hybridization was considered. [48]

In both DFT-D2[47] and DFT-D3, [48] the dispersion energy, E_{disp}, is functional dependent and is not physically meaningful. To obtain physically meaningful information on the decomposition of intermolecular interacts methods such as symmetry-adapted perturbation theory (SAPT) [79] are required. In hydrated water anions DFT-D2 and D3 corrections to London dispersion interactions affect geometries. A drawback of these dispersion correction methods is that they are not electronic structure dependent nor do they impact electronic structure.[48] A large part of the residual error originates in the underlying density functional. [48] The reproduction of electron binding energy of $[\mathrm{Py}(\mathrm{H_2O})_{n=3}]^-$ (see Chapter 2.0) was used as the standard for determining validity of the theoretical calculations. Due to the afore mentioned issues with DFT one can attribute the reproduction of the electron binding energy to a Pauling point [80]. The errors

associated with DFT however is demonstrated in the theory dependent electronic structure discrepancies between Chapter 2.0 and 3.0.

1.1.4.4 Post-Hartree-Fock Electron Correlation Recovery

Configuration Interaction

One of the simplest approaches to recovering electron correlation is the configuration interaction (CI) method in which the wavefunction is described as a linear combination of Slater determinants:

$$\Psi_{\mathrm{CI}} = c_0|\Phi_0\rangle + \sum_{a,i} c_a^i \left|\Phi_a^i\right\rangle + \sum_{a<b,i<j} c_{ab}^{ij} |\Phi_{ab}^{rs}\rangle + \sum_{a<b<c,i<j<k} c_{abc}^{ijk} |\Phi_{abc}^{rst}\rangle + \cdots \quad \mathbf{42}$$

$c_k^{k'}$ are coefficients of Slater determinants, $\left|\Phi_k^{k\prime}\right\rangle$, where k = 0, 1, 2, 3, … occupied orbitals (a, b, c, …) are replaced with k' = 0, 1, 2, 3, … virtual orbitals (i, j, k). The leading term Φ_0, is the HF determinant. In theory $N = \infty$, where N is the number of excitations, in practice a finite basis is chosen by weighing computational cost, gains in accuracy for increased N, and basis set completeness. The variational principle is employed to determine the coefficients c. The matrix formulation of the characteristic equations for determining CI coefficients and eigenvalues is given by:

$$(\mathrm{H} - E\mathrm{S})\mathrm{c} = 0 \quad \mathbf{43}$$

where S is the overlap matrix. When truncated, CI is not size consistent i.e. given a dimer AB at infinite separation the energy of the dimer is not equal to the sum of the energies of A and B.

Møller-Plesset Theory

Møller-Plesset (MP) theory recovers electron correlation via perturbation theory. [81] The MP Hamiltonian, $H^{(1)}$, is expressed as a perturbation of the simpler HF, the zeroth-order Hamiltonian, $H^{(0)}$, wavefunction and energy.

$$H = H^{(0)} + \lambda H^{(1)} \quad \textbf{44}$$

$$\Psi = \Psi^{(0)} + \lambda\Psi^{(1)} + \lambda^2\Psi^{(2)} + ... \quad \textbf{45}$$

$$E = E^{(0)} + \lambda E^{(1)} + \lambda^2 E^{(2)} + \ldots \quad \textbf{46}$$

The form of the n_{th} order perturbative energy, $E^{(n)}$, and wavefunction, $\Psi^{(n)}$can be by determined recursively. The perturbation series begins at 2nd order, since the first order correction is zero due to Brillouin's theorem: [21,82]

$$E_0^{(2)} = -\sum_{n\neq 0} \frac{\left|\langle \Phi_0 | \hat{V} | \Phi_n \rangle\right|^2}{E_n^{(0)} - E_0^{(0)}} \quad \textbf{47}$$

Several difficulties arise within this approach: 1) MP theory is predicated on the idea that the perturbation is small, 2) If the Hartree-Fock reference is not a good starting point the MP theory wavefunction, and energy is not valid, 3) the MP series is not variational, and 4) the MP series may diverge at higher order. A more detailed review can be found here [21,83].

Coupled-Cluster Theory

Like the configuration interaction method, coupled-cluster (CC) theory [84] is multiconfigurational. Coupled-cluster theory is a size consistent reformulation of the CI excitation operator, $\hat{T}$. Untruncated these theories are equivalent i.e., full CI (FCI) is equal to full CC (FCC). The CC wavefunction is expressed as an exponential ansatz:

$$|\Psi_{\mathrm{CC}}\rangle = e^{\hat{T}}|\Phi_0\rangle \qquad \mathbf{48}$$

where the excitation operator, $e^{\hat{T}}$, can be expanded as:

$$e^{\hat{T}} = \left(1 + \hat{T} + \frac{\hat{T}^2}{2!} + \frac{\hat{T}^3}{3!} + \cdots\right)|\Phi_0\rangle \qquad \mathbf{49}$$

This allows for an expression which can be truncated in the same manner as CI, at n-tuple excitations, $\hat{T}^n$:

$$|\Psi_{\mathrm{CC}}\rangle = |\Phi_0\rangle + \sum_{ai} t_a^i|\Phi_a^i\rangle + \sum_{abij} t_{ab}^{ij}|\Phi_{ab}^{ij}\rangle + \sum_{abcijk} t_{abc}^{ijk}|\Phi_{abcd}^{ijkl}\rangle + \cdots \qquad \mathbf{50}$$

The equations for calculating the CC amplitudes are:

$$\langle\Phi_0|e^{\hat{T}}He^{-\hat{T}}|\Phi_0\rangle = E \qquad \mathbf{51}$$

$$\left\langle \Phi_{ij\ldots}^{ab\ldots} \middle| e^{\hat{T}} H e^{-\hat{T}} \middle| \Phi_0 \right\rangle = 0 \qquad \mathbf{52}$$

CC theory becomes more accurate with the inclusion of higher order excitations, the gold standard in practice being coupled cluster singles-doubles with perturbative triples CCSD(T). [85] In the CCSD(T) singles and doubles contributions are determined as shown above (iteratively), but the triples are determined using perturbation theory, see Ref. [85] Like other post-HF methods, the performance of CC theory hinges on whether HF provides a good initial guess. It inherits the difficulties experienced by HF at near degeneracies (narrow energy gaps).

Equation-of-Motion Electron Affinity Coupled Cluster

An alternative approach for calculating the potential energy surface for proton transfer in the pyridine·$(H_2O)_3$ anion is the equation-of-motion coupled-cluster theory (EOM-CC) [86,87]. EOM-CC exploits the spectroscopic picture of electronic structure, describing the electronic wavefunction description as an ionization, excitation, or electron affinity of a chosen reference. This gives rise to several variants of EOM, ionization potential EOM (EOM-IP), excitation energy EOM (EOM-EE), electron affinity EOM (EOM-EA). In this work electron affinity equation-of-motion coupled cluster is appropriate. Here the neutral species is designated as the reference, and the anion the target state. In chapter 3.0, an avoided crossing is demonstrated along the reaction coordinate between the dipole-bound anion, $[Py\cdot(H_2O)_3]^-$, and the valence-bound proton transfer anion, $PyH\cdot OH^-\cdot(H_2O)_2$. The EA-EOM-CCSD energy of the anion along the proton transfer coordinate converges.

The target wavefunction defined relative to a reference state is given by:

$$|\varphi_{\mathrm{EA-EOM-CCSD}}\rangle = \mathcal{R}|\varphi_{\mathrm{CC}}\rangle \quad \textbf{53}$$

where $\mathcal{R}$, is the excitation operator and φ_{CC} is the CC wavefunction of the neutral species. The EA-EOM-CC wavefunction of the target state is expanded:

$$\begin{aligned}\mathcal{R}|\varphi_{\mathrm{CC}}\rangle &= (\mathcal{R}_1 + \mathcal{R}_2 + \cdots)|\varphi_{\mathrm{CC}}\rangle \\ &= \sum_a r^a\, a_a^\dagger|\varphi_{\mathrm{CC}}\rangle + \frac{1}{2}\sum_i\sum_{ab} r_i^{ab}\, a_a^\dagger\, a_i a_b^\dagger|\varphi_{\mathrm{CC}}\rangle + \cdots\end{aligned} \quad \textbf{54}$$

At the EOM-EA-CCSD level of theory [86,87] when the excitation operator, $\mathcal{R}$, is applied, a one-particle, and a two-hole one-particle excitations are performed on the CCSD wavefunction, φ_{CC}, resulting in the construction of the target state.

1.1.5 Role of Basis Set Choice for Accurate Molecular Description

The basis-set choice influences the accuracy of calculated electron affinities. This is especially true for accurately modeling dipole-bound anions, studied in Chapters 2.0 and 3.3.0. Basis-set choice requires optimization: if the basis set is too small basis set superposition error (BSSE) can occur. When compared to valence-bound anions the excess electron of dipole-bond anions [88,89] is very diffuse [90] and requires very diffuse functions. It should be noted that a good basis set choice cannot compensate for deficiency of the method, e.g. binding a weakly bound excess electron in the dipole field of the a molecule at density functional level of theory, since the excess electron is unbound in the complete basis set limit due to self-interaction error.[91]

1.1.6 Multistate Empirical Valence-Bond Theory

The advancement of spectroscopic techniques has prompted computational inquiry [92] into the structural evolution of protonated water clusters, such as the magic twenty-one cluster ($H^+(H_2O)_{21}$), to uncover the physics encoded in the measured spectra. Ab initio methods become prohibitively expensive for increasingly large clusters, for this reason MS-EVB in conjunction with an empirical water model is employed to describe valence-bond states. In Chapter 4.0, we employ MS-EVB as implemented in the OPTIM software package [93], The water model is a flexible, three-site TIP3P empirical force field [94–97] with modified intramolecular parameters of Voth et al. [98]. Isomerization pathways are calculated as a means of determining whether this approach is suitable for mapping out the potential energy surface of $H^+(H_2O)_{21}$.

For the Eigen cation, MS-EVB, developed by Warshel et al. [10], provides a description of $H_5O_9^+$ in terms of mixing of four empirical valence-bond.

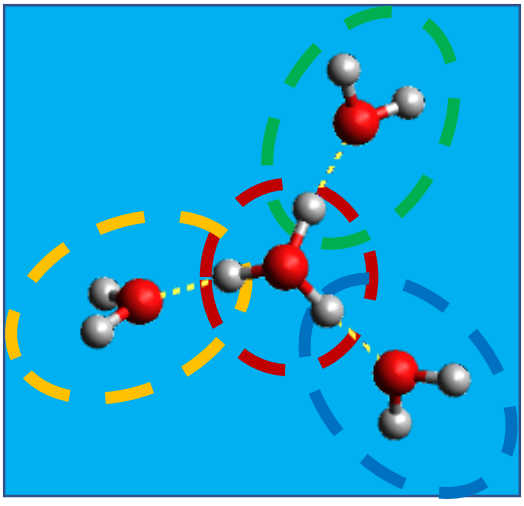

Figure 3: Empirical valence bond states of the Eigen cation (|1>, |2>, |3>, |4>).

MS-EVB approximates proton delocalization by allowing the excess proton to be associated with different water monomers and considers bond breaking and formation reactions as the system evolves from one diabatic state to the other. The result is a set of empirical valence-bond states forming a basis, $\{|i\rangle\}$.

Diagonal MS-EVB Hamiltonian elements, h_{ii}, are given by:

$$h_{ii} = V_{H_3O^+}^{intra} + \sum_{k}^{N_{H_2O}} V_{H_2O}^{intra,k} + \sum_{k}^{N_{H_2O}} V_{H_3O^+,H_2O}^{inter,k} + \sum_{k<k'}^{N_{H_2O}} V_{H_2O}^{inter,kk'} \quad \mathbf{55}$$

where the hydronium–water and water–water intermolecular are approximated by a Lennard-Jones potential, Coulomb energy term and a repulsive potential. Off-diagonal terms of the Hamiltonian mix the diabatic, EVB, states and are given by:

$$h_{ij} = \left(V_{const}^{ij} + V_{complex}^{ij}\right) \cdot A(R_{OO}, q) \quad \mathbf{56}$$

when states $|i\rangle$ and $|j\rangle$ share a hydrogen atom the following reaction: $|i\rangle \rightarrow |j\rangle$ results in proton transfer and h_{ij} is non-zero. V_{const}^{ij} is a coupling constant term and $V_{complex}^{ij}$ is the electrostatic potential between the Zundel complex and the remaining water monomers. $A(R_{OO}, q)$ has the form:

$$A(R_{OO}, q) = \left(\left(1 + Pe^{-k(R_{OO}-D_{OO})^2}\right) \cdot \left(\frac{1}{2}(1 - \tanh[R_{OO} - R_{OO}^0])\right) + 10e^{-\alpha(R_{OO}-R_{OO}^0)}\right) \cdot e^{-\gamma q^2} \quad \mathbf{57}$$

where R_{OO} is the O–O distance of the Zundel cation resulting from the coupling of two MS-EVB states. q is the asymmetric stretch coordinate of the Zundel cation. Values for the parameters employed in $A(R_{OO}, q)$ can be found in Ref. [98]

2.0 Water Network-Mediated, Electron-Induced Proton Transfer in Anionic $[C_5H_5N\cdot(H_2O)_n]^-$ Clusters

This work[1] was published as: Andrew F. DeBlase, Conrad T. Wolke, Gary H. Weddle, Kaye A. Archer, Kenneth D. Jordan, John T. Kelly, Gregory S. Tschumper, Nathan I. Hammer, and Mark A. Johnson, J. Chem. Phys. 143, Vol. 143 (14) 144305 (2015). Kaye A. Archer carried out molecular dynamics simulations and potential energy surface calculations.

2.1 Introduction

The role of proton-assisted charge accommodation in electron capture by a heterocyclic electron scavenger is investigated through theoretical analysis of the vibrational spectra of cold, gas phase $[Py\cdot(H_2O)_{n=3-5}]^-$ clusters. These radical anions are formed when an excess electron is attached to water clusters containing a single pyridine (Py) molecule in a supersonic jet ion source. Under these conditions, the cluster ion distribution starts promptly at n = 3, and the photoelectron spectra, combined with vibrational pre-dissociation spectra of the Ar-tagged anions, establish that for n>3, these species are best described as hydrated hydroxide ions with the neutral pyridinium

[1] A. F. D., C. T. W., G. H. W. carried out experiments and IR calculations; K.A. A, carried out the MD simulations and PES calculations. J.T. K carried out DFT calculations; K D. J, G S. T, N.I. H., and M.A. J guided theoretical, computational and experimental discussions.

radical, $PyH_{(0)}$, occupying one of the primary solvation sites of the OH^-. The n = 3 cluster appears to be a special case where charge localization on Py and hydroxide is nearly isoenergetic, and the nature of this species is explored with ab initio molecular dynamics calculations of the trajectories that start from metastable arrangements of the anion based on a diffuse, essentially dipole-bound electron. These calculations indicate that the reaction proceeds via a relatively slow rearrangement of the water network to create a favorable hydration configuration around the water molecule that eventually donates a proton to the Py nitrogen atom to yield the product hydroxide ion. The correlation between the degree of excess charge localization and the evolving shape of the water network revealed by this approach thus provides a microscopic picture of the "solvent coordinate" at the heart of a prototypical proton-coupled electron transfer reaction.

As an isolated species, the radical anion of pyridine, Py^-, exists as an unstable transient negative ion,[99–106] while in aqueous environment it is known[107] to undergo rapid protonation to form the neutral pyridinium radical $PyH_{(0)}$ along with hydroxide. Consequently, the presence of water plays two essential roles underlying the chemical behavior of Py^-: one to provide a dielectric medium that can electrostatically prevent the valence anion from undergoing electron autodetachment, and the other to facilitate proton transfer by stabilizing the nascent hydroxide ion. Such a scenario provides an interesting opportunity to explore the detailed manner by which these two processes unfold as water molecules are sequentially added to the ionic ensemble $[Py\cdot(H_2O)_n]^-$. This study is motivated by earlier cluster work of Desfrançois and coworkers,[108] who made the important observation that the $[Py\cdot(H_2O)_n]^-$ distribution begins promptly at n = 3 when formed using Rydberg electron transfer. Estimates [100,102–105,108–111] of the Py electron affinity range from -0.48 and -0.79 eV, which means that the isolated anion is unstable with respect to electron detachment.

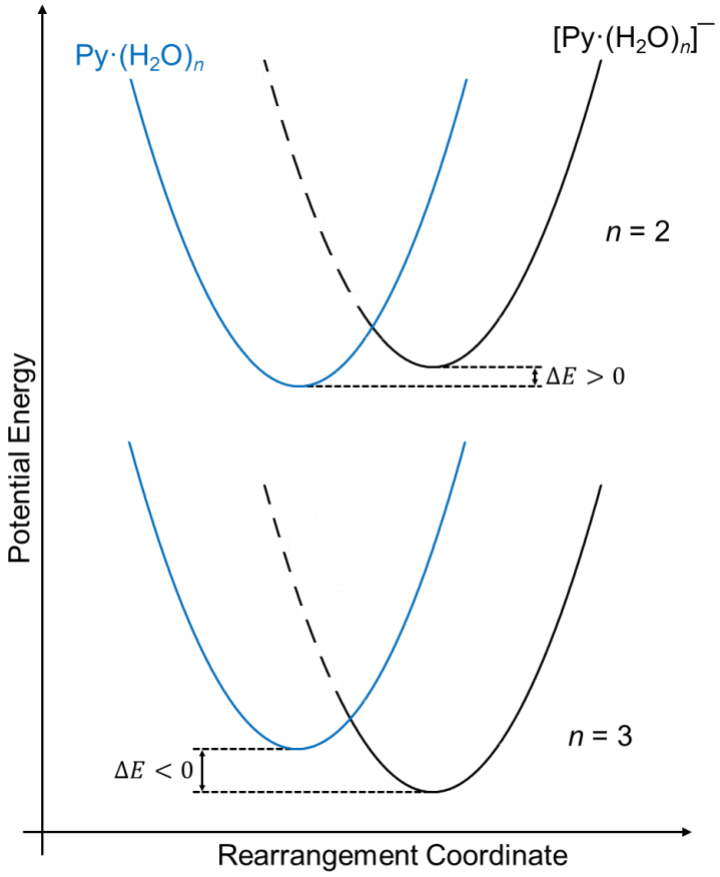

Figure 4: Schematic representation of the potential energy curves for converting $Py\cdot(H_2O)_n$ to the lowest valence anion state of $[Py\cdot(H_2O)_n]^-$ with n = 2 and 3 water molecules. While in the bottom case (n = 3) the charged species is energetically favored, removal of a single water molecule to give n = 2 (top trace) leads to autodetachment of the excess electron. This charge- stabilization by a critical number of solvent molecules has been used to rationalize the observed prompt onset of the $[Py\cdot(H_2O)_n]^-$ distribution at n = 3 in Rydberg electron transfer. [108]

Desfrançois and coworkers[102] attributed the onset of the distribution at n = 3 in the hydrated clusters to the greater stabilization of the Py^- anion (relative to the neutral) with increasing hydration, as indicated schematically in Figure 4. This raises the question, however, of whether such a radical ion can be prepared and isolated as a locally stable arrangement in the early

hydration regime *prior* to the proton transfer event. Indeed, the values for the vertical detachment energies of the untagged $[Py\cdot(H_2O)_{n\geq 3}]^-$ clusters measured in recent negative ion photoelectron spectra [111] have been interpreted to indicate that both $PyH_{(0)}$ created electron-induced proton transfer and reactant Py^- anions were present at $n = 3$, while the spectra of the larger clusters were most consistent with the $PyH\cdot(OH)^-\cdot(H_2O)_{n-1}$ species. [111] This leaves open the questions of how these conclusions depend on the internal energies of the ions, as well as what exact internal rearrangements drive formation of the proton-transferred products. In particular, these results point to an interesting scenario where the proton is effectively titrated from water to Py^- according to the number and arrangement of water molecules in the spirit of our recent study of network-mediated, intracluster proton transfer in the conversion of nitrosonium NO^+ to nitrous acid HONO. [112] Our approach involves an integrated analysis of the photoelectron angular distribution, vibrational predissociation, and photo-induced vibrational autodetachment spectroscopies of the Ar-tagged products from the reaction between neutral Py and the negatively charged water clusters:

$$Py + (H_2O)_n^- \rightarrow Py\cdot(H_2O)_n^- \rightarrow PyH\cdot(OH^-)\cdot(H_2O)_{n-1} \qquad \textbf{58}$$

and thus extends the recent photoelectron work of Wang et al.[111] We then explore the mechanism by which an excess electron, initially delocalized in a diffuse orbital of the system, [113,114] becomes localized into a valence molecular orbital through the cooperative interplay between the water network and the key proton transfer reaction coordinate: N···H···OH.

2.2 Experimental and Computational Methods

2.2.1 Vibrational Photodissociation, Photo-Induced Vibrational Autodetachment, and Photoelectron Spectroscopy

Anionic clusters of H_2O with Py were synthesized in an electron-impact ionized supersonic jet expansion of Ar carrier gas (60 psi) seeded with trace water and Py vapors, which were co-expanded through a single pulsed valve (*Parker Hannifin* General Valve Series 9, 0.030 in. aperture). A 1 keV electron beam counterpropagating along the axis of the supersonic expansion generated negatively charged cluster ions in the resulting neutral plasma. Conditions were optimized for attachment of weakly bound Ar atom "tags" to the cluster anions, thus enabling vibrational predissociation spectroscopy by photoevaporation of the Ar atoms:

$$[Py\cdot(H_2O)_n]^-\cdot Ar_p + h\nu \rightarrow [Py\cdot(H_2O)_n]^-\cdot Ar_{p-q} + q\ Ar \qquad \textbf{59}$$

using the Yale double focusing, tandem time-of-flight photofragmentation mass spectrometer described previously. [115]

The parent $[Py\cdot(H_2O)_n]^-\cdot Ar_p$ ion and $[Py\cdot(H_2O)_n]^-\cdot Ar_{p-q}$ photofragment were separated by a secondary (reflectron) mass spectrometer. The $[Py\cdot(H_2O)_3]^-\cdot Ar_p$ cluster also exhibited vibrational autodetachment above 3000 cm^{-1}:

$$[Py\cdot(H_2O)_3]^-\cdot Ar_p + h\nu \rightarrow [Py\cdot(H_2O)_3] + p\ Ar + e^- \qquad \textbf{60}$$

The action spectrum for electron ejection through Equation 60 was recorded as a function of photon energy by monitoring the electron signal on microchannel plates positioned below the laser interaction region.

All vibrational predissociation and photo-induced vibrational autodetachment spectra between 2250 and 3800 cm^{-1} were obtained using a *LaserVision* OPO/OPA mid infrared system pumped by a Nd:YAG laser (10 Hz, 8 ns pulse width). Radiation in the 600-2500 cm^{-1} region was produced by generating the difference frequency between the ~1.5 and ~3 μm beams from the OPO/OPA in a $AgGaSe_2$ crystal. The spectra of the low and high frequency regions (600-2500 cm^{-1} *vs.* 2250-3800 cm^{-1}) were combined by normalizing the intensities of transitions that occur in the overlap region from 2250 to 2500 cm^{-1} that can be reached with both configurations. In addition, the photofragment signal was divided by the laser pulse energy to account for changes over the course of a scan. Experimental spectra represent the summation of 15-20 individual scans.

Photoelectron spectra were acquired by velocity map imaging at an excitation energy of 2.33 eV using an instrument described in detail elsewhere. [116–120] Images were converted to photoelectron spectra using the BASEX transformation. [118] The vibrational structure of the NO^- spectrum was used to calibrate the spectrometer.

2.2.2 Structure Optimizations and Harmonic Frequency Calculations

To aid in assigning the vibrational spectra, the geometries of various possible structures of the $[Py{\cdot}(H_2O)_n]^-$, n = 2-5 clusters were optimized using M06-2X [70] density functional method with the 6-31++G(d,p) [121–123]basis set. This approach was chosen because it has recently been

shown to accurately reproduce experimental photodetachment energies of hydrated azabenzene anions. [111] The X-H (X = N,O,C) stretching fundamentals were scaled by 0.980 for this level of theory, while the lower energy, non-stretching modes were not scaled. These calculations were performed using the Gaussian09 program. [124]

2.2.3 Born Oppenheimer Molecular Dynamics Simulations

In order to gain insight into the rearrangement dynamics, we also carried out Born-Oppenheimer molecular dynamics (BOMD) simulations of $[Py\cdot(H_2O)_3]^-$ starting from the structure corresponding to the dipole-bound anion. The simulations were carried out in the NVE ensemble with an excess energy corresponding to T = 270 K, randomized over all atoms. This temperature corresponds to ~180 cm^{-1} per degree of freedom, whereas excitation of an OH stretch would deposit ~120 cm^{-1} into each intermolecular degree of freedom (assuming validity of the equipartition theorem and that no energy is deposited into the high-frequency intramolecular modes after randomization). Thus, the simulations were carried out at an energy content in excess of that in play under the experimental conditions, which leads to accelerated dynamics. The BOMD simulations were carried out using the CP2K [125] code and were conducted using the BLYP density functional method, [58,126] including the D2 long-range interaction correction of Grimme [64] and employing the Goedecker-Teter-Hutter pseudopotentials, [127] aug-DZVP-GTH basis sets, [127,128] and a plane wave cutoff of 280 Ry. The Martyna Tuckerman Poisson solver [129] was employed in the calculation of the electrostatic interactions. A cubic box of 18 Å sides was employed, and a time step of 1.0 fs was used.

2.3 Results and Discussion

2.3.1 The Py·$(H_2O)n^-$ Cluster Distribution: An Abrupt Onset at n = 3

The mass spectrum obtained from the ionized free jet, as described above, is displayed in Figure 5, which shows the distribution of $[Py\cdot(H_2O)_n]^-$ clusters (red) and their complexes with an argon atom (blue). Bare hydrated electron clusters with n = 6 and 7 (colored gray) and their Ar adducts (bronze) are also generated in abundance. The abrupt onset of $[Py\cdot(H_2O)_n]^-$ anions at n = 3 is in accordance with the earlier observations by Desfrançois and co-workers, as discussed in the Introduction. While not our focus in this work, we note in passing that we were able to generate the smaller n = 2 species using Ar-mediated condensation,

$$Py + (H_2O)_n^-\cdot Ar_m \rightarrow [Py\cdot(H_2O)_n]^-\cdot Ar_{m^*} \rightarrow [Py\cdot(H_2O)_n]^-\cdot Ar_p + (m\text{-}p)\ Ar \qquad \mathbf{61}$$

in a different source scheme where the Py vapor is introduced with a second pulsed valve and entrained into the electron beam ionized expansion. That approach was used earlier to form very low adiabatic electron affinity (AEA) anions [e.g., $(H_2O)_4^-$] as well as metastable anions with diffuse excess electrons. [130–133]

It is useful to consider the origin of the onset of the cluster distribution at n = 3 in the context of the behavior of related systems. For example, the $(H_2O)_n^-$ distribution, at high water

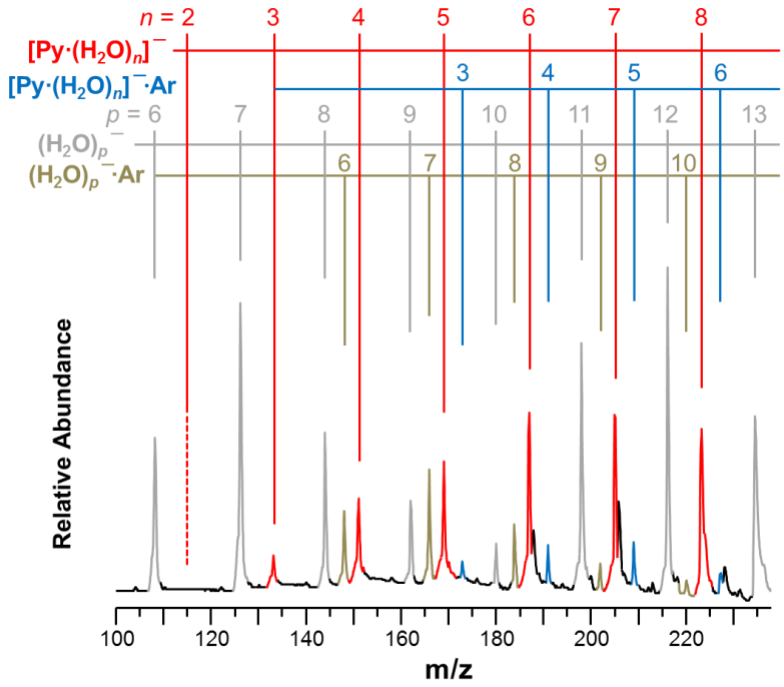

Figure 5: Mass spectrum of electron-impact ionized species generated by coexpanding trace water and pyridine vapor in a supersonic jet with Ar carrier gas. The peaks due to the $[Py\cdot(H_2O)_n]^-$ clusters are colored red, while the blue peaks designate the Ar-tagged species, $[Py\cdot(H_2O)_n]^-\cdot Ar$. The hydrated electron clusters $(H_2O)_n^-$ as well as their Ar-tagged derivatives, $(H_2O)_n^-\cdot Ar$, are also present in the mass spectrum (gray and bronze, respectively). The dotted vertical red line points out that the $[Py\cdot(H_2O)_2]^-$ species is not present under these source conditions.

partial pressures [134,135] displays an abrupt onset at n = 15, which has been traced to a condition where the AEA becomes roughly equal to the water binding energy at this cluster size. In that case, the onset occurs because the smaller cluster anions are neutralized due to electron ejection when the condensation energy released upon attachment of a water monomer is larger than the AEA (i.e., a type of associative detachment reaction). [136] The onset of the $[Py\cdot(H_2O)_n]^-$ cluster distribution at n = 3 therefore indicates that the AEA increases much more rapidly with increasing cluster size than for neat water clusters.

2.3.2 Velocity Map Imaging Photoelectron Spectroscopy of the $[Py\cdot(H_2O)_3]^-$ Cluster: Evidence for a Valence Anion

To assess the nature of the excess electron orbital in the $[Py\cdot(H_2O)_n]^-$ clusters, the angular distributions of photoelectrons were obtained by velocity map imaging using an excitation wavelength of 532 nm (2.33 eV).These results for $n = 3$ are given in Figure 6, where the raw image and photoelectron energy distributions (after BASEX transformation) [118] are given in traces (a) and (b), respectively. The spectrum is very broad, consistent with that reported by Wang et al., [111]

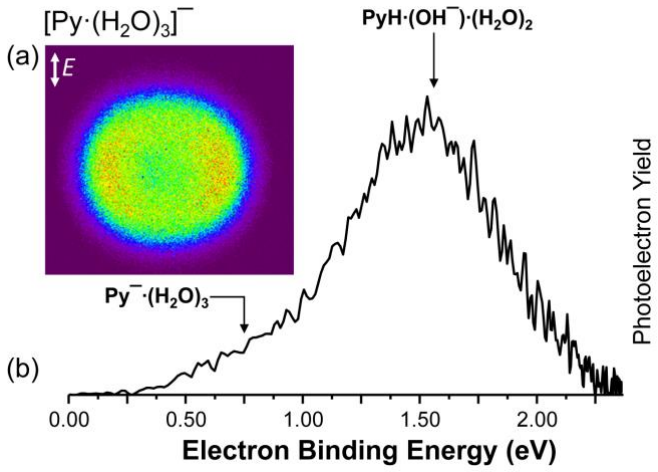

Figure 6: Velocity map image (a) and resulting photoelectron spectrum (b) of $[Py\cdot(H_2O)_3]^-$ after the BASEX transform procedure. [137] This spectrum was obtained using an excitation energy of 2.33 eV and plotted as a function of the electron binding energy. The white arrow in the image indicates the direction of the electric field vector (E) of the laser. Arrows above the spectrum indicate the VDE values for $Py^-\cdot(H_2O)_3$ and $PyH\cdot(OH^-)\cdot(H_2O)_2$ assigned by Wang et al.

displaying a full width at half maximum (FWHM) of 0.85 eV, indicating that the vertical electron detachment energy (VDE) is much greater than the AEA. The peak photoelectron yield of the distribution occurs at 1.53 eV, corresponding to the VDE, which is in close agreement with the VDE of 1.56 eV reported by Wang et al. [111] Most importantly, the image in Figure 6a) exhibits a significantly negative anisotropy parameter [138] of about -0.5, indicating that photoelectrons are preferentially ejected *perpendicular* to the direction of the electric field vector (double-headed white arrow in Figure 6a). This behavior is opposite to that displayed by the hydrated electron clusters, $(H_2O)_n^-$, for which β values are observed close to +2, [139,140] the limiting value expected for a s→p electron ejection scenario. Furthermore, anionic water clusters in the size range around $n = 5$ have much lower VDEs (< 0.5 eV) [130,141–143] with narrow photoelectron distributions closer resembling that displayed by diffuse, dipole-bound electrons. [144] These results indicate that the excess electron in the $[Py\cdot(H_2O)_3]^-$ cluster occupies a valence molecular orbital and is likely associated with a solvated OH^- ion. Photoelectron spectra of the $n = 4$ and $n = 5$ clusters are also given in the Supplemental Material (Figure 33). [105] As reported earlier, the binding energy increases with hydration such that the band becomes distorted due to threshold effects when the VDE approaches the photon energy.

2.3.3 Calculated Structures

The calculated [M06-2X/6-31++(d,p)] minimum energy structures for the $n = 3$-5 clusters identified earlier by Wang et al. are reproduced in Figure 7. Interestingly, the $n = 3$ cluster has two nearly isoenergetic isomers: one that exhibits proton-transfer from a water molecule to the pyridine leaving a solvated hydroxide ion (Figure 7a) and another that contains a hydrated Py^- ion

(Figure 7b).

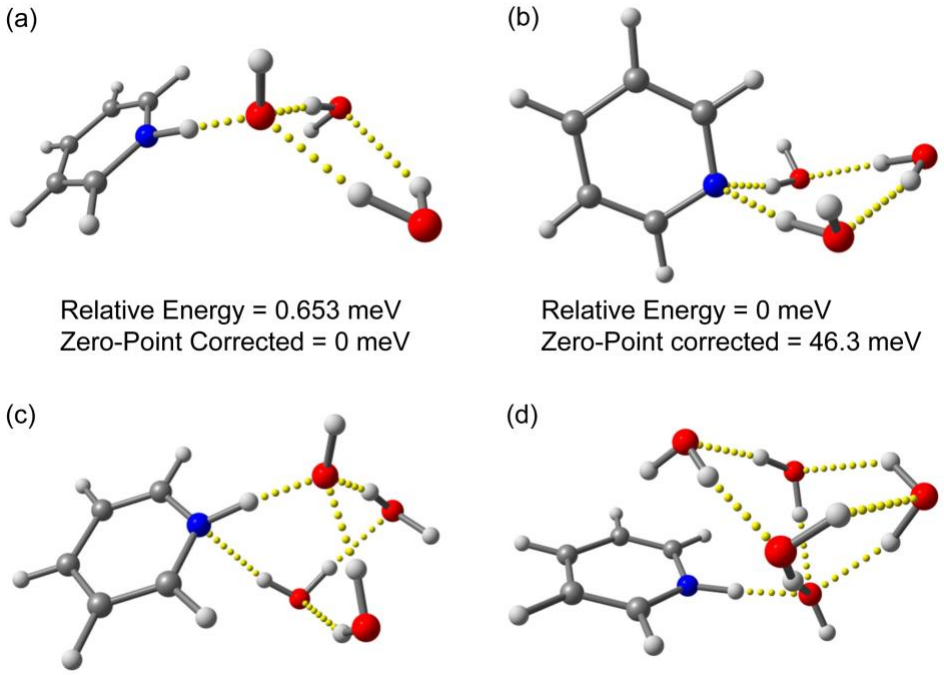

Figure 7: Calculated low energy M06-2X/6-31++G(d,p) structures. a) and b) are two low lying isomers of n = 3, where correction for the vibrational zero-point energy brings the intracluster proton transfer structure (a) lower in energy. The formation of the PyH radical is a robust feature of the larger clusters c) n = 4 and d) n = 5.

Thus, the *n* = 3 cluster appears to represent a tipping point in the electron-driven intracluster proton transfer reaction, and indeed introduces the interesting possibility that vibrational excitation of the cold cluster can promote large amplitude rearrangements associated with this process.

2.3.4 Vibrational Predissociation and Photo-Induced Vibrational Autodetachment Spectroscopies: Evidence for Strong Ionic H-Bonding

2.3.4.1 Infrared Photophysics of the Ar-Tagged and Bare Clusters

The broad photoelectron spectra do not allow structural determination of the molecular nature of the species that bear the negative charge. To help clarify this situation, we obtained the vibrational pre-dissociation spectra of the $[Py\cdot(H_2O)_n]^-$ clusters tagged with Ar, with the results presented in Figure 8. The average number of Ar atoms lost is found to be linearly dependent on the photon energy (see Supplemental Material, Figure 31), [Appendix B.0] establishing that each tag has a similar binding energy on the order of 750 cm^{-1}/Ar. In the case of the smallest persistent cluster at n = 3, it was only possible to observe fragment anions corresponding to Ar loss below 3300 cm^{-1}, while strong features were observed in the higher energy range for the n = 4 and 5 species. This type of behavior has been observed in $(H_2O)_n^-\cdot Ar_m$ clusters, [145] for which the nascent anionic fragment, $(H_2O)_n^{-*}$, is unstable with respect to electron autodetachment, [119]

$$(H_2O)_n^-\cdot Ar_m + h\nu \rightarrow (H_2O)_n^{-*} + m\ Ar \rightarrow (H_2O)_n + e^- \qquad \mathbf{62}$$

unless it is sufficiently cooled by Ar evaporation. We therefore also monitored the electron photo-detachment channel:

$$Py\cdot(H_2O)_n^-\cdot Ar + h\nu \rightarrow [Py\cdot(H_2O)_n]^{-*} + Ar \rightarrow Py\cdot(H_2O)_n + e^- \qquad \mathbf{63}$$

with the results displayed in the insert in Figure 8a) for the Ar-tagged $n = 3$ cluster. The "missing' bands are indeed recovered in the electron loss channel, and these transitions can also be observed in the photofragmentation spectrum of $[Py\cdot(H_2O)_3]^-$ tagged with 4 Ar atoms (see Supplemental Material, Figure 30). [Appendix B.0] This observation of vibrational autodetachment is significant in that it emphasizes the close proximity of the adiabatic electron continuum and the significant rearrangement that is required to access the intersection between the anionic and neutral potential surfaces.

2.3.4.2 Comparison with the Vibrational Spectrum of the $OH^-(H_2O)_n$ Anion

A striking qualitative aspect of the vibrational spectra is that they are extremely broad. For $n = 3$ and 4, for example, diffuse absorptions span most of the 900-3300 cm^{-1} range in contrast to the sharp features displayed by the water cluster anions in this size regime. [130,146] This behavior is also unusual for the microhydration of small molecular anions (*e.g.*, $CO_2^-\cdot(H_2O)_n$) [131] of similar size. Even the intramolecular HOH bending mode is obscured in the $n = 3$ spectrum, and the only features that can be assigned by inspection are the relatively sharp bands near 3700 cm^{-1} due to the free OH stretching modes and those near 3000 cm^{-1} arising from the ring CH stretching fundamentals. Interestingly, the transitions in the lower energy range are much better defined in the larger ($n = 5$) cluster spectrum, with the onset of the diffuse band shifted toward higher energy, beginning at 2400 cm^{-1}.

The calculated harmonic spectra for the minimum energy structures displayed in Figure 7 are included in Figure 8 as inverted traces. Perhaps the most important conclusion from this comparison is that the spectra are so dominated by strong anharmonicities that even the most cursory assignments are not obvious.

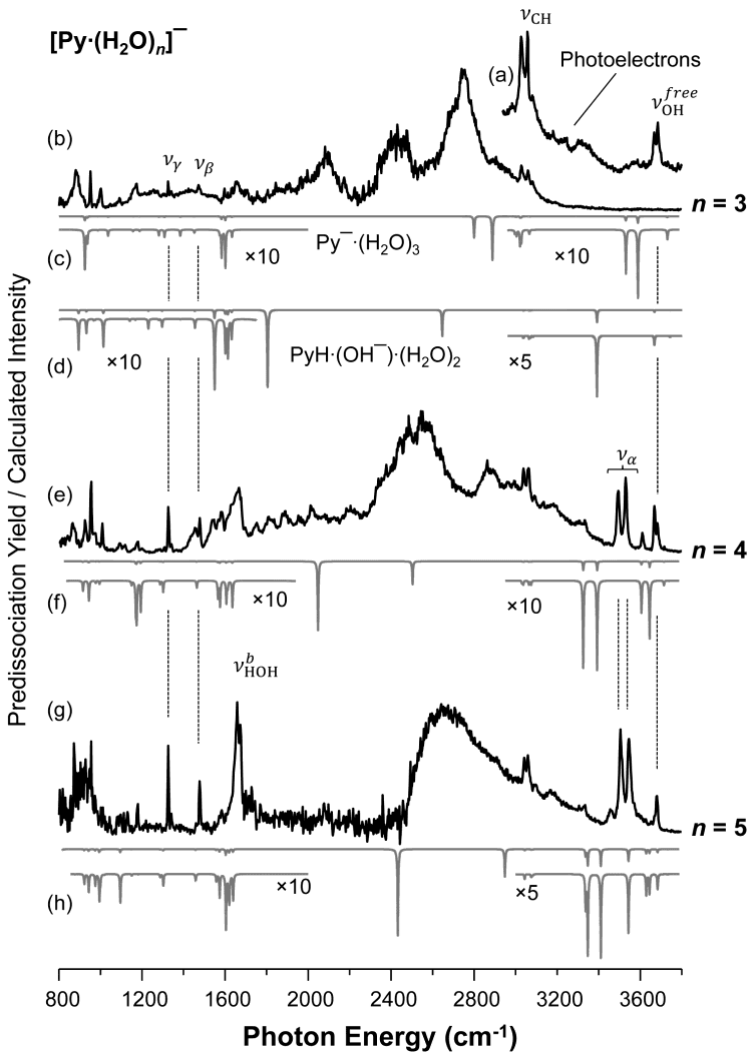

Figure 8: Vibrational action spectra of the $[Py\cdot(H_2O)_n]^-$ clusters. The full infrared spectrum for the $[Py\cdot(H_2O)_3]^-\cdot Ar$ species was recorded by combining the photo-induced vibrational autodetachement channel above 3000 cm-1 (a) with the Ar-predissociation spectrum measuring formation of bare $[Py\cdot(H_2O)_3]^-$ photofragment ions (b). The spectra of $[Py\cdot(H_2O)_4]^-$ (d) and $[Py\cdot(H_2O)_5]^-$ (f) were obtained by Ar-predissociation between 800 and 3800 cm-1. Calculated harmonic spectra [M06-2X/6-31++G(d,p) level] of the low energy proton transfer structures for n = 3, 4, and 5 are shown in the inverted grey traces of (d), (f), and (h), respectively, while the harmonic spectrum of the $Py^-\cdot(H_2O)_3$ is shown in trace (c). Key features are indicated by the dotted guidelines, including: free OH stretching (ν_{OH}^{free}) and CH stretching (ν_{CH}), and other distinct bands (ν_α, ν_β, and ν_γ) that are addressed in the discussion.

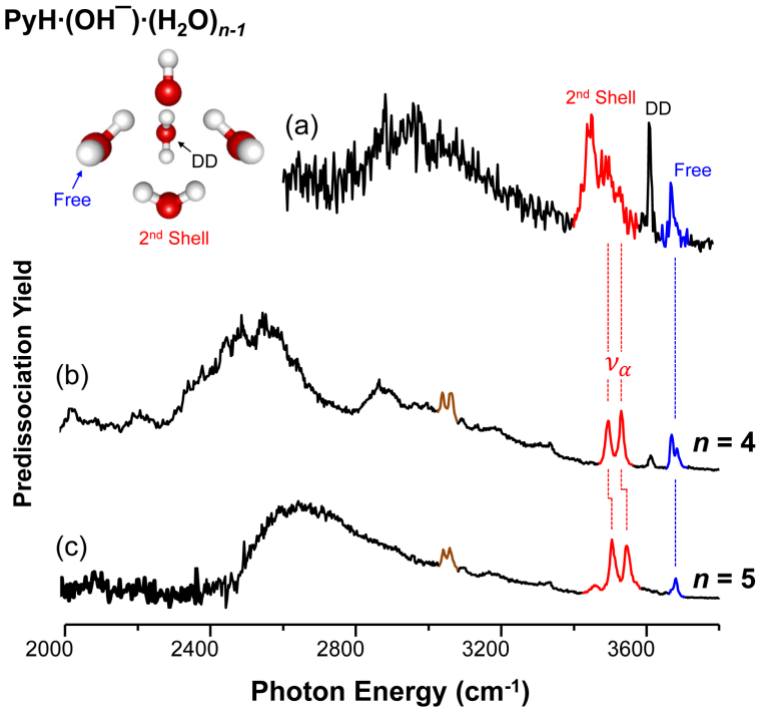

Figure 9: Vibrational predissociation spectrum of the $OH^-\cdot(H_2O)_4$ cluster (a) with the minimum energy structure consistent with the spectrum depicted in the insert. This spectrum is from Science, 299, 1367 (2003), and has been reprinted with permission from AAAS. Vibrational predissociation spectra of the Ar-tagged $[Py\cdot(H_2O)_n]^-$ clusters with n = 4 (b) and 5 (c) are shown for comparison. Bands are assigned according to their number of H-bond acceptor (A) and donor (D) interactions of specific water molecules in the network.

Rather than engage a very difficult exercise in simulating the anharmonic spectra of floppy systems clearly at play here, we find it more useful to empirically evaluate the chemical compositions of the $[Py\cdot(H_2O)_n]^-$ clusters by comparing their vibrational spectra to that of the $OH^-\cdot(H_2O)_4$ cluster reported earlier, [147] and included at the top of Figure 9. Interestingly, a similarly diffuse band is also found in this species, where three water molecules are directly attached to the hydroxide ion and a fourth lies in the second solvation shell as illustrated in the inset structure. This diffuse band has been attributed to excitation of the OH groups engaged in H-bonds to the ion, while the sharp pattern highest in energy arises mostly from non-bonded OH

groups or OH groups of the water molecule in the second solvation shell in a double H-bond donor (DD) configuration (ν_α). Note that the intensity of the hydroxide OH fundamental has been found to be dramatically suppressed upon completion of its hydration shell. [148] The fact that the spectral signatures of all three classes of OH environments (primary shell, secondary shell, and free) in hydrated hydroxide clusters are present in $[Py\cdot(H_2O)_{4,5}]^-$ strongly suggests that these clusters adopt $PyH\cdot(OH^-)\cdot(H_2O)_{n-1}$ arrangements that would be consistent with an intracluster variation of the proton transfer process observed in solution (Equation 58).

2.3.4.3 Identification of the CH Bending Fundamentals of $PyH_{(0)}$

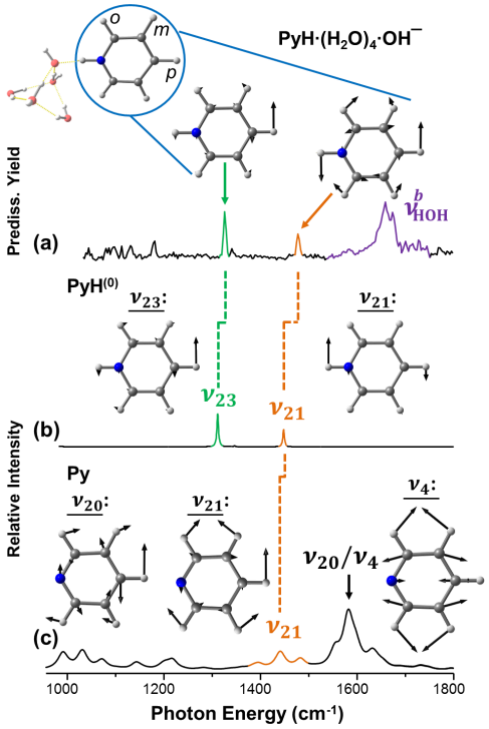

Figure 10: A comparison between the Ar-predissociation spectrum $[Py\cdot(H_2O)_5]^-$ (a), the infrared spectrum of $PyH_{(0)}$ taken in solid p-hydrogen (b), [149] and the infrared spectrum of neutral pyridine vapor [150] **in the OH and CH bending regions (c). The spectrum in trace (b) is a convolution of the tabulated frequencies and intensities in Ref.[149] with a Lorentzian (4 cm^{-1} FWHM). (c) is a convolution of tabulated peaks in Ref.**[150]**, with 20 cm^{-1} half-width Lorentzians. The normal mode displacement vectors of the $Py/PyH_{(0)}$ moiety in each of these species are illustrated next to the corresponding transitions. The green and orange dotted guidelines highlight the proximity of transitions in the two model compounds to those observed in the spectrum of $[Py\cdot(H_2O)_5]^-$.The reduction in complexity of the n = 5 spectrum in the fingerprint region warrants an effort to identify key well-defined peaks in the context of the hydroxide product, specifically the sharp features labeled ν_β and ν_γ in Figure 8. This region of the spectrum is expanded in Figure 10. The bands in question are quite close in frequency to the predicted ring CH bending modes of $PyH_{(0)}$, denoted ν_{23}^{Py} and ν_{21}^{Py} and colored green and orange, respectively in Figure 10. Here the mode numbering is that for isolated $PyH_{(0)}$ with C_{2v} symmetry (numbered in order of highest to lowest symmetry and highest to lowest energy).**

In light of the difficulties with the harmonic predictions discussed above, it is again useful to compare the observed spectra with empirical data to further assess the viability of the PyH·(OH^-)·$(H_2O)_{n-1}$ motif. Figure 10 compares the vibrational predissociation spectrum of $[Py\cdot(H_2O)_5]^-$ to the IR absorption spectrum of the $PyH_{(0)}$ radical isolated in a matrix of frozen *para*-hydrogen[149] and to the gas phase vibrational spectrum of neutral Py. [150] $PyH_{(0)}$ in the *para*-hydrogen matrix was synthesized by Lee et al. by electron bombardment and photolysis of Cl_2/Py/*p*-H_2. For a simplified comparison to our data, we have simulated their spectrum using the tabulated wavenumbers and intensities that were assigned to the $PyH_{(0)}$ species (convoluted using a Lorentzian with a FWHM of 4 cm^{-1}). Both ν_{23} and ν_{21} of the $PyH_{(0)}$ species are very close to the observed sharp bands in the $[Py\cdot(H_2O)_5]^-$ vibrational predissociation spectrum (Figure 10a) with similar relative intensities, albeit with a small red-shift (14 and 30 cm^{-1} for ν_{23} and ν_{21}, respectively) in the solid *p*-hydrogen matrix. Most importantly, these bands are quite different from the pattern displayed by the neutral Py molecule, which has been obtained from vapor-phase measurements and is included in Figure 10c).

2.3.5 Theoretical Exploration of the Rearrangement Pathways in $[Py\cdot(H_2O)_3]^-$

2.3.5.1 Potential Surface for Intracluster Proton Transfer

The empirical evidence points to a situation where the system explores both $Py^-\cdot(H_2O)_n$ and $PyH\cdot(OH^-)\cdot(H_2O)_{n-1}$ components with the latter dominating but with the relative weights of the two terms depending on the degree of solvation of the OH^-. Qualitatively, as the hydroxide-based clusters accommodate additional water molecules on the emergent network, the configuration with the excess charge on the OH is stabilized, while that with the charge on the Py

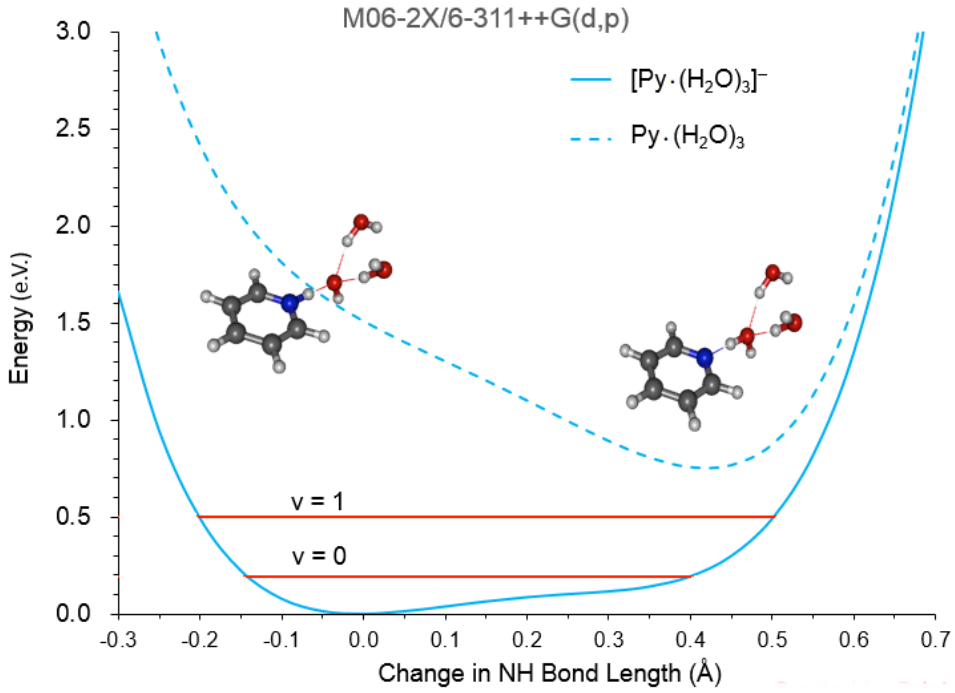

Figure 11: One-dimensional potential energy curves for proton transfer in $[Py\cdot(H_2O)_3]^-$ (solid blue line) and $Py\cdot(H_2O)_3$ (dashed blue line). The minimum energy structure of the anion used in generating these potentials is shown in the inset on the left. The potentials are calculated by varying the NH distance, keeping all other degrees of freedom frozen. On the left-hand side of the anion potential the structure is dominated by $PyH\cdot(OH^-)\cdot(H_2O)_2$, while on the right-hand side it is dominated by $Py^-\cdot(H_2O)_3$. Estimates of the energies of the v = 0 and 1 levels of the anion are illustrated by red horizontal lines.

becomes less important. Thus, in the $n = 3$ case, the proton is more strongly shared in the N···H···O motif, giving rise to very broad spectral features typical for shared protons. [151] At smaller n, excitation of the nominal NH stretch samples the $Py^{-}\cdot(H_2O)_n$ configuration, in essence driving the proton transfer reaction with concomitant excess charge displacement. Such a scenario has been demonstrated to be at play in the binary complex $F^{-}\cdot HOH$, [152] where excitation of the bridging proton stretch samples a region in the potential surface corresponding to $HF\cdots OH^{-}$. When this occurs in a system where the associated water network responds to the change in the charge distribution, it is expected that vibrational excitation will induce substantial heavy particle rearrangements, thus rationalizing the nearly continuous nature of the spectrum for $n = 3$.

To better quantify the nature of the potential surfaces governing the heavy particles and excess electron, we calculated one-dimensional potential energy curves for proton transfer in $[Py\cdot(H_2O)_3]^{-}$ and $Py\cdot(H_2O)_3$. The potentials were calculated starting from the M06-2X optimized structure shown in Figure 7b with a $PyH\cdot(OH^{-})\cdot(H_2O)_2$ configuration, and then carrying out a series of single-point calculations for the anion and neutral for different values of the NH distance, assuming linear motion between the N atom and the O of the hydroxyl, and keeping all other degrees of freedom frozen. The resulting anion potential energy curve, shown in Figure 11, is exceedingly anharmonic, such that even the zero-point level samples the $Py^{-}\cdot(H_2O)_3$ structure. The vibrational zero-point level of the neutral potential along this slice lies above the $v = 1$ level of the anion; however, relaxation of the geometry of the neutral causes its zero-point level to fall below the $v = 1$ level of the anion (as evidenced by the experimentally observed opening of the electron autodetachment channel). We note that the actual energy gap between the proton-transfer and non-proton transfer structures may be somewhat larger than predicted by the M06-2X method. In particular, preliminary results using the restricted open-shell MP2 method [13,153] predict the

non-proton transfer structure to be about 477 meV less stable than the proton-transfer structure, rather than being nearly isoenergetic as predicted by the M06-2X method. In either case, however, it is still anticipated that excitation of the $\nu = 1$ OH manifold will induce significant large amplitude motions that mediates interconversion between these two structures.

As the charge becomes more stabilized on the OH^-, the spectra become simpler as excitation of one quanta of OH stretch no longer leads to sampling of the $Py^-\cdot(H_2O)_n$ class of structures. A primitive manifestation of this type of blue-shifting by differential solvation of charge-localized, asymptotic partners (in this case $Py^-\cdot H_2O$ *vs.* $PyH\cdot OH^-$) has, in fact, been routinely invoked to understand the rare gas tag effects in binary complexes. The case of solvation by water can thus be viewed as an extreme example of a generic solvent response by an anionic, proton bound complex. [154–156] The case of solvation of water can thus be viewed as an extreme example of a generic solvent response by an anionic, proton bound complex.

2.3.5.2 Calculation of the Reaction Path for Water-Mediated Electron Capture by Py

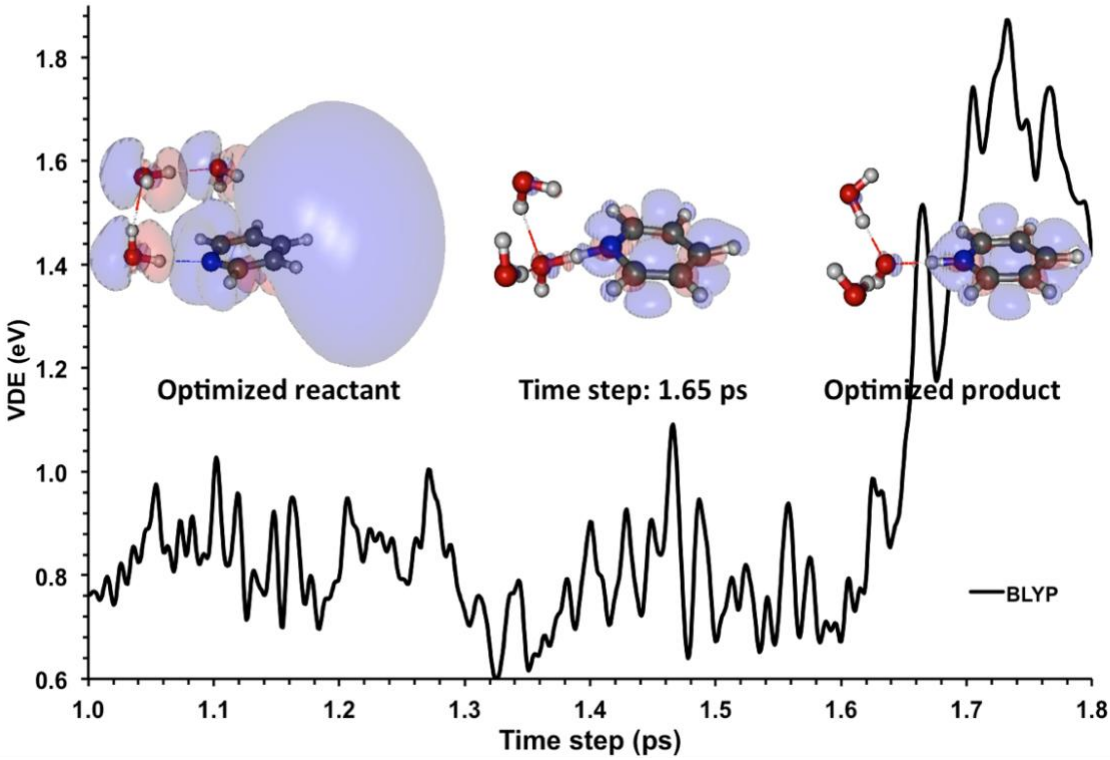

Figure 12: VDE of $[Py\cdot(H_2O)_n]^-$ along a BOMD trajectory with an initial kinetic energy consistent with T = 270 K. The MP2 level charge differences (anion - neutral) for the reactant, intermediate and product are displayed.

The preceding discussion emphasized the close energetic proximity of the $PyH\cdot(OH^-)\cdot(H_2O)_{n-1}$ and $Py^-\cdot(H_2O)_n$ valence-bond arrangements. There is actually a third low-lying valence-bond structure that corresponds to a dipole-bound $Py\cdot(H_2O)_n^-$ anion with a diffuse excess electron, which is expected to be involved in early stages of $(H_2O)_n^-$ + Py condensation. For example, our calculations indicate that excitation of one quanta into the NH or OH stretch vibrations of the most stable $PyH\cdot(OH^-)\cdot(H_2O)_2$ species would deposit sufficient energy for the system to sample such dipole-bound structures as exit channel configurations leading to electron

autodetachment. To further evaluate the dynamics of the interconversion between the $Py\cdot(H_2O)_3^-$ and $PyH\cdot(OH^-)\cdot(H_2O)_2$ structures, we performed Born-Oppenheimer molecular dynamics (BOMD) simulations on the $[Py\cdot(H_2O)_3]^-$ cluster (see Section II.C for details). Ten trajectories, four between 1 and 5.5 ps and six for between 14.7 and 19.3 ps, were run. Of these only two gave rise to the solvated OH^- ion, one near 16 ps and the other it occurred near 1.6 ps. In these simulations, the $Py\cdot(H_2O)_3^-$ isomer was heated to 270 K and changes to the geometry and electronic structure were recorded in 1 fs increments. An example video of one of these trajectories is given in the Supplemental material. [105] Figure 9 plots the electron binding energy along one of the trajectories together with the differences in the charge densities of the anion and neutral, calculated at the MP2/aug-cc-pVDZ [157,158] level, for the final, key intermediate, and product structures (MP2-level charge densities are employed rather than BLYP [58,126] charge densities as the MP2 method is expected to give more reliable charge distributions). For the indicated trajectory, the electron remains dipole bound to the $(H_2O)_3$ water network for about 1.65 ps, before evolving into an intermediate structure of the form $Py^-\cdots H^+\cdots OH^-(H_2O)_2$. This is followed by rapid formation of the pyridinium radical $PyH\cdot(OH^-)\cdot(H_2O)_2$. In the product structure both an electron and a proton have transferred to the Py, with the former occupying the π^* LUMO of the neutral Py molecule. Evolution to the product $PyH\cdot(OH^-)\cdot(H_2O)_2$ structure requires the two H_2O monomers to adopt an arrangement that effectively solvates the OH^-. For the indicated trajectory, the system rapidly evolves from the intermediate to the product, although for other trajectories (not shown) there are fluctuations between the intermediate and reactant-like $Py\cdot(H_2O)_3^-$ structures before the product is accessed. As seen in Figure 11, the electron binding energy increases as the $PyH\cdot(OH^-)\cdot(H_2O)_2$ product is formed, approaching a VDE similar to that observed from the photoelectron spectrum (1.53 eV).

2.4 Conclusions

Gas phase cluster chemistry, together with analyses of the pre-dissociation and photoelectron spectroscopies with electronic structure calculations, have been used to clarify the chemical rearrangements that occur when pyridine (Py) combines with hydrated electron clusters $(H_2O)_n^-$ for n = 3-5. The photoelectron spectrum of the resulting $[Py\cdot(H_2O)_n]^-$ species supports the presence of a valence anion, in which the VDE is much greater than its AEA. Analysis of the vibrational patterns then confirms the formation of neutral pyridinium radical $PyH_{(0)}$ and hydrated hydroxide, where the neutral radical occupies one of the sites in the primary solvation shell around the hydroxide anion: $PyH\cdot(OH^-)\cdot(H_2O)_{n-1}$. Synthetic access to this arrangement now presents an attractive opportunity to follow the reaction chemistry of the $PyH_{(0)}$ radical in the microhydration regime. A particularly timely choice in this regard is the activation of CO_2 by proton coupled electron transfer, which has been proposed for the catalytic activity of Py by Musgrave [159] and Bocarsly. [160]

2.5 Acknowledgements

This work was supported the by Mississippi Center of Supercomputing Research and the National Science Foundation under Grant Numbers CHE-1338056 (G.S.T.) and CHE-0955550 (N.I.H). Both G.S.T. and N.I.H. acknowledge NSF EPSCoR support under grant no. EPS-0903787. M.A.J. and K.D.J want to thank the U.S. Department of Energy for support under grant DE-FG02-06ER15800 and DE-FG02-06ER15066. M.A.J. also expresses gratitude to the staff and facilities of the Yale University Faculty of Arts and Sciences High Performance Computing

Center, and NSF grant CNS 08-21132, which partially funded acquisition of the facilities. KDJ also acknowledges use of computational facilities in the University of Pittsburgh's Center for Simulation and Modeling.

3.0 Proton-Coupled Electron Transfer in [Pyridine •($H_2O)_n]^-$, n = 3, 4, Clusters

This work was published as: Kaye A. Archer, Kenneth D. Jordan, Chem. Phys. Lett, Vol. 661, 196-199 (2016)

3.1 Introduction

The equation-of-motion method is used to map out one-dimensional potentials for proton-coupled electron transfer in the [pyridine • $(H_2O)_n$] – , n = 3, 4, clusters. In both cases there is an avoided crossing between valence-type pyridinyl•(OH^-) $(H_2O)_{n-1}$ and dipole–bound pyridine • $(H_2O)_n$ – anion species. For the n = 3 cluster, the mixing is sufficiently strong that both limiting structures are predicted to be sampled in the vibrational zero-point level.

The anions of pyridine•$(H_2O)_n$ clusters, $[Py•(H_2O)_n]^-$, have been the subject of experimental and theoretical investigation. [111,161,162] These are intriguing and challenging systems because of the possibility of three different types of anions that are expected to be close in energy. The limiting cases are $Py•(H_2O)_n^-$ in which the excess electron is dipole bound [88,163], $Py^-•(H_2O)_n$ in which the excess electron is localized in a valence π* orbital of the pyridine, and the PyH•(OH^-)•$(H_2O)_{n-1}$ species formed by proton-coupled electron transfer (PCET) from $(H_2O)_n^-$ to pyridine. The isolated Py^- ion is unstable with respect to electron detachment, lying 0.62 eV in energy above the ground state of the neutral pyridine molecule [164], but upon sufficient solvation it will become stable, with respect to electron detachment. Figure 13 schematically reports the relative energies of the various fragments and products for the n = 3 cluster. The $(H_2O)_3^-$ dipole-

bound anion has a vertical detachment of 0.13 eV and is nearly isoenergetic with the global minima structure of the neutral $(H_2O)_3$ cluster. [146] In the case of the $Py^{-} \cdot (H_2O)_3$ and $Py \cdot (H_2O)_3^{-}$ complexes, the energies of the unmixed diabatic states were obtained from constrained geometry optimizations.

The photoelectron spectra of the $[Py \cdot (H_2O)_3]^{-}$, $n \geq 3$, clusters are consistent with $PyH \cdot (OH^{-}) \cdot (H_2O)_{n-1}$ structures. However, the vibrational spectrum of the $n = 3$ anion is fundamentally different from that of the $n = 4$ and 5 anions in the region of the NH stretch. Specifically, the spectrum of the $n = 3$ anion is fundamentally different from that of the $n = 4$ and 5 anions in the region of the NH stretch. Specifically, the spectrum of the $n = 3$ cluster displays three broad features with ~350 cm^{-1} spacing (~2050, 2400, 2750 cm^{-1}) while for the $n = 4$ and 5 clusters, the vibrational structure in the NH stretch region consists of a very broad feature peaked near 2600 cm^{-1}. These results suggest a change in the electronic structure of the cluster in going from $n = 3$ and $n = 4$.

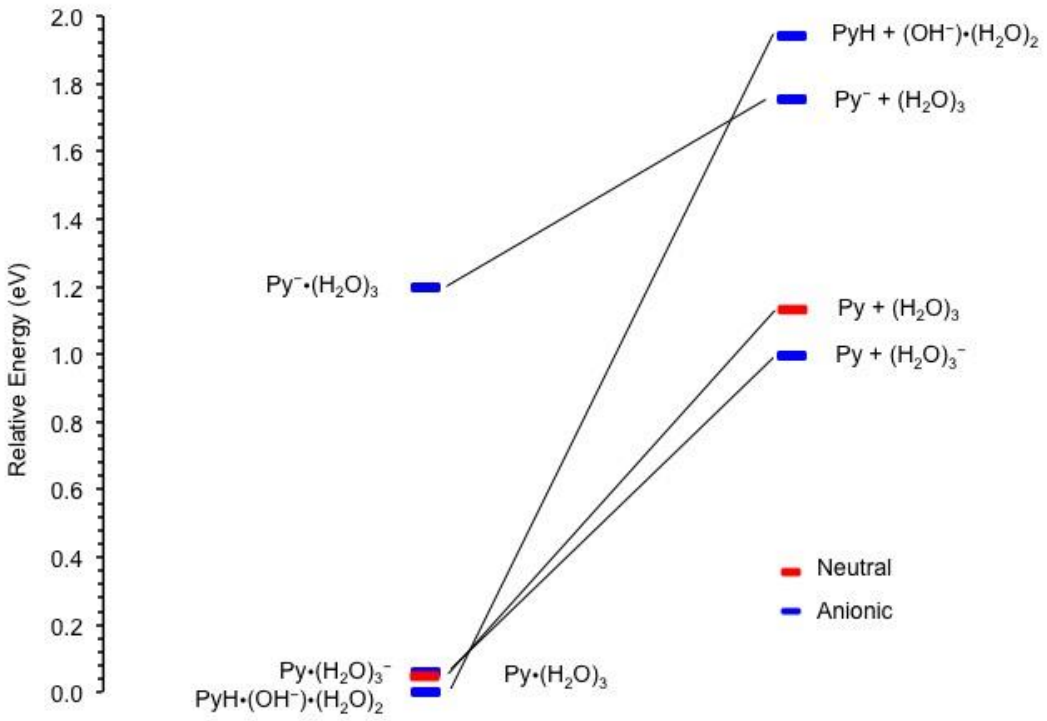

Figure 13: Energies of the various non-interacting fragments as well as of the possible products of the [Py • $(H_2O)_3$]$^-$ cluster. The energies of the neutral species were calculated using the MP2 method, and those of the anionic species were calculated using the EA-EOM-CCSD(2) method. All calculations employed the aug-cc-pVDZ+7s7p basis set, described in the text.

In this work we present electronic structure calculations on [Py•$(H_2O)_3$]$^-$ and [Py • $(H_2O)_4$]$^-$ to better understand how these species evolve along the proton transfer coordinate. These clusters pose a significant challenge to theory. Specifically, density functional methods, even with the inclusion of exact exchange, tend to strongly over-bind dipole-bound anions with the basis sets typically used for such systems, and the spin-unrestricted Hartree-Fock method suffers from sizable spin contamination for the various [Py•$(H_2O)_n$]$^-$ structures calling into question the validity of spin-unrestricted second-order Møller-Plesset (MP2) [165–167]calculations. The spin-restricted (MP2) [168] method avoids the spin-contamination problem, but application of this approach to the [Py•$(H_2O)_3$]$^-$ system gave a discontinuous potential energy curve as a result of the restricted

Hartree-Fock (RHF) calculations converging to different solutions at different geometries. To avoid this problem, we adopt the EA-EOM-CCSD(2) method. [4,5] In this approach one carries out MP2 calculations on the neutral closed-shell cluster, and the resulting doubles [86,169] amplitudes are used to carry out a similarity transformation of the Hamiltonian, which, in turn, is used to carry out one-particle (1*p*) plus two-particle-one-hole (2*p*1*h*) configuration interaction calculations on the anion states.

The present investigation, thus, has two goals: (1) to provide insights into the difference in the electronic structure of the *n*=3 and 4 clusters and the implications of this difference on the vibrational spectra, and (2) to provide benchmark electronic structure results for assessing the performance of more approximate electronic structure methods for describing proton-coupled electron transfer in anionic complexes.

3.2 Computational Details

The EA-EOM-CCSD(2) calculations were carried out using the CFOUR code [170] and employed the aug-cc-pVDZ basis set [171,172] supplemented with a set of 7s7p diffuse functions. [173] The exponents of the supplemental functions were chosen to be in a geometric ratio of 3.33, with the tightest of these functions having exponents 3.33 times smaller than those of the corresponding "aug" functions. The supplemental diffuse functions were centered on the C atom situated opposite the N atom of the pyridine ring and were included primarily for the purpose of describing dipole-bound anions. For the PyH•(OH^-)•$(H_2O)_2$ form of the n=3 cluster, EA-EOM-CCSD(2) calculations were also carried out with the aug-cc-pVTZ basis set [171,172] supplemented with the 7s7p set of diffuse functions [174] in order to check the convergence of the

electron binding energy with basis set expansion. Starting with the $PyH•(OH^-)•(H_2O)_{n-1}$ species, optimized using the ROHF-MP2 method as implemented in GAMESS [175,176] in the frozen core

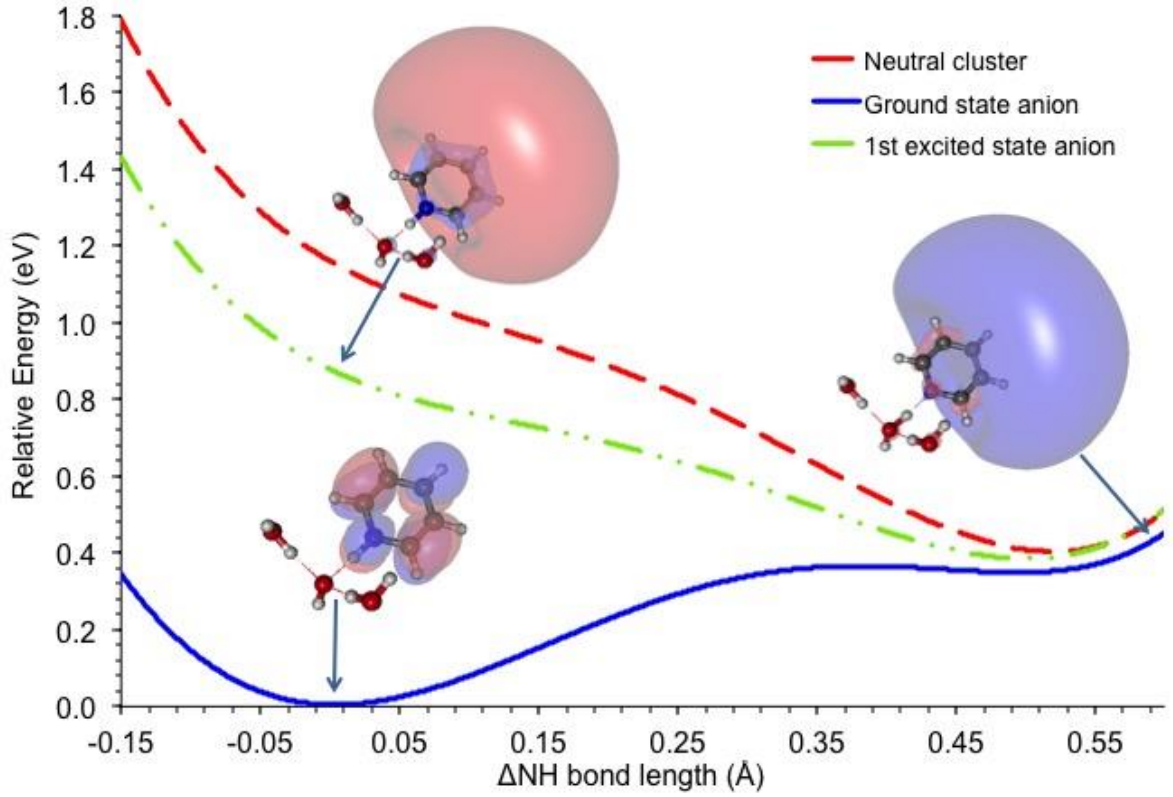

Figure 14: One-dimensional potential energy curves for the $PyH•(OH^-)•(H_2O)_2 \rightarrow Py • (H_2O)_3^-$ rearrangement. The energies of the anion states were calculated using the EOM-EA-CCSD(2) method, using the aug-cc-pVDZ+7s7p basis set, with the starting structure being that of $PyH•(OH^-)•(H_2O)_2$ optimized using the ROMP2 method. At each step along the reaction coordinate, the MP2 energy of the neutral cluster is also reported. There is an avoided crossing between the valence-like and dipole-bound anions near ΔNH = 0.45 Å.

approximation, a series of single-point calculations, in which the shared proton was moved along the line connecting the N atom of the pyridine ring and the O atom of the OH^- ion, were carried out. The resulting potential energy curves for the n = 2 and n = 3 clusters are shown in Figure 14 and Figure 15, respectively. The figures also display the dominant natural orbitals for the unpaired electron as obtained for the EOM calculations.

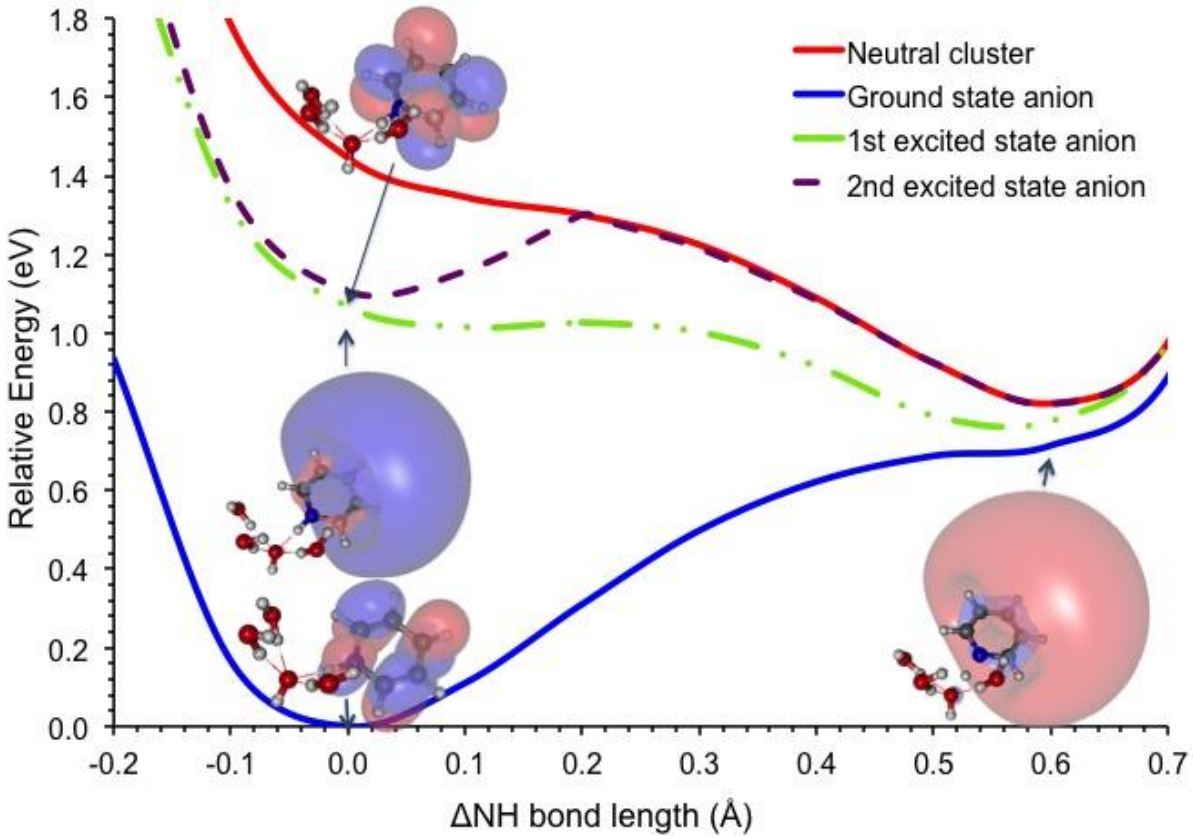

Figure 15: One-dimensional potential energy curves for the PyH•(OH–) • $(H_2O)_3$ → Py • $(H_2O)_4$– rearrangement. The energies of the anion states were calculated using the EOM-EA-CCSD(2) method, using the aug-cc-pVDZ+7s7p basis set. The initial structure of PyH • (OH–) • $(H_2O)_3$ was optimized using the ROMP2 method. At each step along the reaction coordinate, the MP2 energy of the neutral cluster is reported. There is an avoided crossing between the lowest valence-type and dipole-bound anion near ΔNH = 0.60 Å.

3.3 Results

At the minimum energy structure of the n = 3 anion, the calculated vertical detachment energy (VDE) at the EOM-EA-CCSD(2)/aug-cc-pVDZ+7s7p level is 1.16 eV, as compared to the experimental result 1.56 eV. Upon enlarging the basis set to aug-cc-pVTZ+7s7p, the calculated

vertical detachment energy increases to 1.35 eV, in reasonable agreement with experiment. At this geometry there is also a dipole-bound anion lying energetically about 0.3 eV below the neutral cluster. The natural orbitals associated with the unpaired electron are also shown in Figure 14. As the proton is displaced along the reaction coordinate (from the $PyH•(OH^-)•(H_2O)_2$) starts near 0.26 eV, which implies that the ν=1 level of this vibration lies about 0.4 eV above the potential energy minimum. Thus, as seen from Figure 14, the vibrational excited state of the anion samples the $Py(H_2O)_3^-$ structure.

The potential energy curves depicted in Figure 14 were generated by simply stretching the NH bond, keeping all other degrees of freedom frozen. Separate calculations indicate that the energy of the neutral cluster drops by 0.40 eV upon geometry relaxation. At the potential energy minimum of the neutral, ΔNH = 0.77 Å, and at the geometry the dipole-bound anion is calculated to lie only by 0.03 eV below the neutral. Thus, on the relaxed potential the dipole-bound anion near ΔNH = 0.77 Å would be expected to lie only a few hundredths of an eV above the $PyH • (OH^-)•(H_2O)_2$ species at its optimized structure. We have optimized the geometry of the anion at the ROMP2 level for ΔNH values between -0.2 and 0.35 Å. The relaxed potential has a barrier of ~0.12 eV near ΔNH = 0.25 Å. This result establishes that, both limiting $PyH • (OH^-) • (H_2O)_2$ and $Py • (H_2O)_3^-$ configurations are sampled in the vibrational zero-point level of the n = 3 anion. This is consistent with the fact that the peak in the photodetachment spectrum for the n = 3 cluster extends from 0 to 2 eV. Our calculations also predict that autoionization should become an open channel for $PyH•(OH^-)•(H_2O)_2$ following excitation of one quanta of the NH stretch mode. The experimental vibrational spectrum of $[Py•(H_2O)_3]^-$ was obtained by use of Ar-tagged $[Py•(H_2O)_3]^-$•Ar cluster. For this species electron detachment is observed at energies above 0.4 eV, while at lower energies the vibrational excited anion decays by Ar-atom loss. The Ar atom is expected to

stabilize the valence anion state relative to the neutral cluster, acting so as to suppress the electron detachment channel. It is also likely that the Ar tag causes a reduction of the amount of Py • $(H_2O)_3^-$ character in the wavefunction for the ground state anion.

Interestingly, our calculations do not provide evidence for a bound $Py^-•(H_2O)_3$ ion. This suggests that this form of the anion, at least for the geometries considered, lies energetically above the neutral, and is thus subject to electron detachment. However, this temporary anion state could be involved in the initial electron capture with rapid decay to the dipole-bound and/or valence anion, and thus lead to the observed $PyH•(OH^-)•(H_2O)_2$ product. Calculations using the M06-2X density functional method [177], in contrast to those with the EA-EOM-CCSD (2) methods, predict the $Py^-•(H_2O)_3$ ion to be stable with respect to electron detachment. This appears to be an artifact of the DFT calculations. Table 2 summarizes experimental and calculated detachment energies of [pyridine• $(H_2O)_3$] $^-$ and [pyridine• $(H_2O)_4$] $^-$. Unless noted otherwise the M06-2X detachment energies were calculated using M06-2X optimized geometries and using the 6-31++G(d,p) basis set [122,178], and the EOM detachment energies were calculated using ROMP2 optimized geometries and the aug-cc-pVDZ+7s7p basis set. The exceptions are the M06-2X calculations on the $Py•(H_2O)_3^-$ form of the anion, which were carried out at the ROMP2 optimized geometry and the EOM calculations on the $Py^-•(H_2O)_3$ form of the anion, which were carried out at the M06-2X optimized structure. The M06-2X calculations predict the $Py^-•(H_2O)_3$ and $PyH•(OH^-)•(H_2O)_2$ species to be isoenergetic, with the $Py•(H_2O)_3^-$ form of the anion lying 0.13 eV higher in energy. In contrast the EOM calculations predict the $PyH•(OH^-)•(H_2O)_2$ form of the anion to be most stable, with the $Py•(H_2O)_3^-$ and $Py^-•(H_2O)_3$ forms lying, respectively, 0.06 eV and 0.12 eV higher in energy.

Table 2: Vertical detachment energies of [Py· $(H_2O)_3$]– and [Py· $(H_2O)_4$]–.

Cluster	Experimental (eV)		Isomer	Theory	
	Wang et al[a]	Deblase et al[b]		Wang et al M06-2X/6-31++G(d, p)	Current work EOM-EA-CCSD(2) aug-cc-pVDZ+7s7p
[Py· $(H_2O)_3$]-	0.75 1.56	1.53	Py–· $(H_2O)_3$	0.84	0.39[c]
			Py· $(H_2O)_3$–	0.74[d]	0.12
			PyH·OH–· $(H_2O)_2$	1.44	1.16(1.35[e])
[Py· $(H_2O)_4$]-	1.79	1.63	Py–· $(H_2O)_4$	1.33	–
			Py· $(H_2O)_4$–	–	0.71
			PyH·OH–·$(H_2O)_3$	1.7	1.45

a Ref.[179]

b. Ref.[180]

c. Calculated at the M06-2x/6-31++G(d,p) optimized geometry.

d. Calculated at the ROMP2/aug-cc-pVDZ optimized geometry.

e. The value in the parentheses was obtained using the aug-cc-pVTZ+7s7p basis set.

For the n = 4 cluster, the calculated vertical electron detachment energy at the minimum energy structure of the anion is 1.45 eV, which is in reasonable agreement with the experimental VDE value of 1.63 eV [179]. As for the n = 3 cluster, the adiabatic ground state of the anion of the n = 4 cluster evolves from valence-bound at ΔNH ~ 0 Å to dipole-bound at large ΔNH values (~0.6 Å). The energy of the n = 4 cluster drops by 0.50 eV when the geometry is fully relaxed. At the relaxed geometry ΔNH = 0.85 Å. Thus, the relaxed potential for proton transfer in the ground state anion is much steeper for the n = 4 than for the n = 3 anion. As a result, the cluster in its zero-point level is essentially PyH • (OH^-) • $(H_2O)_3$ in nature, but in its v = 1 NH stretch level, it could acquire a small amount of dipole-bound anion character. From Figure 15 it is seen that in addition to the ground state valence-type anion and the dipole-bound anion, the n = 4 cluster also has a bound excited state valence-type anion, in which the excess electron occupies the second lowest lying π* orbital of the pyridine ring.

3.4 Conclusion

Our calculations of the potential energy curve for proton transfer in [Py • $(H_2O)_3$] – provide evidence that even in its vibrational zero-point level the anion samples both the dipole-bound Py • $(H_2O)_3^-$ and valence-type PyH • (OH^-) • $(H_2O)_2$ configurations. This conclusion is consistent with the complex vibrational spectrum observed for the anion in the [Py • $(H_2O)_3$]– cluster. The presence of the additional water molecule in [Py • $(H_2O)_4$]- causes the PCET limiting structure to be preferentially stabilized with respect to the dipole-bound anion [compared to $Py(H_2O)_3^-$]. At the ROMP2 level of theory the preferential stabilization is about 0.21 eV. This suppresses the large amplitude motion along the proton transfer coordinate and the sampling of dipole-bound structures in the zero-point and first vibrationally excited (NH stretch) levels. While M06-2X calculations indicate that the strong mixing between Py^- • $(H_2O)_3$ and PyH • (OH^-) • $(H_2O)_2$ the present EA-EOM-CCSD (2) calculations indicate that the strong mixing is between the Py • $(H_2O)_3^-$ and PyH • (OH^-) • $(H_2O)_2$.

3.5 Acknowledgments

This research was carried out with the support of the DOE, under grant number DE-FG02-06ER15066. The calculations were carried out on computers in the University of Pittsburgh's Center for Simulation and Modeling. We acknowledge valuable discussions with M. Johnson.

4.0 Mapping the Potential Energy Surface of $H^+(H_2O)_{21}$

4.1 Introduction

The $H^+(H_2O)_{21}$ cluster is a magic number cluster [181], which has been the subject of much theoretical and experimental investigation [92,181,190–199,182,200–209,183,210–213,184–189]. Mapping the potential energy surface of $H^+(H_2O)_{21}$ can offer physical insights that can serve to explain the OH stretch peaks observed experimental IR spectra. [130] Proton transfer is known to proceed via hydrogen-bond networks. Therefore, an effective model for mapping the $H^+(H_2O)_{21}$ potential energy surface should allow for proton transfer and subsequent polarization of the electronic distribution. An appropriate model for proton transfer should allow the excess proton to be associated with different water monomers. [214] Multistate empirical valence-bond theory [10,98,214–216] describes molecular systems as linear combinations of (chemically motivated) valence-bond states. In the present study the multistate empirical valence-bond (MS-EVB) model incorporates the TIP3P [94,95,97,98] water model (MS-EVB/TIP3P).

The surface-bound hydronium, due to its interaction with the water molecules of its solvation shells, is subjected to an electric field that causes a redshift of the hydronium infrared peaks in $H^+(H_2O)_{21}$ [217]. Jordan et al. [217] demonstrated that when the interaction of the first and second solvation shells with hydronium were considered, the hydronium peaks in $H^+(H_2O)_{21}$ IR spectra are reproduced. The dispersion energy contribution to the total interaction energy also converges with the inclusion of water monomers located in the first and second solvation shell. [217] For improved accuracy, we consider empirical valence-bond (EVB) states where the excess proton is localized on water molecules in the first three solvation shell. Doubly nudged elastic

band (DNEB) [218] is employed to calculate the minimum energy isomerization pathway between two minima presented in literature. [219] Intermediate states from an isomerization pathway generated at MS-EVB/TIP3P level of theory are re-optimized at B3LYP-D3 [59,220,221]/6-31+G(2d, p) level of theory. The comparison of the geometry configurations of intermediate states and energetic ordering at MS-EVB/TIP3P and B3LYP-D3/6-31+G(2d,p) levels of theory will serve as a feasibility study of the appropriateness of the MS-EVB/TIP3P approximation for mapping the potential energy surface of $H^+(H_2O)_{21}$.

DNEB, as implemented in the OPTIM software package [93], is employed to carry out a double ended search between two known extrema, in this study, two minima. The pathlength between the extrema is minimized (in Euclidean space). A series of images is generated via linear interpolation between the coordinates of the endpoints, to discretize the pathway. Each image is a vector that describe geometry configurations along the DNEB pathway. Adjacent images are connected by springs; springs ensure that images are equidistant on the DNEB pathway. Limited–memory BFGS [222] was used to relax the DNEB pathway to the minimum energy pathway. Hybrid eigenvector following, EF/L–BFGS, was employed to refine the transition states.

Low-energy isomers have been identified by Christie et al. [130] utilizing density functional theory (DFT) and by Xantheas [219] using second-order Møller-Plesset theory (MP2). [81,153,223–226] The present study employs multistate empirical valence-bond (MS-EVB) theory of Voth et al. [98] This iteration of the MS-EVB potential employs a flexible TIP3P force field. Since TIP3P is meant as a water model, point (permanent) dipoles were introduce into the MS-EVB/TIP3P to accommodate the response of the electronic degrees of freedom due to the presence of a mobile excess proton. [98,227] MS-EVB can be viewed as being a mixed quantum mechanics /molecular mechanics (QM/MM) approximation.

4.2 Computational Details

The OPTIM package of Wales et al. [93] was employed to calculate the minimum energy isomerization pathway. MS-EVB/flexible TIP3P of Voth et al. was chosen to evaluate the potential energy surface. LBFGS was employed to converge minima and hybrid eigenvector-following/ LBFGS was employed to refine transition states. Changes to NEB parameters such as the number of images (this influences pathway resolution), the connection algorithm, cost function (weights connection attempts of minima closer in Euclidean space as more important), and BFGS step size, and NEB forces impact which isomerization pathway is found. Preference is given to shorter path lengths via the Dijkstra [228] weighted completeness graph approach, the lowest isomerization energy pathway is therefore not guaranteed. While each pathway appears to be reasonable, there seems to be no systematic way to optimize parameters in order to guarantee that the minimum energy isomerization pathway is found. Therefore, a methodical approach to NEB parameter convergence is not apparent

4.3 Results

Due to the complexity of the $H^+(H_2O)_{21}$ potential energy landscape, many isomerization pathways (transforming the Christie et al. isomer into the Xantheas isomer), with transition states occurring in the same energy regime, are feasible. Twenty-five distinct isomerization pathways with transition states no more than 9 kcal mol^{-1} above the Christie et al. isomer (which we will refer to as Isomer 1) and the Xantheas minima (which we will refer to as Isomer 2) have been identified. Several isomerization pathways overlap i.e., have many of the same transition states

and intervening intermediate states. The calculated isomerization pathways have between 7 and 22 transition states. The DNEB calculations uncovered 350 unique minima, 89 of which function as intermediate states on the isomerization pathways shown below in Figure 16. The other 261 minima are connected to only one intermediate state (rather than the requisite two needed for it to feature in the isomerization pathway) along the isomerization pathways presented. This occurred because the DNEB algorithm, as implemented in the OPTIM software package, [93] first finds transition states, it then proceeds to calculate minima directly connected to the transition states (forming a set of minima-transition-minima segments). Finally, these segments are connected to form the entire isomerization pathways (this allows for local minima which are not featured on the isomerization to be found).

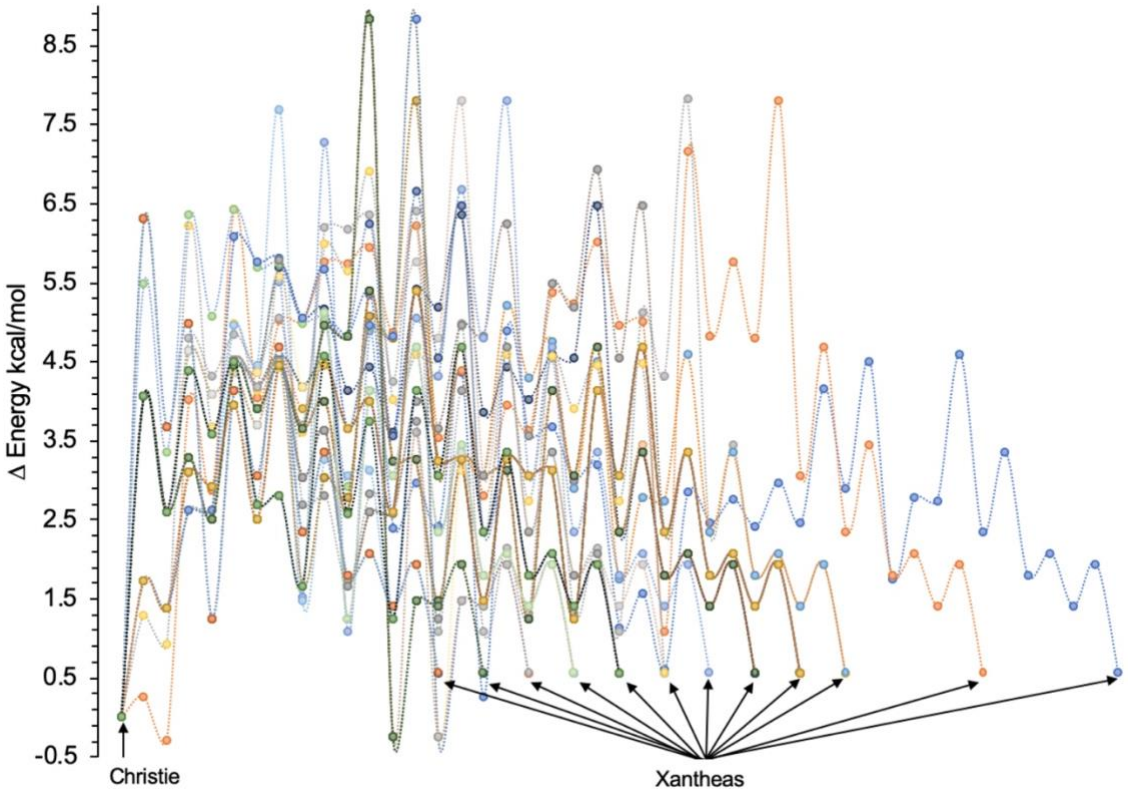

Figure 16: Isomerization pathways of differing lengths for the transformation of the H+(H2O)21 isomer found by Christie et al. [130] to the isomer found by Xantheas. [219]

Represented below is a pathway which has 13 intermediate states with the highest intervening transition state located 5.40 kcal mol^{-1} above Isomer 1 (see Figure 17). On the MS-EVB/flexible TIP3P PES Isomer 2 is located 0.55 kcal mol^{-1} above Isomer 1. It should be noted that when Isomers 1 and 2 are compared, there are 7 water molecules oriented differently in pentagonal rings (see Figure 18), while the donor – acceptor (hydrogen-bond) arrangements of the hydronium and every other water molecule remain the same (see the first and last columns of Table 3 and Table 4).

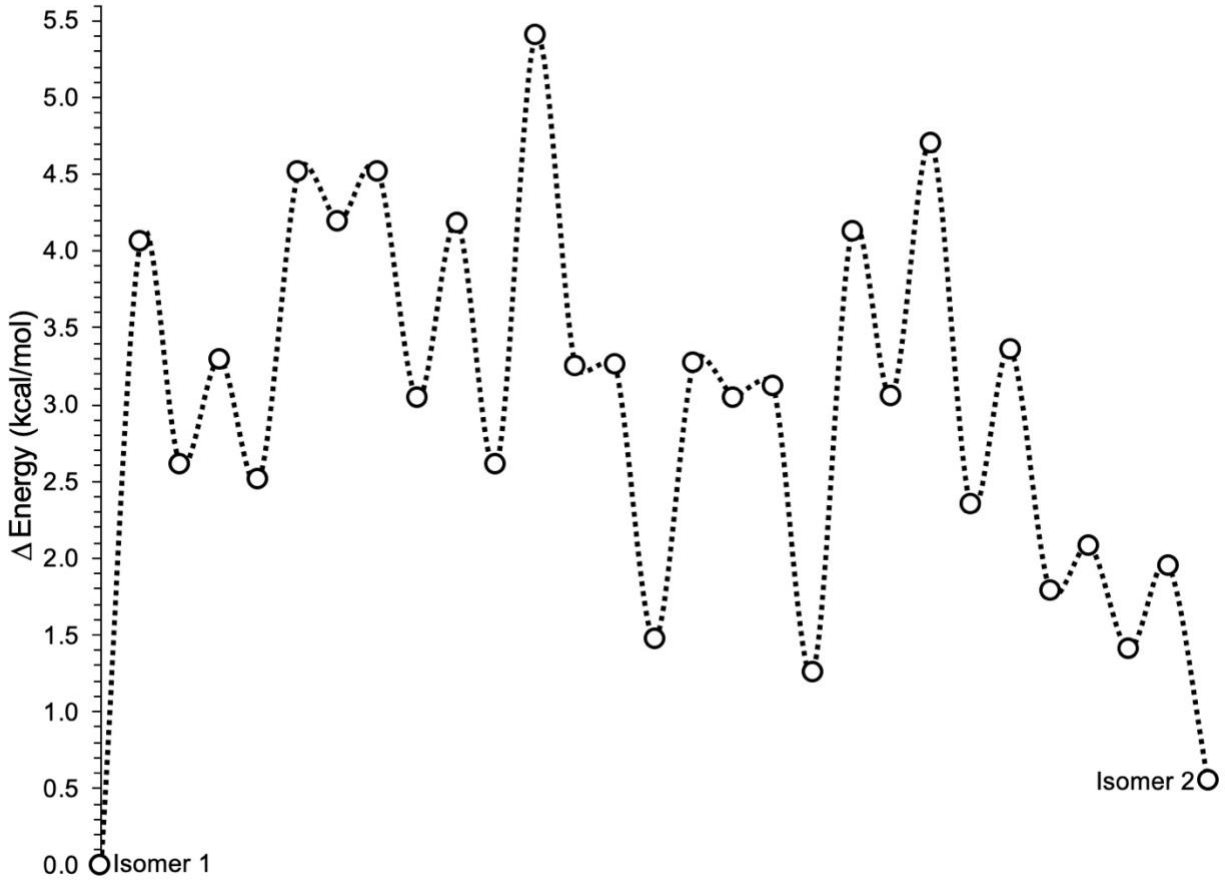

Figure 17: Isomerization pathway between the minima of Christie et al. [130] and Xantheas. [219]

Changes to these 7 water molecules impact the donor – acceptor motif of 8 waters along the minimum energy isomerization pathway. The isomerization pathway is characterized by concerted rotation of 7 water molecules which results in hydrogen-bond formation and breaking. Each consecutive intermediate state results from a net of no more than one broken or formed hydrogen-bond (relative to the previous intermediate). Table 3 and Table 4 document donor – acceptor motif changes of the intermediate states along the isomerization pathway. Figure 20 demonstrates how the geometric configuration changes along one isomerization pathway.

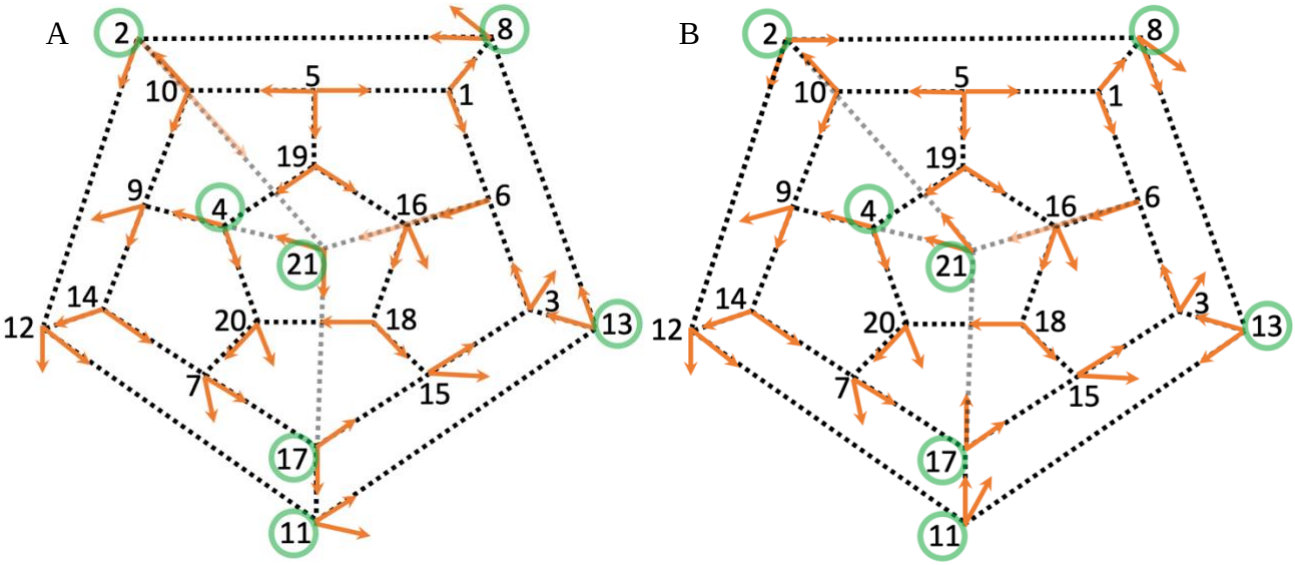

Figure 18: Comparison of Isomers 1 (panel a) and 2 (panel b) molecular arrangement. The internal H_2O is labeled 21; H_3O^+ is labeled 5. The 3D $H^+(H_2O)_{21}$ molecule is represented by a 2D structure where the dotted lines indicate hydrogen bonds and the orange arrows indicate O-H bonds (originating on O atoms and terminating on H atoms). The lighter lines indicate H-bonds to the central water monomer (labeled 21). The green circles identify water monomers that undergo changes to the H-bond motif on the isomerization pathway.

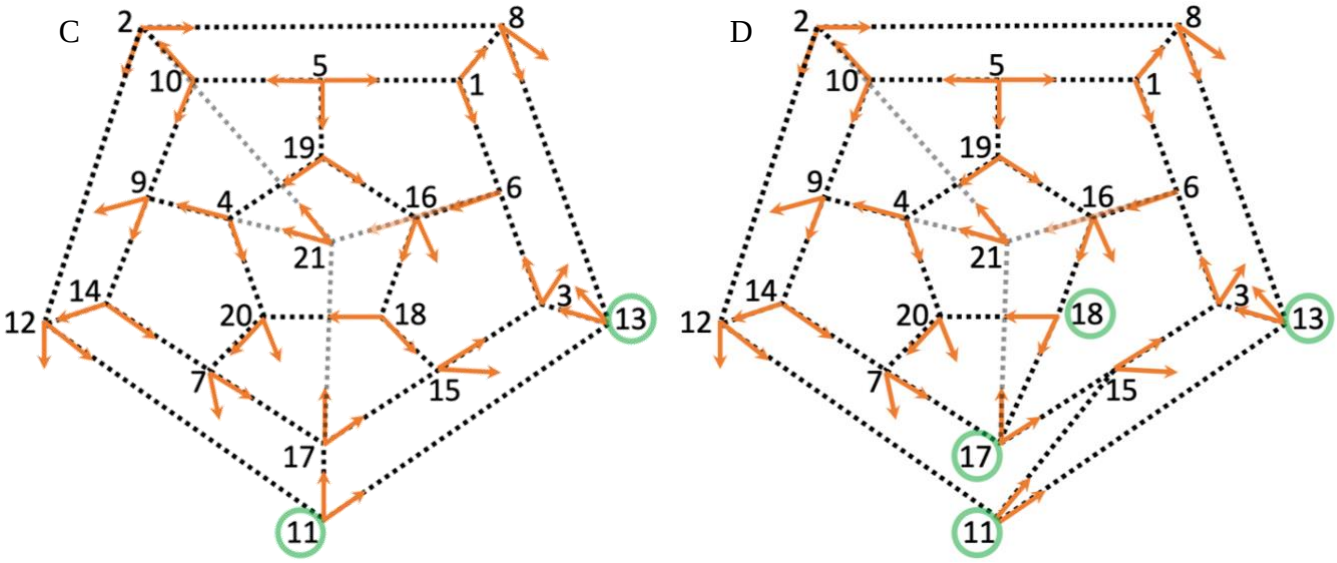

Figure 19: Comparison of Isomers 3 (panel a) and 4 (panel b). On the MS-EVB/TIP3P potential energy surface Isomers 3 & 4 are lower in energy than Isomers 1 & 2. The green circles identify differences in the H-bond motif when compared to Isomer 2.

Table 3: Donor - acceptor motif along minimum energy isomerization pathway. A, D and d represents acceptor, donor and dangling O-H bonds respectively. * identifies the trapped H_2O molecule. Green indicates motif changes relative to previous intermediate state.

Oxygen Center	Isomer 1	Intermediate states													Isomer 2
		1	2	3	4	5	6	7	8	9	10	11	12	13	
O-02	AADD	AAD*d*	AAD*d*	AAD*d*	AAD*d*	AAD*d*	AADD	AADD	AADD	AADD	AADD	AADD	AADD	AADD	AADD
O-08	AAD*d*	AAD*d*	AAD*d*	AAD*d*	AAD	AD*d*	AAD*d*	AA*dd*	AAD*d*	AAD*d*	AAD*d*	AAD*d*	AAD*d*	AAD*d*	AAD*d*
O-10	ADD	ADD	ADD	ADD	ADD	AADD	ADD	ADD	ADD	ADD	ADD	ADD	ADD	ADD	ADD
O-11	AAD*d*	AAD*d*	AD*d*	AD*d*	AAD*d*	AD*d*	AAD*d*	AD*d*	AD*d*	AAD*d*	AD*d*	ADD	AD*d*	AD*d*	AAD*d*
O-13	ADD	ADD	AADD	AADD	AADD	AADD	AADD	AADD	AAADD	AADD	AADD	AADD	ADD	AD*d*	ADD
O-17	AADD	AADD	AADD	ADD	ADD	ADD	ADD	ADD	ADD	ADD	ADD	AADD	AAADD	AADD	AADD
O-18	ADD	ADD	ADD	AADD	AADD	ADD	ADD	ADD	ADD	ADD	ADD	ADD	ADD	ADD	ADD
O-21*	AADD	AAD	ADD	ADD	AADD	AADD	AADD	AADD	AADD	AADD	AAADD	AAADD	AADD	AADD	AADD

Table 4: Donor – acceptor motif of water monomers of intermediate states that remain the same on the isomerization pathway. * identifies the H_3O^+.

Oxygen Center	Acceptor-Donor Motif
O-01	ADD
O-03	AAD*d*
O-04	AADD
O-05*	DDD
O-06	AADD
O-07	AAD*d*
O-09	AAD*d*
O-12	AAD*d*
O-14	ADD
O-15	AAD*d*
O-16	AAD*d*
O-19	ADD
O-20	AAD*d*

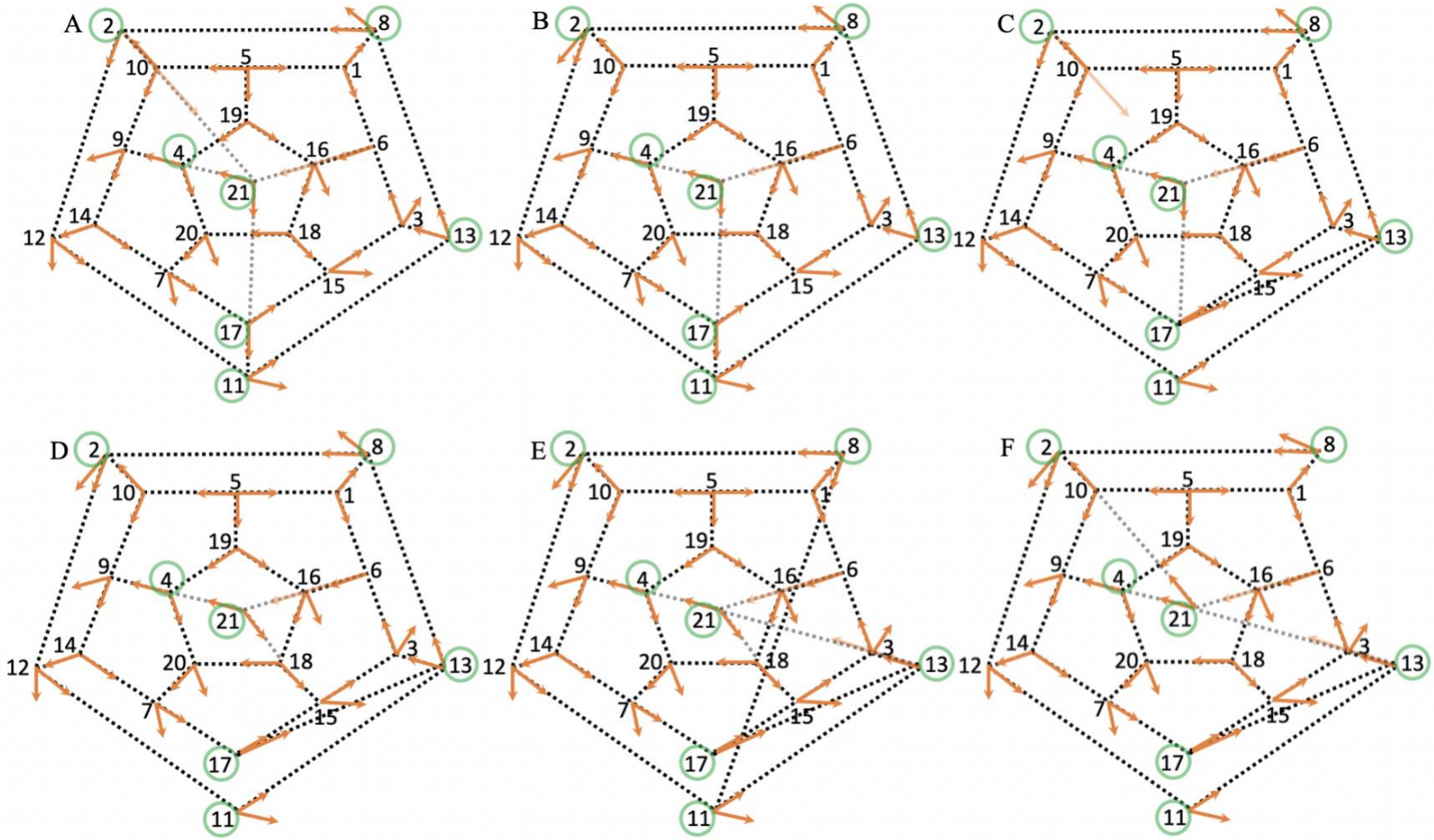
A
B
C
D
E
F
2
8
5
10
1
19
9
4
16
6
21
14
20
18
3
12
13
7
15
17
11

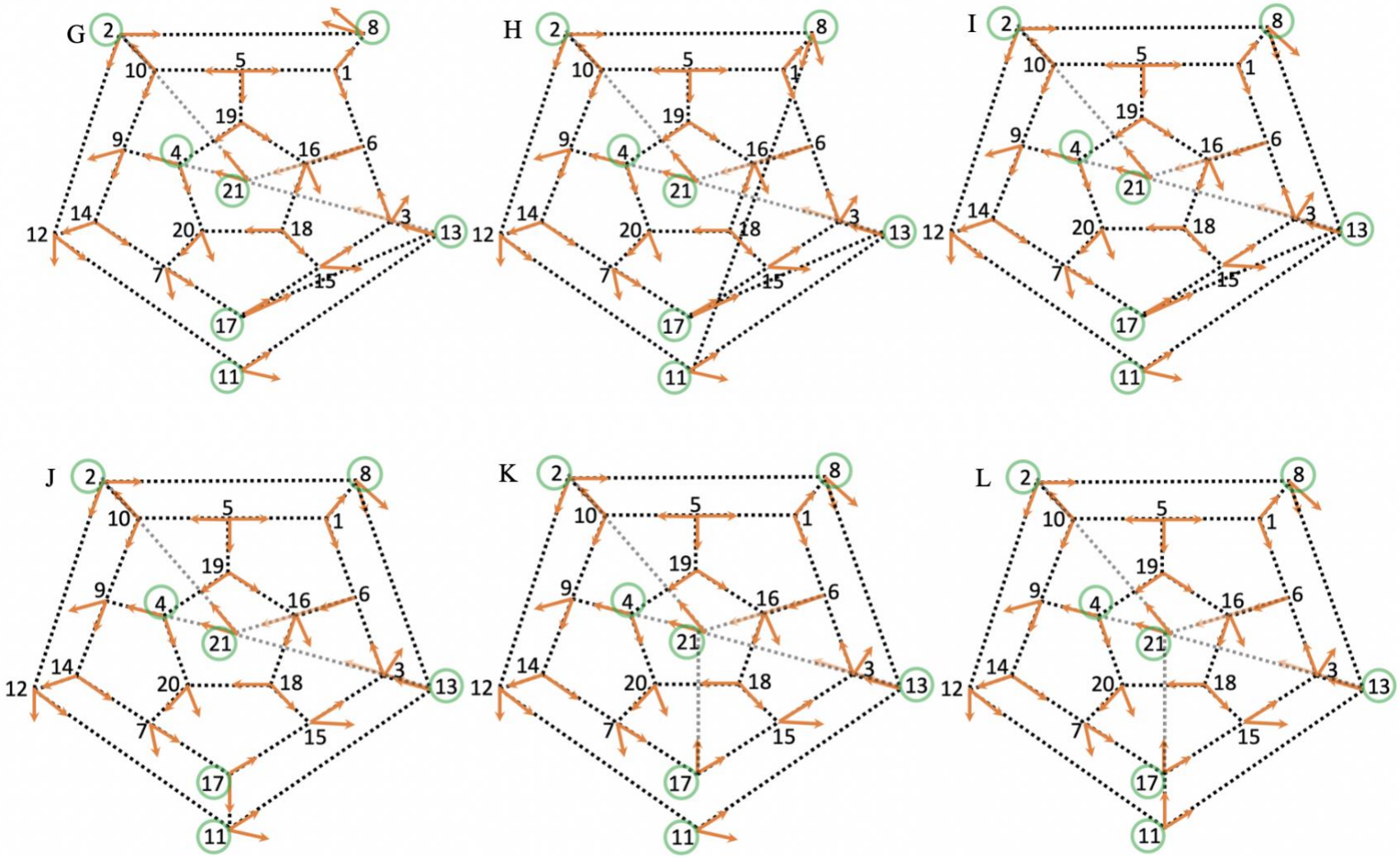
G
H
I
J
K
L
2
8
5
10
1
19
9
4
16
6
21
14
3
12
13
20
18
7
15
17
11

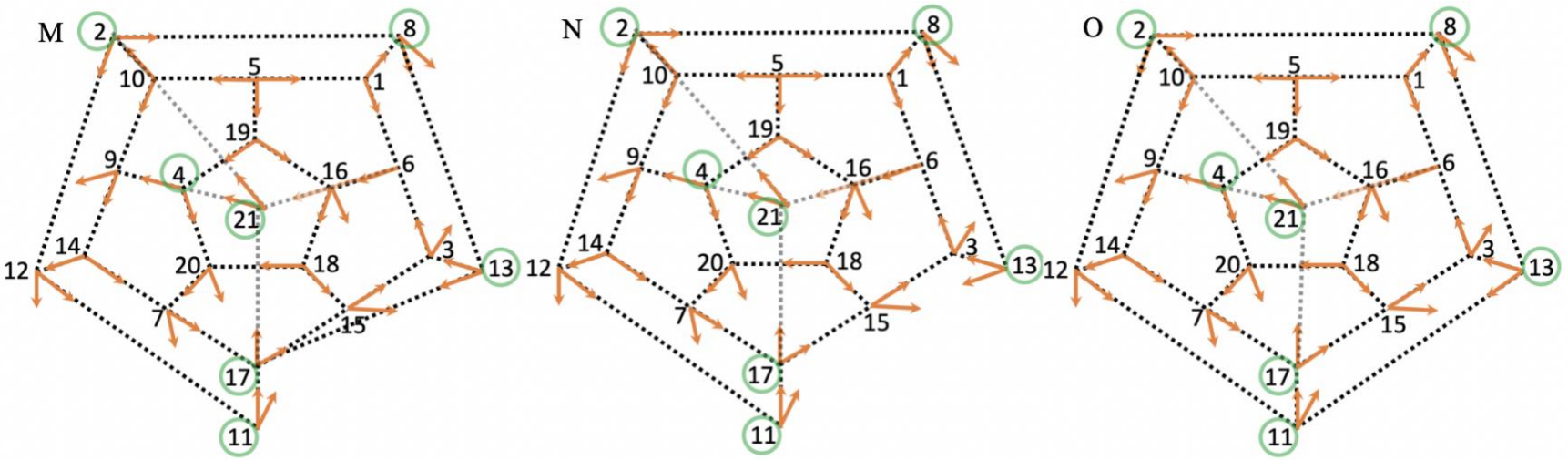

Figure 20: Comparison of isomer geometry along the minimum energy isomerization pathway. A and O are Isomers 1 and 2 respectively. B - N are intermediate states. The green circles identify the monomers that experience changes to their hydrogen-bond motif along the isomerization pathway.

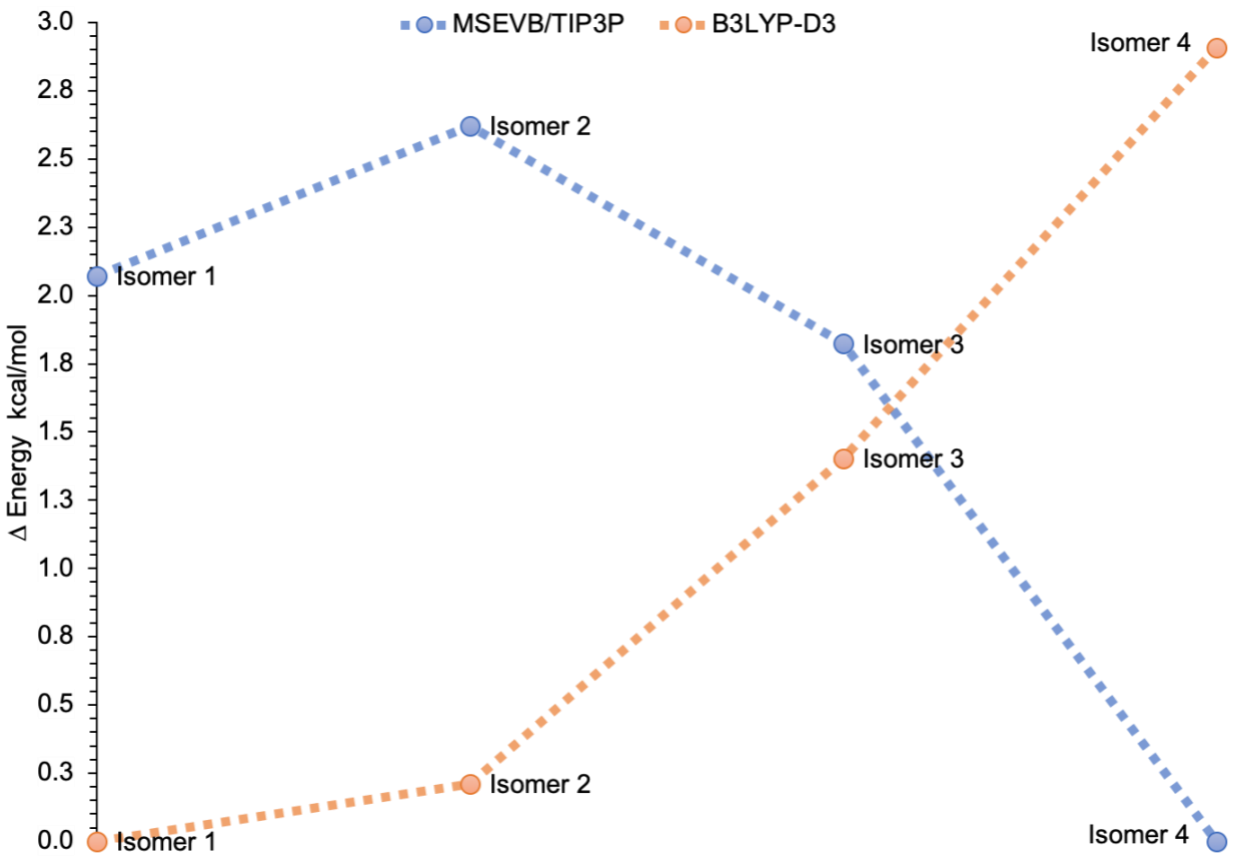

Figure 21: Comparison of isomer ordering at the MS-EVB/TIP3P and B3LYP-D3 levels of theory.

Two intermediate states (which we have designated Isomers 3 and 4) that were found on one of the isomerization pathways) are lower in energy than Isomer 1 and 2, see Figure 19. Isomer 3 is most similar to Isomer 2 with the only difference being that the acceptor – donor motif of two waters molecules are interchanged (labelled 11 and 13 – in isomer 2 monomer 13 is ADD and monomer 11 is AD with a dangling O–H bond, isomer 3 the acceptor – donor motif is reversed). Isomer 4 has two tetragonal rings and two hexagonal rings (see Figure 19). These geometries were re-optimized at the B3LYP-D3/6-311+G(2d,p) level of theory. On the MS-EVB/TIP3P potential energy surface Isomer 2 of Xantheas is 0.55 kcal mol^{-1} above Isomer 1 of Christie et al, while at B3LYP-D3/6-311+G (2d, p) level of theory Isomer 1 is 0.21 kcal mol^{-1} above Isomer 2. On the MS-EVB/TIP3P potential energy surface Isomer 3 is 0.25 kcal mol^{-1} below Isomer 1, while at

B3LYP-D3/6-311+G(2d,p) level of theory Isomer 3 is 1.40 kcal mol^{-1} above Isomer 2 (see Figure 21). Isomers 3 and 4 are higher in energy than isomers 1 and 2 at B3LYP-D3/6-311+G(2d,p) level of theory while the reverse is true on the MS-EVB/TIP3P potential energy surface. While the pathway presented above seems reasonable as an isomerization pathway, the MS-EVB/flexible TIP3P potential energy surface does not reproduce the energetic ordering of B3LYP-D3/6-311+G (2d,p) level of theory as shown in Figure 22.

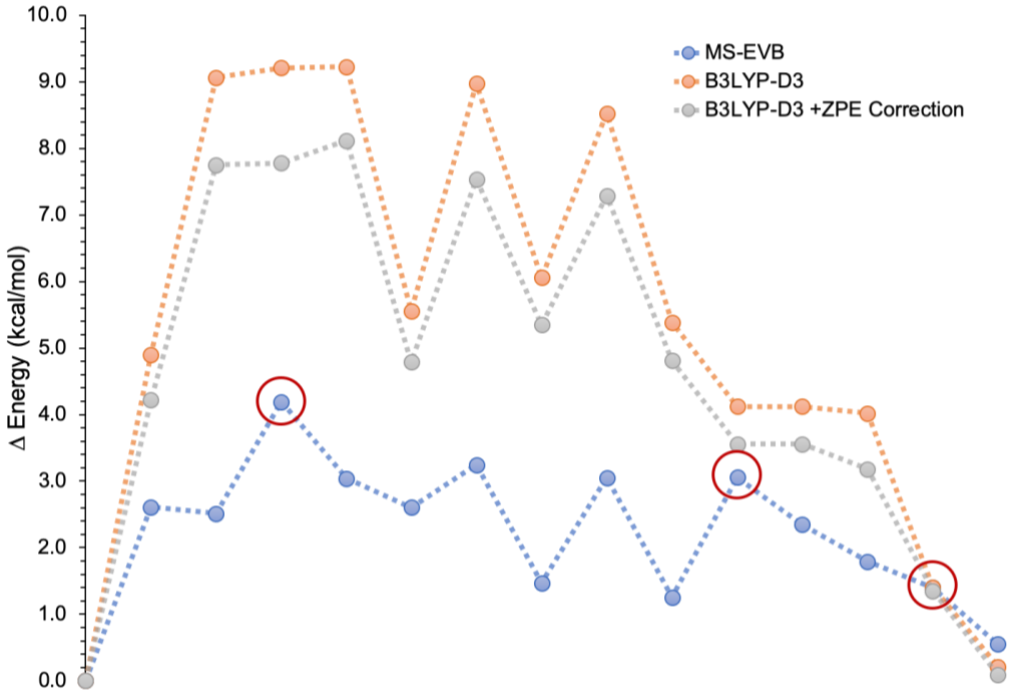

Figure 22: Comparison of minima at MS-EVB/TIP3P, B3LYP-D3 and B3LYP-D3+ZPE.

Figure 22, shows that the energetic ordering observed at MS-EVB/TIP3P level of theory (indicated by blue line) is not the same at B3LYP with D3 correction (B3LYP-D3) (indicated by the gray line) and B3LYP-D3 with vibrational zero-point energy correction (the orange line) calculated at the B3LYP-D3/6-31G(2d,p) level of theory. The red circles identify minima along an isomerization pathway on the MS-EVB potential energy surface that when re-optimized at

B3LYP-D3 level of theory (with or without ZPE correction) converge to a different isomer. When the indicated (red circles) isomers on the MS-EVB/TIP3P pathway are optimized at B3LYP-D3 level of theory, we find that the isomers differ by one rotated water molecule. The first red circle (in Figure 22) on the MS-EVB potential energy surface, which is 4.0 kcal/mol above Isomer 1 (Christie et al), is consistent with a $H^+(H_2O)_{21}$ isomer which has a surface Zundel cation. [229] This does not exist as a local minimum on the B3LYP-D3 potential energy surface. When considering the usefulness of the MS-EVB/TIP3P method as a viable model chemistry approach for mapping the potential energy surface of $H^+(H_2O)_{21}$, a minimum requirement is the qualitative reproduction of the potential energy surface. When energetic ordering of intermediate states is compared at MS-EVB/TIP3P and B3LYP-D3 levels of theory, no clear trend can be established. Also, minima on the MS-EVB/TIP3P potential energy surface are not guaranteed to exist on the B3LYP-D3 surface.

4.4 Conclusion

The MS-EVB/TIP3P method does not accurately describe the potential energy surface of $H^+(H_2O)_{21}$. Capturing both dispersion and polarization effects accurately is known to be important for characterizing the structures of water clusters. The underlying water model in the MS-EVB method is the flexible TIP3P empirical force field. TIP3P does not include explicit polarization. Therefore, incorporation in MS-EVB of a polarizable water force field parameterized against accurate ab initio calculation may offer a way forward for mapping the potential energy surface of $H^+(H_2O)_{21}$. Also, computational resources permitting, employing an ab initio method to describe the water monomers can provide more accurate results. MS-EVB is routinely employed to study

proteins and extended solids. This study serves as a cautionary tale that the accuracy of MS-EVB calculation is only as good as the empirical force field employed to describe the water-water and proton-water interaction.

Appendix A Structural and Electronic Properties of Ultrathin Picene Films on the Ag(100) Surface

This work[2] was previously published as: S. J. Kelly, D. C. Sorescu, J. Wang, K. A. Archer, K. D. Jordan, P. Maksymovch, Surface Science 652 (2016) 67–75. Kaye A. Archer carried out EOM calculations.

A.1 Introduction

Using scanning tunneling microscopy and electronic structure calculations, we investigated the assembly and electronic properties of picene molecules on the Ag(100), Ag(111), and Cu(111) surfaces, with particular emphasis on Ag(100). In each case, picene molecules are found to lie parallel to the surface at coverages up to half a monolayer and to adopt alternating parallel and tilted orientations at full monolayer coverage. In the latter case, the arrangement of the molecules is roughly similar to that in the bulk crystal. On the metal surfaces considered, the growth mode of picene is quite different from that of its structural isomer pentacene which forms a bilayer overlayer on top of a dense monolayer of flat-lying molecules on metal surfaces. Tunneling spectroscopy measurements provide estimates of the energies of several low-lying unfilled molecular orbitals as well as of the highest occupied molecular orbital of the absorbed picene

[2] SJK and JW carried out experiments, DFT and MD simulations calculations; KAA carried out EOM calculations; KDJ, DCS and PM guided theoretical, computational and experimental discussions.

molecules. From analysis of these results, we establish that the on-site Coulomb repulsion for picene decreases by ~ 2 eV in going from the gas phase to the full monolayer on Ag(100), bringing it close to that of the undoped bulk crystal.

Picene, an isomer of pentacene with an armchair arrangement of benzene rings, has attracted considerable interest for potential applications in electronic materials. Significantly, for the gas-phase molecules, the one-particle band gap is appreciably larger for picene than for pentacene (7.00 vs. 5.35 eV [230]) making it more stable (the band gaps of the corresponding crystals are 3.1 eV for picene and [231] 1.8 eV for pentacene [232]). In addition, it has been reported that the picene crystal, when intercalated with potassium, can become superconducting with a T_c below 7 K or even as high as 18 K [233,234], although this result has been questioned by other researchers.[235] Following the report of superconductivity in picene, several other PAHs (polycyclic aromatic hydrocarbons) with zig-zag fusion of the rings have been reported to become superconducting when doped with alkali or other metal atoms.[234] Equally intriguing is the nature of the electronic structure of the crystal at high doping levels but under conditions that it is not superconducting. [236]

At the same time, evidence is mounting that the doping picture itself is complex. Resistive measurements have revealed that picene undergoes a superconducting transition, [237] where the state above T_c is granular-metal-like. Other reports have suggested strong inhomogeneities in alkali-doped polyacenes. [238,239] This would be consistent with the inference of filamentary superconductivity where only a fraction of the total sample becomes superconducting. [240] Recent calorimetry measurements indicate that the reported superconductivity in alkali-doped picene may be due to ferromagnetic impurities, or that the molecules may even react with the intercalated K atoms. [238] In light of the inconsistencies concerning the nature of doped picene

films and crystals, it is clear that additional studies providing a molecular level under-standing of both the doped and undoped systems are required. Of particular importance for understanding the electronic structure of picene is the extent of electrostatic screening changes in going from the isolated molecule to condensed-phase systems.[236,241,242]

In this work, we present the first steps toward the development of such picture. Using tunneling microscopy and spectroscopy as well as electronic structure calculations, the monolayer structures of picene on Ag(111), Cu(111), and Ag(100) were characterized. As reported earlier by the Hasegawa group, [243] picene on Ag(111) displays two distinct phases in which all adsorbed molecules are in direct contact with the metal surface. We determined that this behavior also occurs for picene on the Ag(100) and Cu(100) surfaces. Furthermore, for picene/ Ag(100) we determined using tunneling spectroscopy the energies of cation states associated with the highest occupied molecular orbital (HOMO), and the anion states associated with the lowest unoccupied molecular orbital (LUMO) and several higher energy unoccupied orbitals. In a simple orbital model, the HOMO–LUMO gap of a molecule depends linearly on U, the on-site Coulomb repulsion. [244] In condensed phase systems, the U value is reduced by screening effects. We deter-mined that the value of U for picene molecule on the metal surface is comparable to that of picene in the bulk crystal. Our first attempt toward intercalation of K atoms into the picene film, aiming to reduce the nearly neutral adsorbed molecule to an open-shell anion state, introduced very strong disorder into the picene layer, although the procedure used is known to produce well-ordered structures of doped C_{60}.[245]

A.2 Experimental and Computational Methods

A.2.1 Experimental

Picene films were grown in a custom-modified UHV chamber equipped with a deposition source, LEED and a quartz-crystal microbalance. Metal surfaces were cleaned by sputtering/annealing cycles prior to molecular deposition. The molecules were deposited on the metal surfaces at temperatures between 77 and 150 K. Subsequent ordering of the films was achieved by post-annealing to T = 300 K. STM images were acquired and tunneling measurements were carried out with a commercial scanning tunneling microscope (SPECS JT-STM) at T = 77 and 4.5 K. Tunneling spectroscopy was used to determine the HOMO–LUMO gap as well as the energies of higher-lying anion states of picene on Ag(100).

A.2.2 Computational Methods

The adsorption properties of picene molecules on the Ag(100) sur-face as a function of coverage were investigated using density functional theory calculations carried out with the Quickstep module [246] of the CP2K program. [247] The calculations made use of the PBE functional [67] with the Grimme-D3 [63] correction for long-range dispersion. The DZVP-MOLOPT [248] Gaussian-type orbital (GTO) basis set was used for the Ag atoms, and the TZV2P-MOLOPT GTO basis set was used for the C and H atoms of the picene molecule Goedecker, Teter and Hutter (GTH) pseudopotentials [127] were used to represent the core electrons. A plane-wave basis set with a cutoff of 400 Ry was used for expansion of the electronic density.

The binding configurations of the picene molecule at different cover-ages were investigated using two sets of slab models. The first set of models which included the (4 × 4), (6 × 6) and (8 × 8) square surface models with their axes aligned parallel and perpendicular to the [0, 0.5, −0.5] axis was used to characterize the adsorption of picene on the sur-face at low coverage. The second set used (7 × 5) and (8 × 5) rectangular supercells with their axes oriented along the [0,1,0] and [0,0,1] directions. This set of supercells allowed the analysis of adsorbed picene molecules at higher coverage, including arrangements having a surface packing and orientation similar to that observed experimentally. In all instances the slabs used in calculations contained five Ag layers, with the top two layers of metal atoms being allowed to relax, and the bottom three layers being kept frozen at their bulk optimized positions. A vacuum region of 26 Å was employed in the direction perpendicular to the surface.

To aid in the analysis of the features observed in the tunneling measurements, we have also carried out calculations of the anion states using the electron-affinity equation-of-motion MP2(EA–EOM–MP2) method [249] as implemented in the CFOUR code [170] and in conjunction with the cc-pVDZ Gaussian-type orbital basis set.[250] This basis set was chosen to prevent collapse of the anion states onto the continuum. [251] In addition, we also report electron affinities estimated from experimental ionization potentials [252] and from application of the pairing theorem.[253] According to the pairing theorem, the energies of π and π^* orbitals of alternant hydrocarbons are symmetrically located about a reference energy.

A.3 Results and Discussion

A.3.1 STM Results

At sub-monolayer coverage (Figure 23 a), the constant current STM image of a picene molecule on Ag(100) has a characteristic crescent shape due to the zig-zag arrangement of the benzene rings in the molecular backbone. The apparent approximate size of the molecule is ~1.35 nm long and ~ 0.7 nm wide. The long-axis of the molecule is oriented along the <010> direction of the Ag(100) surface. At low coverage, the molecules are isolated consistent with repulsive intermolecular interactions. These are likely to be dominated by H–H repulsion but could also include dipolar repulsive interactions [254] due to small charge transfer between the surface and the molecules and Pauli repulsion. [255]

Upon increasing the surface coverage to about 0.5 ML (region 1 in Figure 23 b and Figure 24 d), the picene molecules are seen to adopt a partially ordered arrangement with the molecular axes twisted slightly off the original 45° orientation, and with the molecules stacked along the short axes. We refer to this structure as phase 1. The intermolecular spacing along the rows is ~0.7–0.8 nm, while that across the rows is ~1.5 nm. The ordering is not regular, as evidenced by meandering of the molecular displacements along the close-packed rows. Further increase of the coverage completes the monolayer (region 2 in Figure 23 b and d). In contrast to the low coverage where the molecules repel one another (e.g. Figure 23 a), a new phase, denoted phase 2, nucleates within phase 1 and grows as islands (Figure 41). Moreover, as will be seen from the calculations discussed below, about half the molecules in phase 2 are tilted with respect to the surface and bonded to it via one of their edges. As will be discussed later the net intermolecular interactions when in-creasing the coverage to 1.0 ML are attractive, in contrast to those at or below 0.5 ML.

The STM images of the full monolayer, display an alternating pattern along the rows (Figure 23 d), implying that the unit cell is comprised of two inequivalent molecules. There is also a subtle modulation of the intermolecular spacing, which doubles the size of the unit cell, with the net dimensions being v = 3 nm and u = 1.1 nm (Figure 23 d). Despite being more highly ordered than the phase 1 structure in which the molecules are bound parallel to the surface (Figure 23 b and d, as well as Figure 24 d), the tilted molecules in the phase 2 structure display small, random deviations from translational periodicity that are apparent in high-resolution images (Figure 23 d).

At still higher coverage, after saturation of phase 2, growth proceeds into the multilayer regime, where locally saturated 3D islands of two or more layers of picene molecules grow on top of the monolayer (Figure 23 c). Therefore, on the Ag(100) surface, phase 2 is the most ordered arrangement of molecules, while growth itself proceeds in the Stranski– Krastanov mode [157] where formation of the second layer precedes growth of a three-dimensional film.

The growth mode of picene molecules is qualitatively similar on Cu(100) as seen in Figure 24 . The largely disordered layer of flat-lying molecules (region 1 in Figure 24 a) begins to develop into more highly ordered islands (region 2 in Figure 24 a). For the Ag(111) surface, the coexistence of two types of structures is also observed [243], although the lower coverage phase 1 structure is more highly ordered than phase 2. The electronic properties of the resulting surface structures were probed using scanning tunneling spectroscopy. To eliminate the current-induced damage of the adsorbed layers, we have used the technique of Z–V spectroscopy [256], in which the tunneling current is kept constant during the voltage ramp. When the tunneling energy matches the energy of a molecular resonance (i.e., the energy of an occupied or unfilled orbital), the tip retracts to maintain overall a constant tunneling probability. The energies of the electronic states are therefore registered as steps in the height Z of the STM tip relative to the metal surface or as peaks in dZ/dV.

As seen in Figure 25 a, for the phase 1 structure of picene on Ag(100), broad resonances due to anion formation are registered at 1.3, 2.1, and 3.3 eV. There is also a sharp peak at 3.5 eV that we attribute to the image potential state of the metal surface. Figure 25 b shows the corresponding results for the phase 2 (monolayer) system.

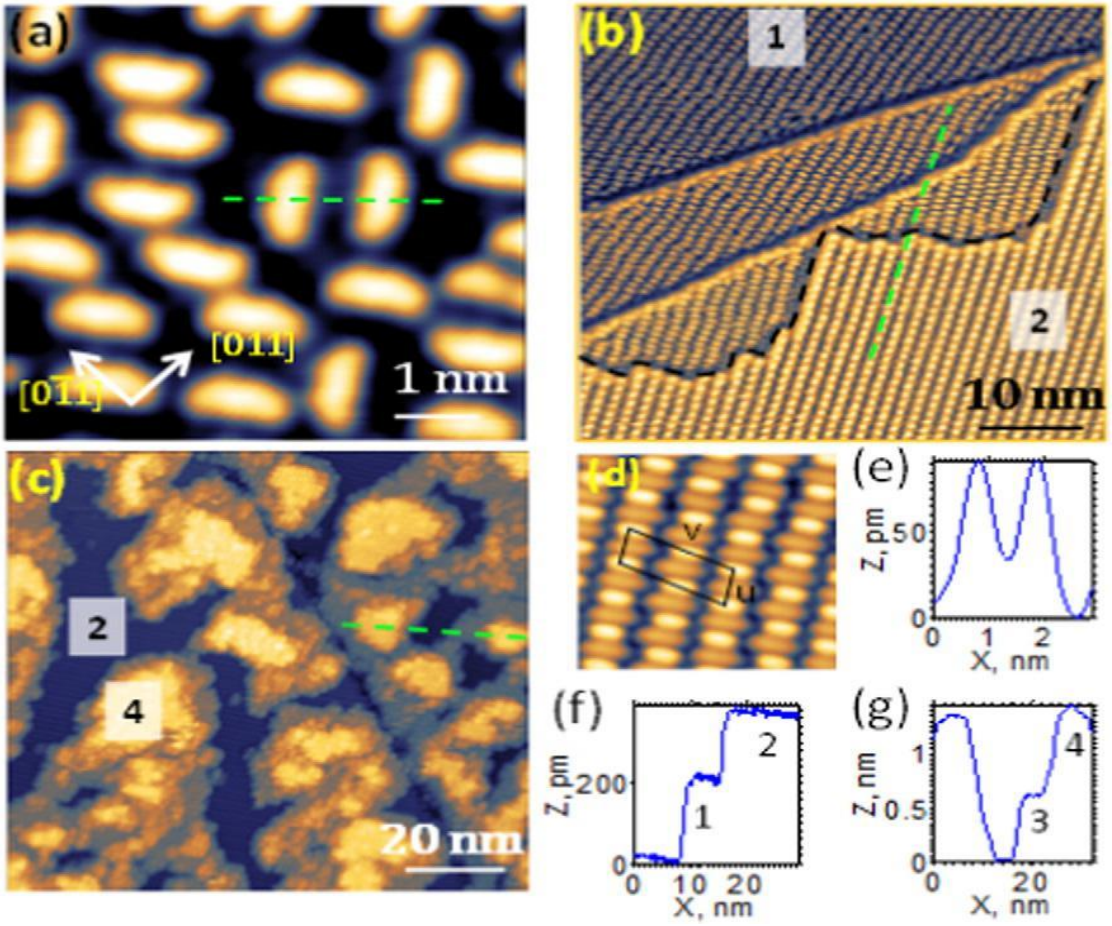

Figure 23: Constant current STM images of picene molecules on the Ag(100) surface: (a) at low coverage (acquired at bias V = 1 V and current setpoint I = 30 pA); (b) at higher coverage where both phase 1 (region 1) and phase 2 (region 2) coexist (U = 0.7 V, I = 140 pA); (c) at still higher coverage where the phase 2 structure is fully saturated (region 2) and multilayer islands up to nominally three layers begin to nucleate (U = 3.2 V, I = 100 pA). (d) A close-up STM image of the phase 2 system, with unit-cell vectors *u* and *v* described in the text (U = 0.7 V, I = 140 pA). (e–f) Topographic line profiles along green dashed lines in images (a–c), correspondingly. Numbers in the images and line-profiles correspond to the nominal thickness of the layers.

The resonances in phase 2 structure are notably narrower than those in the phase 1 structure, most likely due to reduced electronic coupling of the tilted molecules in phase 2 to the surface. Moreover, each of the first two peaks appears to be comprised of two closely spaced features as seen in Figure 25 c and d. Using Lorentzian fits (Figure 25 d), the energies of these features are estimated to be 1.55 and 1.69 eV and 2.23 and 2.35 eV. As with the phase 1 structure, the phase 2 structure displays a sharp resonance centered at 3.5 eV (Figure 25 b) associated with the image potential state. In addition, a filled state resonance is observed at is observed at ~−1.37 eV (Figure 25 e).

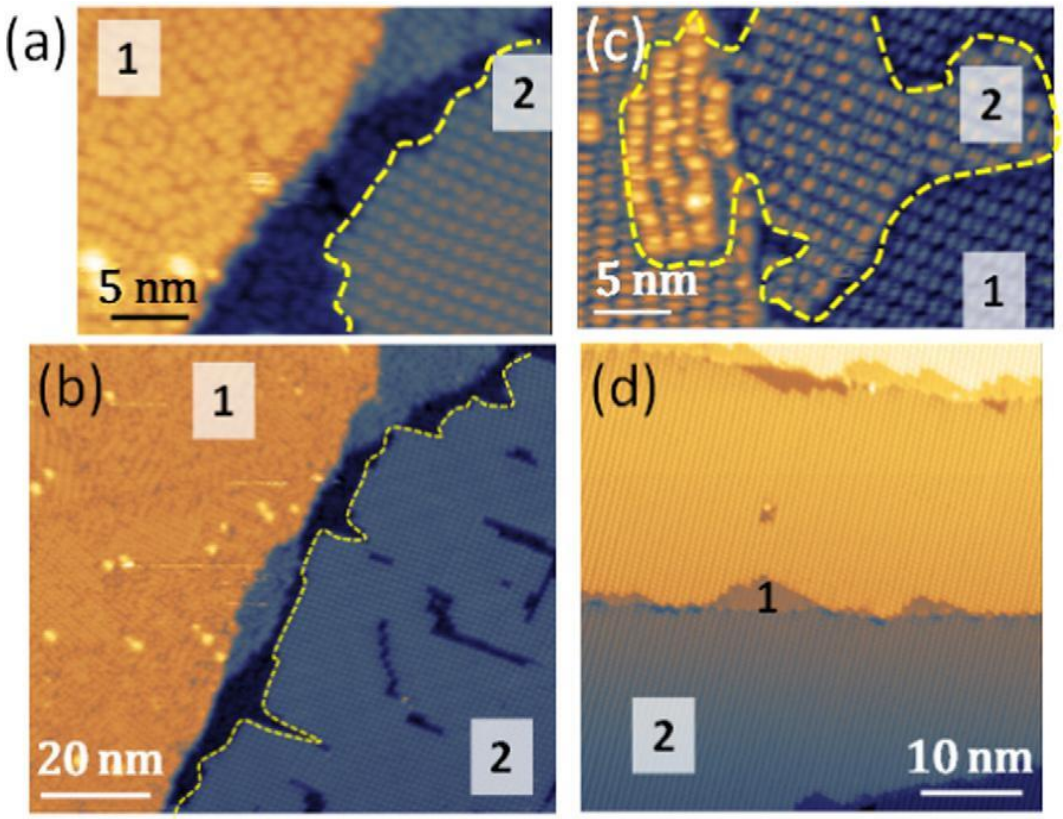

Figure 24: Constant current STM images of coexisting phases 1 and 2 on Cu(100) surface (a, b) (U = 0.3 V, I = 30 pA), Ag(111) surface (c) (U = 1.2 V, I = 20 pA), and Ag(100) surface (d) (U = 0.5 V, I = 30 pA). The phase 1 and phase 2 regions are marked in each case.

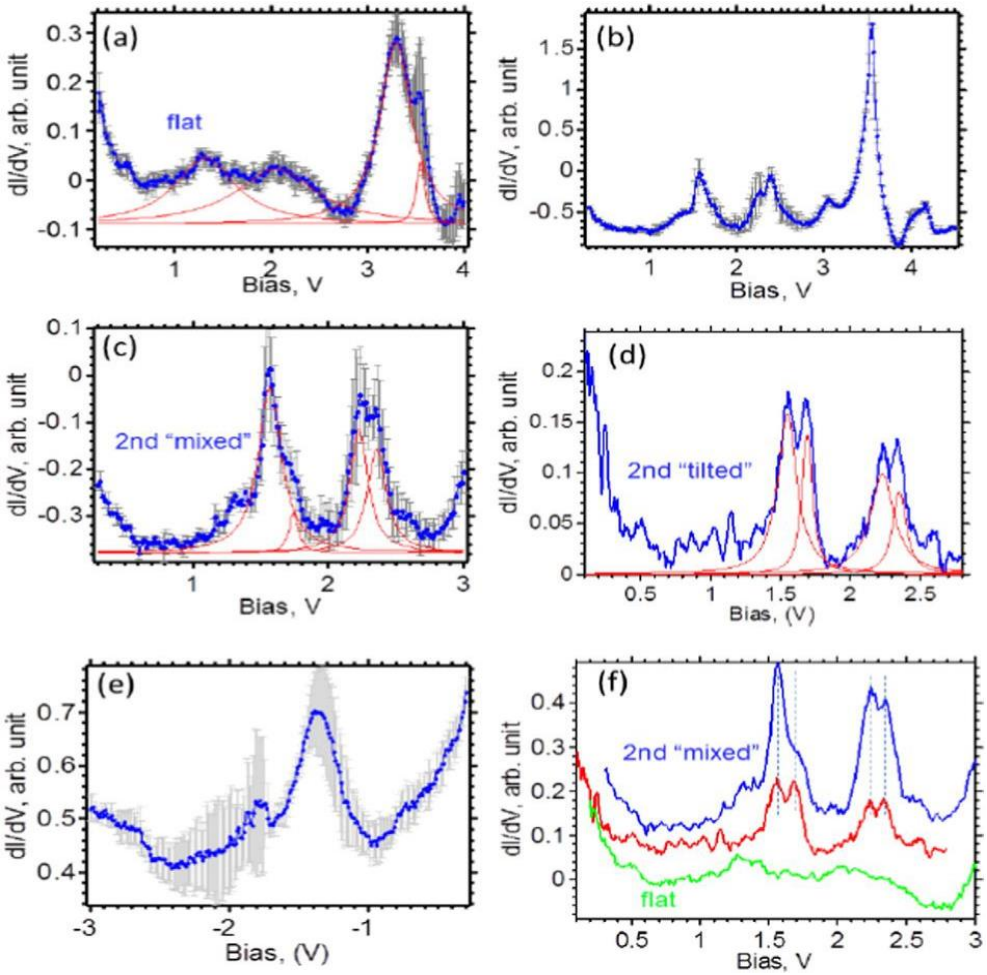

Figure 25: Tunneling spectroscopy of empty electronic orbitals of picene on Ag(100). Blue is the average of several (2–20) individual I–V curves; gray is the error bar corresponding to one standard deviation; red is the fit to the observed peaks using a Lorentzian function. (a) Phase 1; (b) phase 2. (c) Mixed phase 1 and phase 2, (d) low-energy anions states of phase 2 picene/Ag(100) with observable fine structures within each of the first two main peaks and the accompanying fit with four Lorentzians. (e) Filled state region of the phase 2 picene on Ag(100). (f) Overlay of three kinds of spectra in (a), (c) and (d) that reveals their relationship to each other. All spectra were acquired at 77 K using Z–V spectroscopic mode with a constant-current set-point of ~ 100 pA. Note that the spectra show *dI/dV*, acquired as the first harmonic of voltage-modulated tunneling current with the AC amplitude of 5–10 mV and frequency of 650 Hz.

A.3.2 Experimental Analysis of Picene Epilayers

As was previously concluded for picene on Ag(111) [243], the phase 1 structure should not be viewed as a complete monolayer because all molecules in the saturated phase 2 are in direct contact with the metal surface. This is not obvious upon visual inspection of the STM images in Figure 23 and Figure 24 where the molecules adsorbed in going from the phase 1 structure to the phase 2 structure appear to have grown on top of the molecules adsorbed flat on the surface (e.g. Figure 24 d). However, both the apparent height measurements and the calculations discussed below support a phase 2 structure with about half of the molecules being tilted with respect to the surface and bound to it edge wise. The STM measurements give an apparent height of ~ 100 pm (Figure 23 e) for the picene molecules relative to Ag(100) in phase 1, and a change in the apparent height of ~ 170 pm between phase 1 and phase 2 (Figure 23 f). The height difference between the top of the phase 2 and the second layer is ~600 pm and that between the second and third layers is 600–700 pm (Figure 23 g). The experimental measurements yield contours of constant tunneling probability rather than the topography. The positions of molecular resonances in the tunneling spectra (discussed below) do not significantly depend on tip–sample distance, which implies that the potential drops primarily across the vacuum gap, which is consistent with a wide gap (low tunneling current) and a dielectric constant of 3–4ε0 characteristic of organic semiconductors. Therefore, the apparent height difference of 170 pm in going from phase 1 to phase 2 is expected to be quite close to the topographic height difference, even though the height of the molecules comprising phase 1 is clearly underestimated by STM topography. The smallest unit-cell dimension of bulk picene is 615.4 pm, which is comparable to the separations between the layers after the first full monolayer, but far greater than the 170 pm height difference between the phase 1 and phase 2 structures.

A.3.3 Structural Analysis from the DFT Calculations

Phase 1

In the computational studies, we first examined the adsorption con-figurations of picene molecules on the Ag(100) surface at low surface coverage. This was accomplished by placing a single picene molecule in the (4 × 4), (6 × 6) and (8 × 8) supercells with the long axis of the molecule taken parallel to the Ag–Ag close contacts. The results of this analysis are summarized in Figure 26. At low coverage, corresponding to a single picene in the (8 × 8) surface unit (Figure 26 a), the molecule adsorbs flat on the surface and can assume three different orientations. In one (denoted α), the molecular axis is parallel to the [0, 0.5, −0.5] axis of the Ag(100) surface, and in another (denoted δ), it is diagonally oriented along the [0,1,0] axis. The third orientation (denoted γ) corresponds to an intermediate structure with the axis rotated by about 18° relative to that defined by the Ag–Ag short distance. For each of these three orientations, we investigated structures with the molecular center initially located above fcc, hollow, or top sites. Panel a) in Figure 26 indicates the evolution from the initial structures to the optimized structures. For the α and δ configurations, adsorption at both the fcc and hollow sites is found to lead to stable minima, while for the γ configuration only a single stable structure located above the hollow site was determined. The adsorption energy is calculated to be relatively insensitive to the orientation of the molecule on the surface. As a result, at low coverages the adsorbed picene molecules should readily rotate and diffuse on the Ag(100) surface. Regardless of their positions or orientations, at low coverage the picene molecules are predicted to lie nearly flat on the surface. This is illustrated for δ(fcc) in the inset panel in Figure 26 a), which provides a side view of the adsorption structure. As seen in this panel, the picene molecule lies flat on the surface at a distance of about 3.0 Å above the metal atoms in the top layer.

The variations with increasing coverage of the calculated adsorption energies for the most stable α and δ configurations of a picene molecule on the Ag(100) surface are reported in Figure 26 b). The results were obtain-ed from calculations performed using the (8 × 8), (6 × 6) and (4 × 4) supercells.

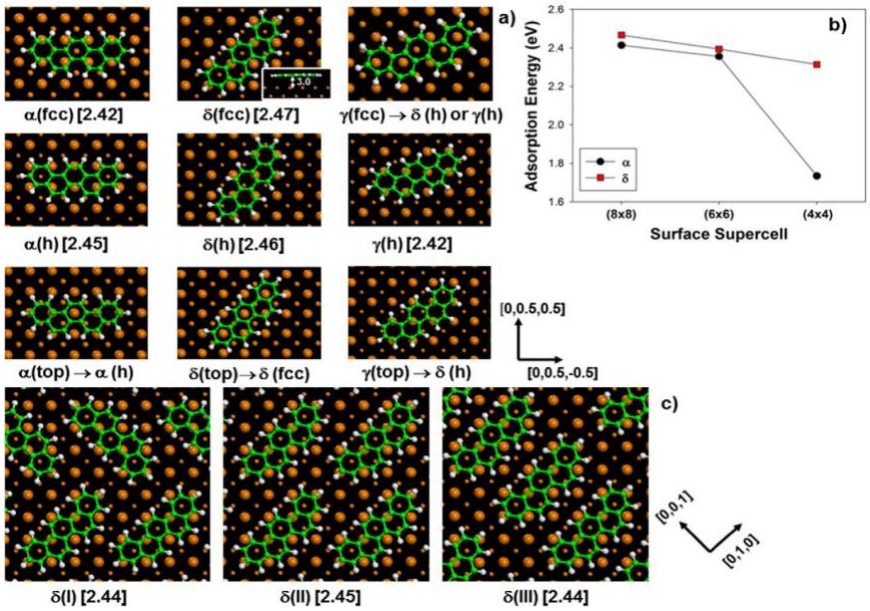

Figure 26: Adsorption configurations of picene on Ag(100) in the dilute to phase 1 regime as determined by DFT calculations. In all these cases the molecules are lying flat on the surface. For the stable adsorption configurations, the binding energies in eV of the final optimized structures (shown in the figures) are given in parentheses. For unstable configurations the evolution of the depicted structure from the initial (shown in the figure) to final structures is indicated. Configurations in panels a) correspond to a single molecule adsorbed in the (8x8) unit cell. α, δ and γ labels denote configurations parallel to the [0, 0.5, -0.5] axis, diagonally oriented along the [0,1,0] axis and rotated by about 18˚ relative to [0, 0.5, -0.5] axis, respectively. The fcc, hollow (h) and top labels used refer to the specific locations on the surface of the middle of picene molecule. The α, δ and γ arrangements are defined in the text. Panel b) indicates the variation of the adsorption energy of configurations α and δ for different surface supercell models. Panel c) illustrates different arrangements of molecules in the δ state at 0.5 ML coverage with the long axis of neighbor molecules oriented either perpendicular (δ(I)) or parallel ((δ(II) and δ(III)) to one another.

The calculated adsorption energies decrease with increasing coverage, although for the δ configuration the decrease is relatively moderate, going from 2.47 eV for the (8 × 8) supercell to 2.31 eV for the (4 × 4) supercell. For the α configuration the adsorption energy drops precipitously, particularly when going from the (6 × 6) to the (4 × 4) supercell. Due to the increase of the lateral repulsion between H atoms on different molecules, the α configuration becomes highly destabilized at higher coverages. These calculations demonstrate that as 0.5 ML coverage is approached, only the δ adsorption configuration, in which the molecule is oriented "diagonal" along the [0,1,0] direction, would be expected to survive. This result is consistent with the experimental observation for the preferred orientation of picene molecules up to 0.5 ML coverage (Figure 23 a). For the δ configuration, we considered structures with the long axes of neighboring molecules oriented either perpendicular (δ(I) in Figure 26 c)) or parallel (δ(II) and δ(III) in Figure 26 c)) to one another. Essentially the same binding energy is obtained for these arrangements at this coverage. We also examined the sensitivity of the adsorption configuration and binding energy of picene molecules to the surface as the lateral separation between the molecules is decreased. This was done using the 8 × 5 and 7 × 5 surface supercells (see Figure 27 a) and b)) oriented along the [0,1,0] and [0,0,1] directions, respectively, and containing two rows of molecules. The separation between the centers of the rows is 16.4 Å for the 8 × 5 supercell and 14.4 Å for the 7 × 5 supercell. As seen from the side views of the resulting configurations depicted in panels a) and b) of Figure 27 the molecules at these coverages remain flat on the surface and have comparable binding energies of 2.49 and 2.46 eV.

Phase 2

We examined next the adsorption of picene molecule at coverages greater than 0.5 ML. This has been done for the case of the (7 × 5) supercell by increasing the number of molecules in

each row from two to three (see panels c) and d) in Figure 27). As shown in these figures, upon optimization, the structure changes from one with all molecules lying flat on the surface to structures in which either about a third of all molecules are tilted (see Figure 27 c) or all of them are tilted by some degree (see Figure 25 d) with respect to the surface. These two arrangements are essentially isoenergetic with adsorption energies of about 1.9 eV/ molecule, significantly smaller than that (2.5 eV/molecule) for phase 1. These findings suggest that a simple increase in the number of molecules in the first layer from two to three for each row in the (7 × 5) supercell (see Figure 27 c and d) is highly unfavorable and these higher coverage arrangements were not considered further.

Additionally, we analyzed whether picene molecules could adsorb lying flat on top of the molecules already adsorbed flat on the surface. This has been done for the case of the (7 × 5) supercell containing a total of twelve molecules distributed equally in two rows (each containing two layers). Calculations reveal (for a typical case see Figure 42) that such arrangements are unstable with respect to those in which some of the molecules are tilted and some are bonded edgewise to the sur-face. For this reason, in the ensuing discussion we focus on structures in which some molecules are bonded directly to the metal surface but are tilted with respect to the surface.

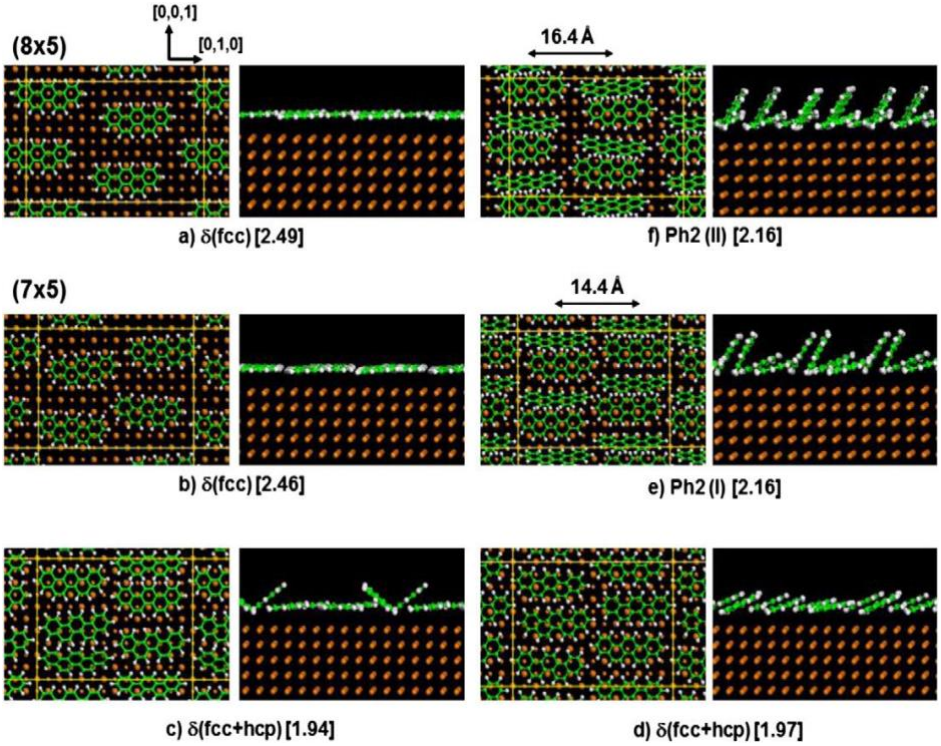

Figure 27: Adsorption configurations of picene in phase 1 on Ag(100) at 0.5 ML (panels a) and b)), at intermediate coverages above 0.5 ML (panels c) and d)) and in phase 2 at full ML coverage (panels e) and f)) as determined by DFT calculations. The number of picene molecules per supercell is four (a), b)), six (c), d)), and eight (e), f)). The supercells used in calculations are indicated in the figures. The acronyms Ph2(I) and Ph2(II) refer to molecular configurations of picene in phase 2 in the (7 × 5) and (8 × 5) supercells, respectively. The other acronyms are explained in the main text.

The most stable arrangement for phase 2 has all the molecules be-yond 0.5 ML tilted with respect to the monolayer and located in between the molecules of the first layer, as shown in panels e) and f) of Figure 27. The average binding energy of all molecules, both flat and tilted, is 2.16 eV, for both the 7 × 5 and 8 × 5 supercells. The most tilted molecules are less strongly adsorbed than the nearly flat-lying molecules, with binding energies of 1.86 and 1.84 eV for 7 × 5 and 8 × 5 supercells, respectively. However, we note that these adsorption energies are higher than the cohesive energy between picene molecules in the crystal. For picene crystal with a monoclinic

structure [257], we calculate a cohesive energy of 1.76 eV per molecule (for the optimized crystal, our calculated lattice parameters of 8.449, 6.112, and 13.454 Å agree to within 1.5%, with the experimental values of 8.480, 6.154, and 13.515 Å [257]).

Calculations carried out with only the tilted molecules on the surface, give a binding energy of about 1.2 eV/molecule, which leads us to conclude that for the phase 2 structure, about 0.9 eV of the binding energy per molecule of the tilted molecules comes from interactions with the molecules bound flat (or nearly so) on the surface. This molecule–molecule interaction is expected to be dominated by dispersion and electrostatic contributions. While our calculations indicate that the average binding energy per molecule is reduced in going from phase 1 to phase 2, Hasegawa and co-workers [258], reached the opposite conclusion concerning the relative stabilities of the two phases on Ag(111). In this case, however, phase 2 would precede the formation of phase 1, which is not the case as seen from the results of our experiments.

Overall, the results presented in Figure 27 and Figure 42 provide strong support that phase 2 is a mixture of molecules lying nearly flat on the surface and molecules that are tilted with respect to the surface plane, in agreement with the experimental findings. The most notable conclusion is that the intermolecular interactions contribute as much as 0.9 eV/molecule to the binding, allowing the titled configuration to be energetically preferred over a hypothetical flat lying bilayer.

Analysis of Tunneling Spectroscopy Measurements

We now turn to the analysis of the tunneling spectra of the phase 2 structure (shown in Figure 25 b–f). Table 5 summarizes the energies of the anion states of picene (referenced relative to the ground state anion) obtained from EA-EOM-MP2 [249] calculations using the cc-pVDZ basis set, from use of the pairing theorem [253] and from experiment, together with our assignments. The calculated results are for the gas-phase molecule while the experimental results

are from the present measures of picene monolayer on Ag(100).

For phase 2 picene/Ag(100) the relative energies of molecular resonances are 0.14, 0.67, 0.79, 1.43 eV, and 2.55 eV (based on Figure 25). Comparison of the EOM and experimental results leads to the following assignment of the experimentally observed features: The first broad resonance (overlapping features at 0 and 0.14 eV) derives from the ground and first excited anions states, which are predicted to be nearly degenerate, the second broad resonance (overlapping features at 0.67 and 0.79 eV), is due to the third anion state, and the 1.43 and 2.55 eV features to the fourth and sixth anion states, respectively. The calculations place the fifth anion state 1.80 eV above the ground state, and although the experiment does not display a clear feature at this energy, it could be hidden under the low-energy shoulder of the image potential state. Finally, the predictions of the pairing theorem are close to those of the EOM calculations, providing further support for these assignments.

The major issue with the above assignment concerns the (0.67, 0.79 eV) doublet observed experimentally, while the calculations predict only a single anion state in this energy range. We believe that it is unlikely that the experimentally observed splitting derives from picene molecules in different environments. A more likely possibility is that the splitting results from the interactions between picene molecules. If this is the case, then the lower energy doublet (0 and 0.14 eV) could also have as its origin the splitting caused by interactions between picene molecules.

Overall good agreement is found between the computed relative energies of the anion states for the gas-phase molecule and the corresponding STS results for the phase 2 system. This indicates that there is an approximately uniform shift in the energies of the various π^* anion states of picene in going from the gas-phase molecule to the phase 2 adsorbed species. The anion states

of the phase 1 structure are stabilized by additional 200–300 meV compared to titled molecules in the phase 2 structure, presumably due to the stronger interaction with the metal surface.

Assuming that the broad peak at ~−1.3 eV in the STS measurements (Figure 25 e) corresponds to electron ejection from the HOMO, the HOMO– LUMO gap for picene molecules in the phase 2 structure is then 2.9 eV,

Table 5: Relative energies (eV) of the π* anion states of picene.

STS of phase 2 picene/Ag(100)	Gas-phase picene	
	EOM-MP2	Pairing theorem[c]
0.0, 0.14[a]	0.0, 0.04	0.0, 0.13
0.67, 0.79[a]	0.66	0.82
1.43	1.30	1.52
(1.80)[b]	1.80	1.74
2.55	2.41	1.74

[a] The doublet structures in the STS features were determined by a fitting procedure de-scribed in the text.

[b] Although the STS measurements do not display a distinct feature near 1.80 eV, such a feature could be "hidden" on the low-energy side of the intense feature associated with the image potential state.

[c] These results are derived from the experimental IPs of picene reported in [252].

while the experimental IP–EA value for the gas-phase molecule is 7.0 eV. The 4 eV reduction in the HOMO–LUMO gap in going from the gas-phase molecule to the phase 2 structure, implies that the on-site Coulomb potential is reduced by about 2.0 eV due to screening by the neighboring molecules and the metal surface.

A similar conclusion is reached by estimating the extent of the screening from the shift in the LUMO in going from the gas phase molecule to the phase 2 structure. The first EA of picene in the gas phase is 0.6 eV (referenced to vacuum) [230] while the energy of the first anion state of the phase 2 structure of picene on Ag(100) is 1.55 eV relative to the Femi level. Since the work function of Ag(100) is ~4 eV, we conclude that the anion state is stabilized by 1.8 eV in going from the gas-phase molecule to the phase 2 structure. Thus, the reduction in the U value due to screening deduced from the shift of the LUMO level is consistent with that determined from the change in the HOMO–LUMO gap. The work-function of 4 eV was estimated from the position of the image potential state (3.5 eV), the binding energy of which is ~ 0.5 eV below vacuum level on Ag(100).[259]

Interestingly, the band-gap of a crystalline picene is ~3.3 eV close to that determined here for phase 2 picene/Ag(100), which indicates that the screening due to the metal substrate and surrounding molecules in adsorbed picene is comparable to that in the picene crystal. This immediately suggests that despite close-proximity to the metal surface, Coulomb screening in polyaromatic molecular systems remains weak. Even for an electronic bandwidth (W) of ~ 0.5 eV, U_{scr}/W N 1, making the emergence of Mott-insulating state quite likely in doped picene. In prior studies, the Coulomb repulsion has been assumed to be ~1–2 eV in picene [236], but the models show a metal–insulator transition around a value of the Coulomb repulsion of 0.8 eV. [260] At the same time, the regime analyzed in Ref. [241], here there is suppression of the Mott insulating state and formation of ¾ filled bands in 3e-doped picene, necessitates U values of N5 eV. The screening in either bulk or adsorbed forms is too strong to allow such cross-over between ½ filled and two ¾ filled bands, at least within the assumed approximations. This situation may be different

however, in a condensed phase adsorbed on insulators, where there would be no effects of image screening due to proximity to metallic substrate.

We now examine more closely the resonance structure in the STS measurements of picene on Ag(100) under different coverages. Figure 25 (a) reports the spectrum for the phase 1 structure which corresponds to flat-lying molecules. Figure 25 b and d report the spectra for the phase 2 structure, and Figure 25 c reports the spectrum due to a mixture of phase 1 and phase 2 structures. Figure 25 f demonstrates how the spectrum in Figure 25 c arises as a superposition of those from phase 1 and phase 2 structures. However, as we discussed above, the detailed origin of splitting in Figure 25 d (and its effect on spectra in Figure 25 c) will need further investigation, as the magnitude of the splitting of the peaks at ~ 1.5 eV is too large to be explained by the near-degeneracy of LUMO/LUMO + 1 states, while the splitting of the peaks at ~ 2.25 eV is too small to be accounted for by LUMO + 2/LUMO + 3 splitting.

Picene Epilayer Doped with Potassium

Much of the controversy regarding K-doped picene and related polyaromatic hydrocarbons [261,262] has to do with the absence of well-defined single crystals and instability of such materials in ambient environment, which significantly hinder electron transport measurements on any kind of alkali doped material. Thin films would be very beneficial in this regard as would be the prospect of direct characterization of K-doping, or even the hypothesized superconducting state, with tunneling spectroscopy. To this end, we attempted to dope the well-characterized films with potassium. To avoid deposition of hot K atoms directly onto the molecular film, we first deposited K onto Ag(100) and then over-grew picene. K would not diffuse into the bulk of the Ag crystal under these conditions. We further confirmed that the work-function of the surface is lowered by at least 2 eV by K deposition .[263]

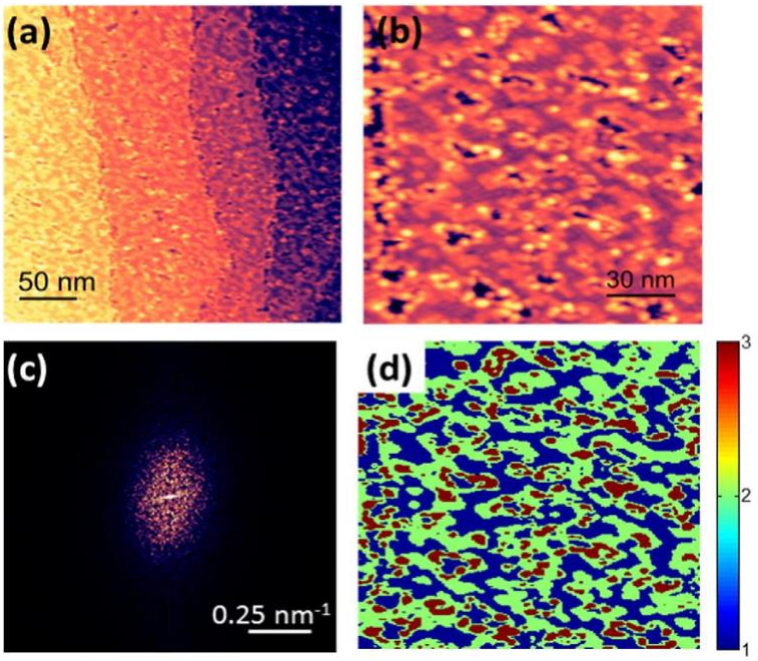

Figure 28: STM images of picene grown on top of a K-doped Ag(111) surface. (a, b) Large and small-scale constant-current topography images of typical structures. (c) 2D-FFT of the image in (b) that shows lack of apparent long-range order. (d) k-means cluster transform applied to (b). Here the constant-current heights from the STM image are partitioned into three clusters using the k-means++ clustering algorithm.[264] **The colors in the image correspond to the cluster number. There are three characteristic features in this image. These are: the flat-lying picene molecules in cluster 1 (possibly phase 1), and slightly higher molecules in cluster 2 (possibly tilted as in phase 1) and the bare surface in cluster 3.**

As clearly seen in Figure 28 a and b, the quality of the films that form on K-doped Ag(100) is far inferior to that observed on the clean metal surface. In particular, there is an almost complete lack of long-range ordering as evidenced by the Fourier transform of the STM image (Figure 28 c). STM topography reveals multiple holes on the surface, which based on the constant current topography represent single molecular layers (Figure 28 d). The other characteristic feature is that the molecules sur-rounding the holes have slightly higher apparent topography (Figure 28 d). The cause of the observed disorder is not clear. However, one possibility would be the strong

electrostatic interactions involving negatively charged picene molecules and K^+ ions. We could also be observing a chemical reaction between potassium and picene as suggested by the calorimetry study of Ref. [238]

A.4 Conclusions

In conclusion, picene is shown to be able to form two types of structures on noble metal surfaces. In the lower coverage phase, denoted phase 1, the molecules lie flat on the surface, and in the higher coverage phase, denoted phase 2, half of the molecules lie nearly flat on the surface and the other half lie tilted about 30° with respect to the plane of the surface plane. Our calculations show that a significant portion of the stability of phase 2 comes from attractive interactions between the tilted and flat lying molecules. Scanning tunneling microscopy measurements show that the HOMO–LUMO gap is reduced from 7 eV to about 3 eV for phase 2 picene on Ag(100), with the latter value being close to that of the bulk crystal. The sizable reduction in the on-site Coulomb repulsion upon formation of the monolayer makes it an interesting molecular model system for strongly correlated electronic ground states produced upon doping. Finally, we attempted to carry out K-doping of the picene monolayer and found that in the coverage regime tested, K-doping caused significant disorder, most likely caused by electrostatic interactions. We believe that scanning probe microscopy with molecular resolution may provide critical insight into the structure, chemistry and electronic states of the potassium doped polyaromatic hydrocarbons, particularly if bulk-like arrangements of molecules can be stabilized in ultrathin structures. Here, we showed that even a monolayer of picene on certain metal surfaces may satisfy this criterion and approach bulk-like “herringbone” arrangement of molecules as well as electrostatic screening

comparable to bulk values. Further effort combining tunneling spectroscopy and epitaxially grown films is likely to produce deeper insight into doping of polyaromatic hydrocarbons, with direct implications for their presumed phase-transitions.

A.5 Acknowledgments

SK, JW, PM: Experiments were carried out at the Center for Nanophase Materials Sciences, sponsored at the Oak Ridge National Laboratory, by the Division of User Facilities, Basic Energy Sciences, U.S. Department of Energy. KDJ and KA acknowledge support from the National Science Foundation through grant CHE-1362334. Some of the calculations were carried out at the University of Pittsburgh's Center for Simulation and Modeling.

Appendix B Supplementary Materials

B.1 Supplementary Materials for "Water Network-Mediated, Electron Induced Proton Transfer in Anionic $[C_5H_5N\cdot(H_2O)_n]^-$ Clusters"

B.1.1 Photoelectron Spectra of $[Py\cdot(H_2O)n]^-$, n=3–5 Clusters

Photoelectron spectra of $[Py\cdot(H_2O)_n]^-$ clusters for n = 3-5 are presented in Figure 29. These were obtained by velocity map imaging with an excitation wavelength of 532 nm. Trace (a) compares the spectra of the bare (black) and Ar-tagged (blue) n = 3 clusters. One might expect that the negative charge is solvated more effectively when the Ar tag is present, increasing the VDE; however, the two spectra are very similar at the current resolution (about 50 meV), which indicates that the tag is weakly bound.

As n increases [Figure 29 (a) and (b)], it is evident that the electron binding energy also increases. The increase in the electron binding energy also is apparent by the decrease in the radius of the raw velocity map image (insets in Figure 29). Furthermore, the negative anisotropy parameter (β) of the image is less evident in the larger clusters, as the most intense region of the image is at the center. It is important to point out that the VDE approaches the energy of the excitation laser (2.33 eV) in the n = 4 and 5 clusters, causing the cross-section to fall off according to the Wigner Threshold law.[265] Thus, we present these results simply to demonstrate the increase in the VDE rather than to provide an accurate measurement, which would require modifications to our imaging apparatus to allow higher frequency excitations.

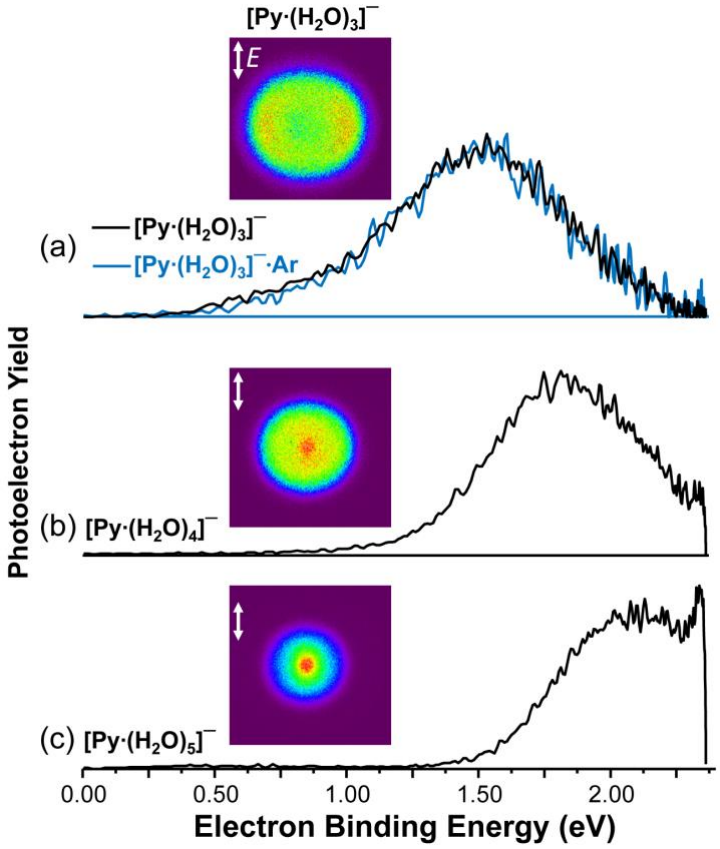

Figure 29: Photoelectron spectra of $[Py\cdot(H_2O)_n]^-$ with n = 3-5 [(a), (b), and (c), respectively]. Raw velocity map images are shown above each spectrum, with a white arrow denoting the orientation of the electric field vector. In trace (a), the blue spectrum corresponds to argon tagged $[Py\cdot(H_2O)_3]^-\cdot$Ar.radius of the raw velocity map image (insets in Figure 29). Furthermore, the negative anisotropy parameter (β) of the image is less evident in the larger clusters, as the most intense region of the image is at the center. It is important to point out that the VDE approaches the energy of the excitation laser (2.33 eV) in the n = 4 and 5 clusters, causing the cross-section to fall off according to the Wigner Threshold law. Thus, we present these results simply to demonstrate the increase in the VDE rather than to provide an accurate measurement, which would require modifications to our imaging apparatus to allow higher frequency excitations.

B.1.2 Tag Dependence Study

To assess the effect of the Ar tag on the vibrational predissociation spectra of the $[Py\cdot(H2O)3]^{-}\cdot Ar$, we also recorded spectra of these cluster by tagging with four Ar atoms. The full vibrational spectra of $[Py\cdot(H2O)3]^{-}\cdot Ar$ and $[Py\cdot(H2O)3]^{-}\cdot Ar4$ are compared in Figure 30. The spectrum in trace (a) was obtained by monitoring the photofragmentation of the singly-tagged adduct to form bare $[Py\cdot(H2O)3]^{-}$ photofragments. Note that transitions do not occur in the free OH stretching region (above 3500 cm-1) because the vibrational autodetachment channel, in which neutral fragments are generated, dominates in the high energy region of the spectrum (see section III.D. of the manuscript). Traces (b)-(d) are spectra of $[Py\cdot(H2O)3]^{-}\cdot Ar4$, which were obtained by monitoring production of $[Py\cdot(H2O)3]^{-}\cdot Arn$, photofragments, with n = 0-2, respectively. At high energies (above 2400 cm-1) all tag atoms are evaporated yielding the spectrum in Figure 30(b). Apparently, the additional solvation energy of the four Ar atoms increases the AEA enough that the free OH stretches (ν_{OH}^{free}) become apparent. Between 1600 and 2400 cm-1, production of $[Py\cdot(H2O)3]^{-}\cdot Ar$ (loss of 3 Ar atoms) dominates [trace (c)], while predominantly $[Py\cdot(H2O)3]^{-}\cdot Ar2$ (loss of 2 Ar atoms) is produced below 1600 cm-1 [trace (d)]. The peak positions and band shapes in traces (b)-(d) are very similar to those of the singly tagged species, suggesting that the tag does not significantly perturb the spectrum of $[Py\cdot(H2O)3]^{-}$.

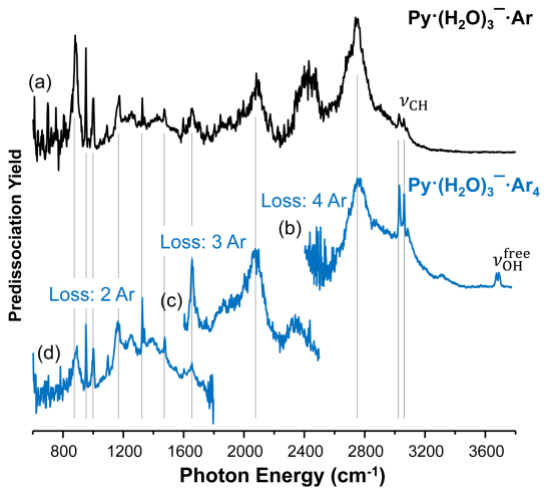

Figure 30: Tag dependence study of Py·(H2O)3−·Arn, which compares the n = 1 species (a) with the n = 4 species in the loss of 4 (b), 3 (c), and 2 (d) Ar channels (blue traces).

To estimate the binding strength of the tag, we plotted the average number of tag molecules evaporated against the photon energy (Figure 31). The average number of Ar molecules lost ($\Delta\bar{n}$) at a given photon energy was determined by integrating the total photofragmentation signal and multiplying the fractional contribution of each loss channel (χ_i) by the number of tags lost by that channel (n_i) as described below:

$$\Delta\bar{n} = \sum_i \chi_i n_i. \qquad \textbf{64}$$

The same procedure was used by Kamrath et al. to measure the binding energies of H_2 tags on simple peptides.

The linear correlation in Figure 31 confirms that the binding energy of all four tags is similar. Therefore, the average binding energy (735 cm^{-1}) was estimated by the inverse slope of

the best-fit equation. Note that this approximation assumes that the electron loss channel was insignificant near 2500 cm^{-1}.

B.1.3 Calculated Isomeric Forms of $PyH\cdot(H_2O)_n\cdot OH^-$, with n = 3-5

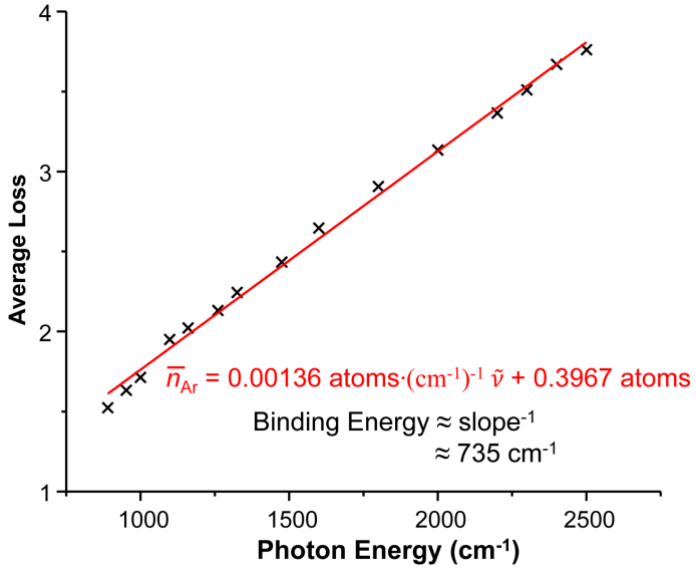

Figure 31: Dependence of the average number of Ar atoms evaporated ($\bar{n}_{Ar}$) on the photon energy used for photofragmentation. The line of best fit is given in red, as well as the average binding energy (inverse slope).

To determine the extent of the electron induced proton mediated charge transfer, we compare the experimental predissociation spectra to calculated harmonic spectra of the lowest energy isomers of $PyH\cdot(H_2O)_n\cdot OH^-$, with n = 3-5. Figure 32 presents the results for two low-lying n=3 isomers calculated using B3LYP/aug-cc-pVTZ. Structures and relative energies (zero-point corrected) calculated for various isomers of the n = 4 and 5 species are shown in Figure 33, and Figure 34, respectively, with the corresponding spectra given in Figure 35 and Figure 36.

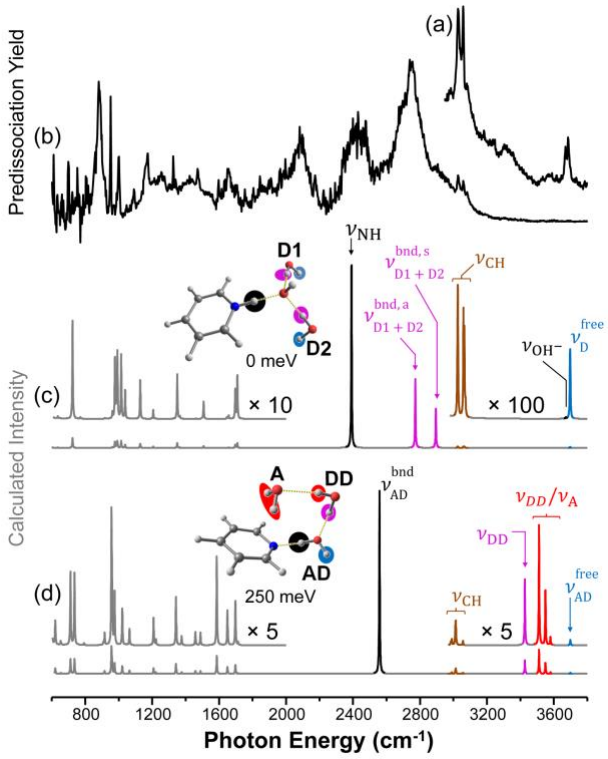

Figure 32: Comparison of the combined photo-induced vibrational autodetachment (a) and Ar-predissociation (b) spectra of $[Py\cdot(H_2O)_3]^-$ to spectra calculated at the B3LYP/aug-cc-pVTZ level of theory [(c)-(d)]. The geometries are displayed above each spectrum, where the colors of the highlighted bonds correspond to the OH and NH stretches labelled in the calculated spectra. Relative energies are displayed below each structure.

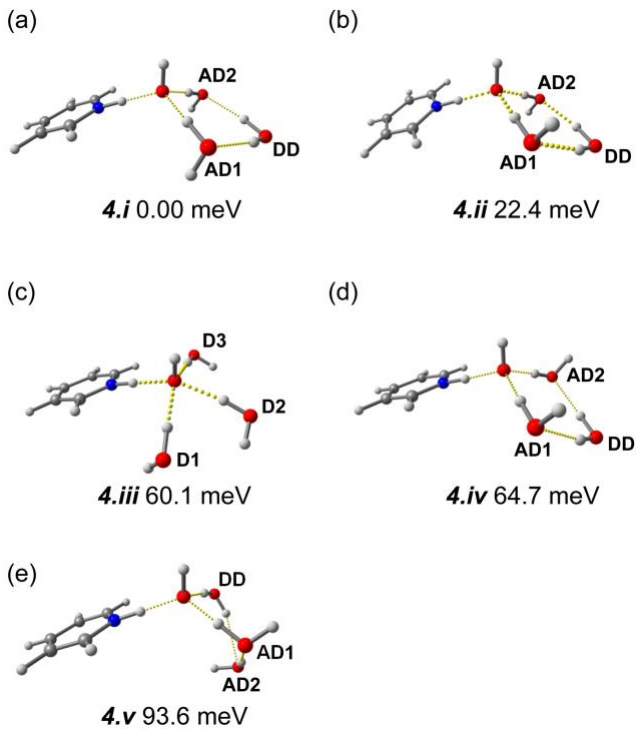

Figure 33: Structures of $Py\cdot(H_2O)_4^-$ isomers and relative energies calculated at the B3LYP/aug-cc-pVTZ level of theory.

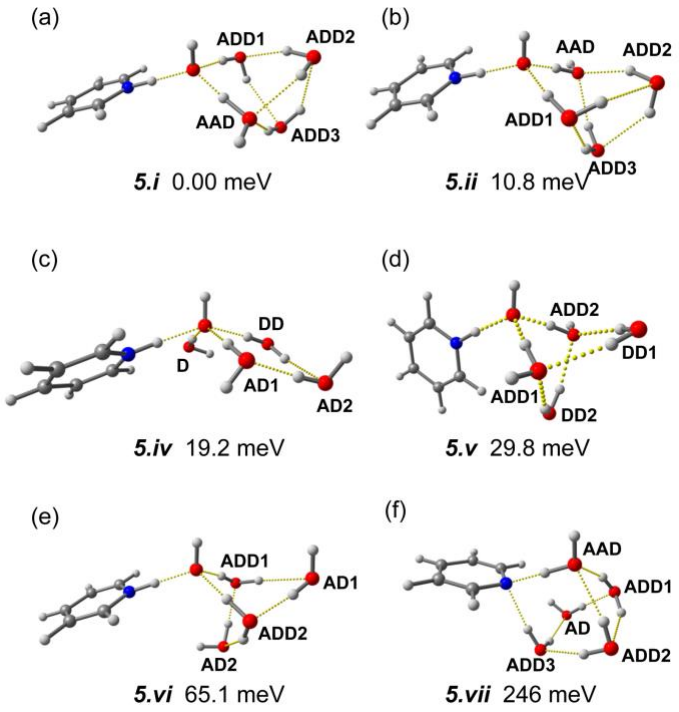

Figure 34: Structures of $Py\cdot(H_2O)_5^-$ isomers and relative energies calculated at the B3LYP/aug-cc-pVTZ level of theory.

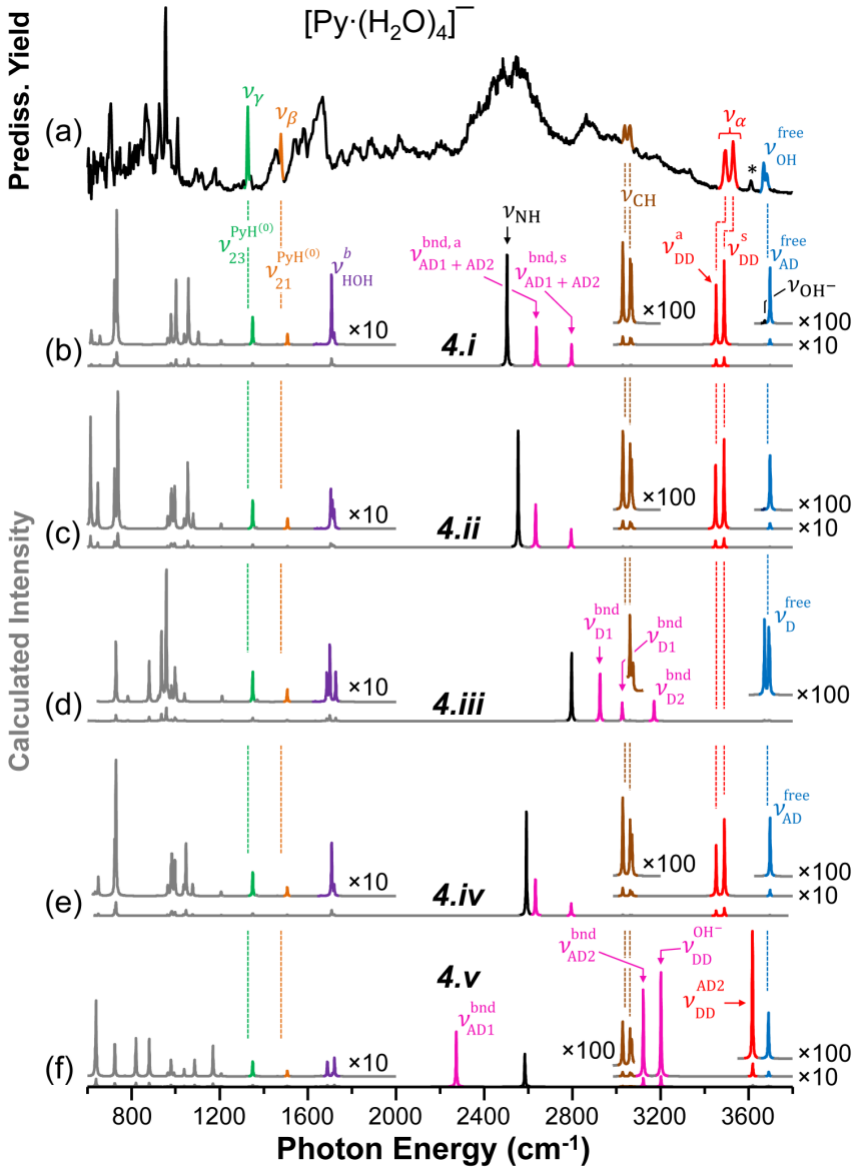

Figure 35: Comparison of the Ar-predissociation spectrum of $[Py\cdot(H_2O)_4]^-$ (a) to spectra calculated at the B3LYP/aug-cc-pVTZ level of theory [(b)-(f)]. The Roman numeral labels refer to the structures in Figure 33. Bands are assigned according to their number of H-bond acceptor (A) and donor (D) interactions of specific water molecules within the network, and are consistent with the manuscript.

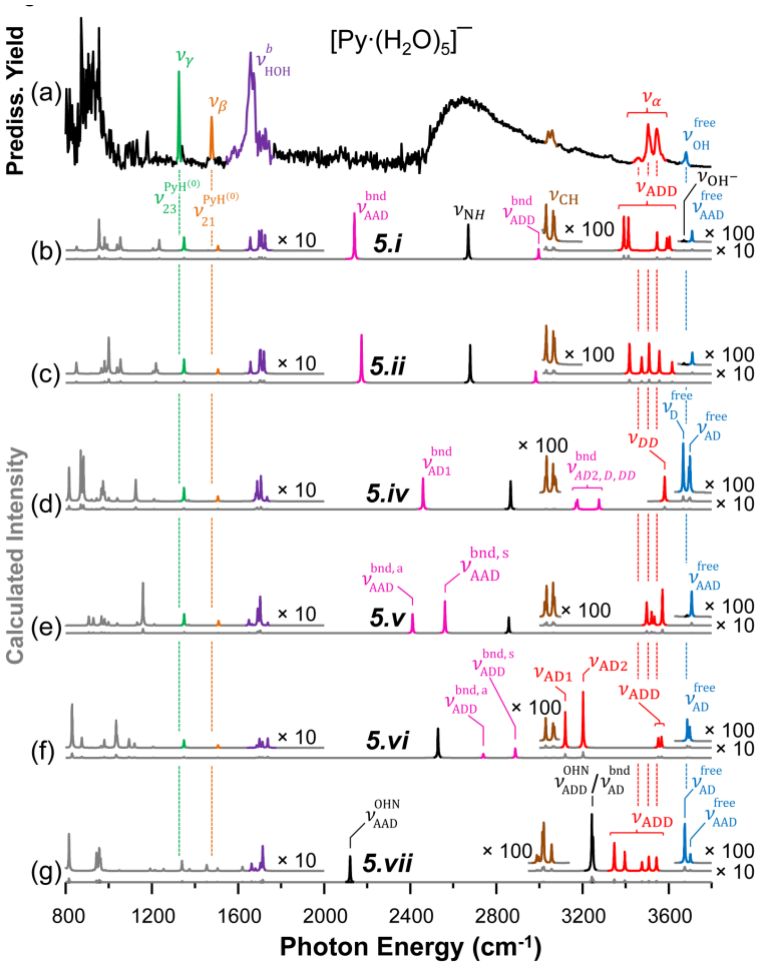

Figure 36: Comparison of the Ar-predissociation spectrum of $[Py\cdot(H_2O)_5]^-$ (a) to spectra calculated at the B3LYP/aug-cc-pVTZ level of theory [(b)-(g)]. The Roman numeral labels refer to the structures in Figure 34. Bands are assigned according to their number of H-bond acceptor (A) and donor (D) interactions of specific water molecules within the network and are consistent with the manuscript. The importance of long-range interactions for the proton transfer and subsequent reconfigurations of the hydroxide stabilizing water network, are not taken into account by the B3LYP functional. In an attempt to account for these factors, we used the M06-2X functional, with the resulting structures, minimum energies and harmonic vibrational spectra summarized for n = 3-5 in Figure 37-Figure 39, respectively. While both functionals establish the formation of the pyridinium radical [$Py_{(0)}$] for clusters comprising of n =4 and n =5 water molecules, interplay between the solvent network and the radical ring are strongly enhanced for M06-2X. These calculations suggest a π-type interaction of a single water molecule with the center of the ring, where B3LYP prefers a scenario in which the ring exhibits a hydrophobic character.

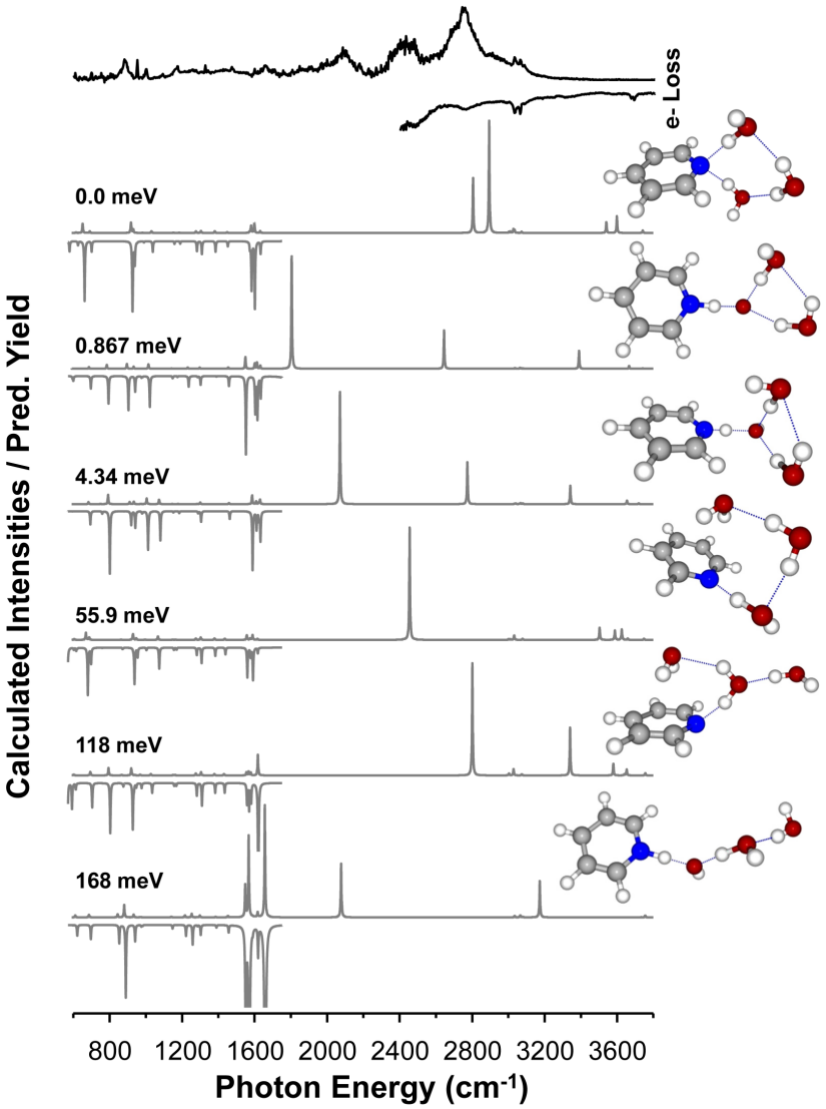

Figure 37: Comparison of the Ar-predissociation spectrum of $[Py\cdot(H_2O)_3]^-$ (a) to spectra calculated at the M06-2X/6-31++G(d,p) level of theory [(b)-(g)]. Structures and relative energies are included with each spectrum.

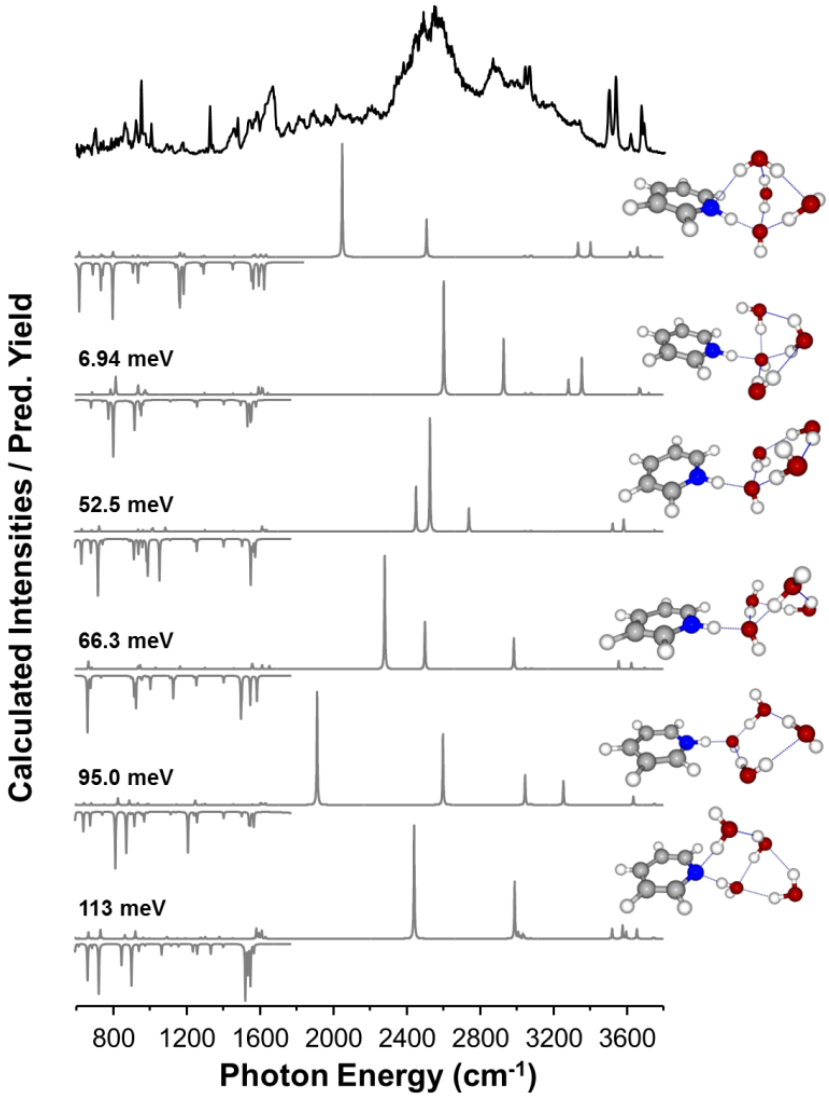

Figure 38: Comparison of the Ar-predissociation spectrum of $[Py\cdot(H_2O)_4]^-$ (a) to spectra calculated at the M06-2X/6-31++G(d,p) level of theory [(b)-(g)]. Structures and relative energies are included with each spectrum.

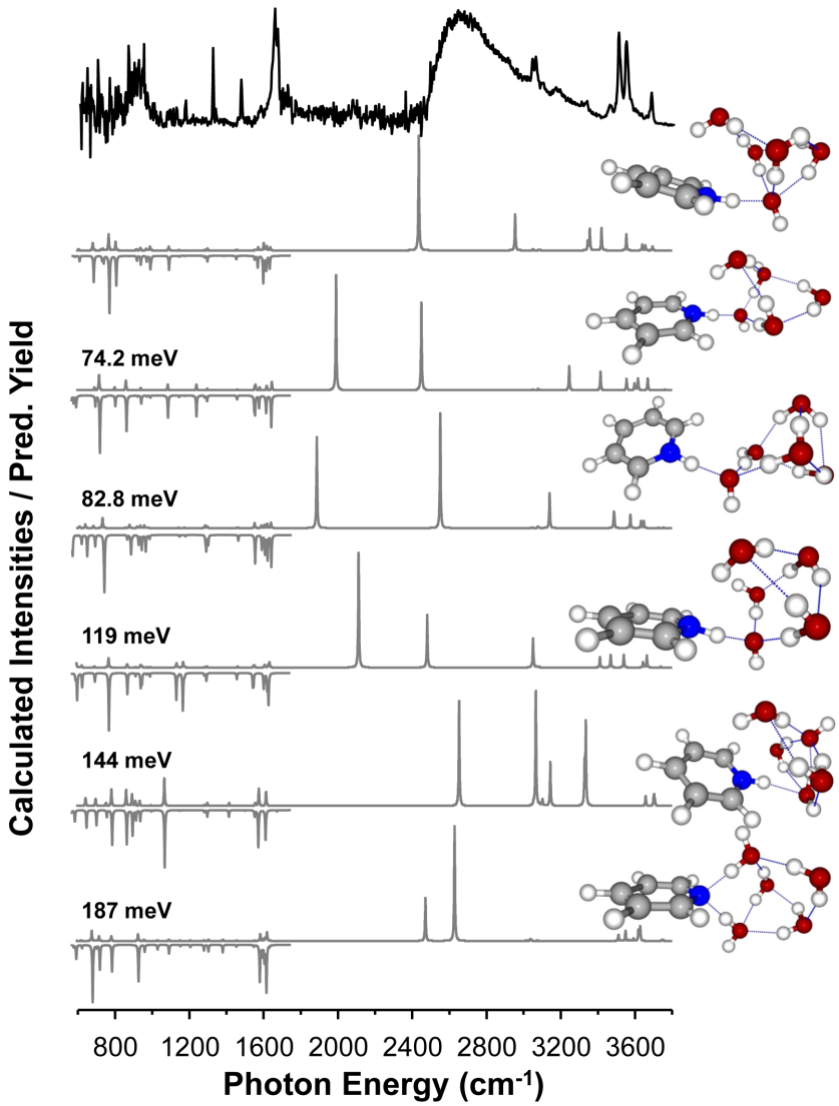

Figure 39: Comparison of the Ar-predissociation spectrum of $[Py\cdot(H_2O)_5]^-$ (a) to spectra calculated at the M06-2X/6-31++G(d,p) level of theory [(b)-(g)]. Structures and relative energies are included with each spectrum.

B.1.4 Double Resonance Spectroscopy of $[Py\cdot(H_2O)_4]^-$

Isomer specific double resonance spectroscopy was used to evaluate the possibility of multiple isomers in $[Py\cdot(H_2O)_4]^-$. In this experiment, a probe laser is fixed on a particular transition, while a hole-burning pump laser is tuned throughout the region of interest. The photofragmentation signal of the probe laser is monitored to record an isomer specific dip spectrum. This set-up employs two laser interaction zones and three stages of mass selection so that each photofragment is mass-isolated and is described elsewhere in more detail.

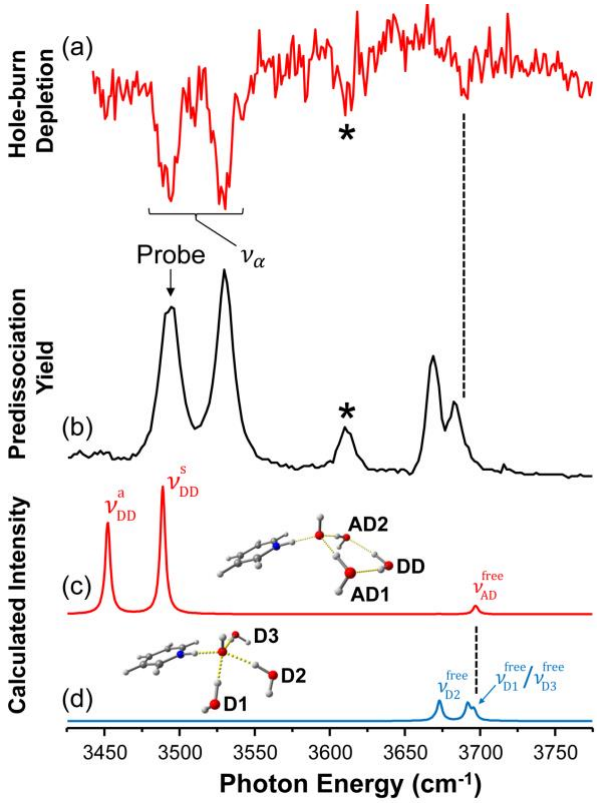

Figure 40: IR-IR double resonance spectrum (red) of $[Py\cdot(H_2O)_4]^-\cdot Ar$ (a). The probe laser was set to 3494cm^{-1} (indicated by arrow). The vibrational pre-dissociation spectrum in this region is given in trace (b). Structures of feasible low-energy isomers and calculated harmonic spectra at the B3LYP/aug-cc-pVTZ level of theory are given in (c) and (d). The asterisk marks a transition that was not predicted in the harmonic level calculations.

As shown in Figure 42, the probe laser remained fixed on the lowest energy transition for solvation shell OH stretching (3494 cm^{-1}), while the pump (hole burning) laser was tuned between 3450 and 3775 cm^{-1}. As indicated by the asterisk, the peak that was not anticipated at the harmonic level of theory is evident in the double resonance spectrum [Figure 42 (a)], suggesting that it belongs to the same isomer. Higher in energy, free OH stretching is also visible; however, it appears that the lowest energy member of the doublet has disappeared in the hole-burning spectrum. It is possible that a second isomer is present that does not contain water molecules in the second solvation shell, which gives rise to the lower energy member of the doublet. It is also possible that the splitting results from isomers that differ in the placement of the Ar tag (*i.e.*, bound to one of the free OH groups vs. elsewhere). For example, similar isomer splittings in free OH stretches were attributed to a tag effect in 1,8-disubstituted naphthalene derivatives.

B.2 Supplementary Information for "Structural and Electronic Properties of Ultrathin Picene Films on the Ag(100) Surface"

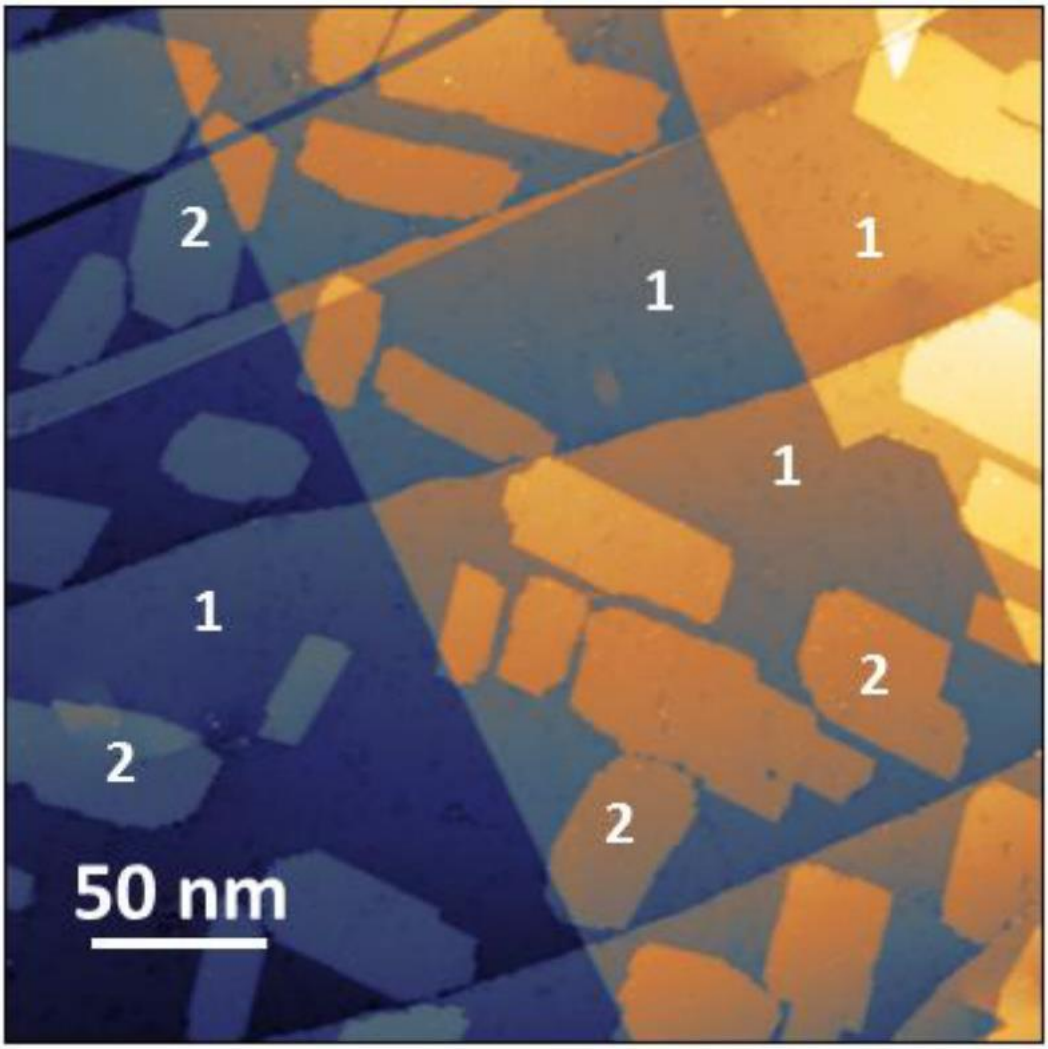

Figure 41: STM image of picene epilayer at an intermediate coverage between phase 1 (indicated by 1) and phase 2 (indicated by 2). Phase 2 clearly grows as islands.

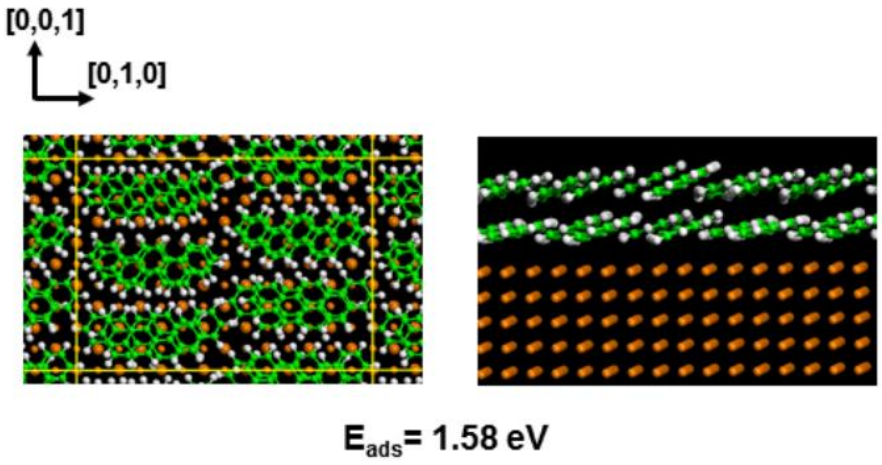

Figure 42: Adsorption configuration of a picene bilayer composed of twelve molecules distributed over two rows (each containing two layers) on Ag(100). Initially, all molecules were lying flat parallel to the surface and they become tilted upon optimization. Calculations were performed using the 7 x 5 supercell.

Bibliography

[1] R. Mcweeny, G. Diercksen, R.G. Parr, J.E. Brown, Self-Consistent Perturbation Theory. I. General Formulation and Some Applications The, J. Chem. Phys. 49 (1968) 5648. doi:10.1063/1.1669970.

[2] J.A. Pople, R.K. Nesbet, Self-consistent orbitals for radicals, J. Chem. Phys. 22 (1954) 571–572. doi:10.1063/1.1740120.

[3] C.C.J. Roothan, Hartree Fock Theory, Rev. Mod. Phys. 23 (1951) 69.

[4] M. Nooijen, R.J. Bartlett, Equation of motion coupled cluster method for electron attachment, J. Chem. Phys. 102 (1995) 3629–3647. doi:10.1063/1.468592.

[5] J.F. Stanton, R.J. Bartlett, The equation of motion coupled-cluster method. A systematic biorthogonal approach to molecular excitation energies, transition probabilities, and excited state properties, J. Chem. Phys. 98 (1993) 7029. doi:10.1063/1.464746.

[6] C. Peng, H. Schlegel, Bernhard, Combining Synchronous Transit and Quasi-Newton Methods to Find Transition States., Isr. J. Chem. 33 (1993) 449–454. doi:10.1002/ijch.199300051.

[7] G. Henkelman, B.P. Uberuaga, H. Jó, A climbing image nudged elastic band method for finding saddle points and minimum energy paths, J. Chem. Phys. 113 (2000) 9901–9904. http://theory.cm.utexas.edu/henkelman/pubs/henkelman00_9901.pdf (accessed October 26, 2018).

[8] S.A. Trygubenko, D.J. Wales, A doubly nudged elastic band method for finding transition states, J. Chem. Phys. 120 (2004) 2082–2094. doi:10.1063/1.1636455.

[9] U.W. Schmitt, G.A. Voth, The computer simulation of proton transport in water, J. Chem. Phys. 111 (1999) 9361–9381. doi:10.1063/1.480032.

[10] J. Aqvist, A. Warshel, Simulation of Enzyme Reactions Using Valence Bond Force Fields and Other Hybrid Quantum/Classical Approaches, 1993. https://pubs.acs.org/sharingguidelines (accessed February 27, 2019).

[11] G.A. Worth, L.S. Cederbaum, BEYOND BORN-OPPENHEIMER: Molecular Dynamics Through a Conical Intersection, Annu. Rev. Phys. Chem. 55 (2004) 127–58. doi:10.1146/annurev.physchem.55.091602.094335.

[12] A. Markmann, A.M. Adiabatic, D. Representations, Born-Oppenheimer Non-Adiabatic Diabatic Appendix ADIABATIC AND DIABATIC REPRESENTATIONS, 2005. http://ursula.chem.yale.edu/~batista/personal/Andreas/academic/talk05diabatic.pdf

(accessed February 19, 2019).

[13] C. Møller, M.S. Plesset, Note on an Approximation Treatment for Many-Electron Systems, Phys. Rev. 46 (1934) 618–622. doi:10.1103/PhysRev.46.618.

[14] R.J. Bartlett, G.D. Purvis, Many-body perturbation theory, coupled-pair many-electron theory, and the importance of quadruple excitations for the correlation problem, Int. J. Quantum Chem. 14 (1978) 561–581. doi:10.1002/qua.560140504.

[15] P. Hohenberg, W. Kohn, Inhomogeneous Electron Gas, Phys. Rev. 136 (1964) B864–B871. doi:10.1103/PhysRev.136.B864.

[16] W. Kohn, L.J. Sham, Self-consistent equations including exchange and correlation effects, Phys. Rev. 140 (1965) A1133–A1138. doi:10.1103/PhysRev.140.A1133.

[17] C. Lee, W. Yang, R.G. Parr, Development of the Colle-Salvetti correlation-energy formula into a functional of the electron density, 1989. doi:10.1016/0009-2614(89)85118-8.

[18] D.R. Salahub, M.C. Zerner, eds., The Challenge of d and f Electrons, American Chemical Society, Washington, DC, 1989. doi:10.1021/bk-1989-0394.

[19] H. Koch, P. Jo/rgensen, Coupled cluster response functions, J. Chem. Phys. 93 (1990) 3333–3344. doi:10.1063/1.458814.

[20] H. Koch, R. Kobayashi, A. Sanchez de Merás, P. Jo/rgensen, Calculation of size-intensive transition moments from the coupled cluster singles and doubles linear response function, J. Chem. Phys. 100 (1994) 4393–4400. doi:10.1063/1.466321.

[21] A. Szabo, N.S. Ostlund, Modern quantum chemistry : introduction to advanced electronic structure theory, Dover Publications, 1996.

[22] D.R. Hartree, The Wave Mechanics of an Atom with a Non-Coulomb Central Field. Part I. Theory and Methods, Math. Proc. Cambridge Philos. Soc. 24 (1928) 89–110. doi:10.1017/S0305004100011919.

[23] J.C. Slater, A Simplification of the Hartree-Fock Method, Phys. Rev. 81 (1951) 385–390. doi:10.1103/PhysRev.81.385.

[24] C.C.J. Roothaan, New Developments in Molecular Orbital Theory, Rev. Mod. Phys. 23 (1951) 69–89. doi:10.1103/RevModPhys.23.69.

[25] M. Levy, Universal variational functionals of electron densities, first-order density matrices, and natural spin-orbitals and solution of the v-representability problem., Proc. Natl. Acad. Sci. U. S. A. 76 (1979) 6062–5. doi:10.1073/pnas.76.12.6062.

[26] V. Sahni, J. Gruenebaum, J.P. Perdew, Study of the density-gradient expansion for the exchange energy, Phys. Rev. B. 26 (1982) 4371–4377. doi:10.1103/PhysRevB.26.4371.

[27] J. Harris, R.O. Jones, The surface energy of a bounded electron gas, J. Phys. F Met. Phys. 4 (1974) 1170–1186. doi:10.1088/0305-4608/4/8/013.

[28] J.P. Perdew, Jacob's ladder of density functional approximations for the exchange-correlation energy, AIP Conf. Proc. 577 (2001) 1–20. doi:10.1063/1.1390175.

[29] M. Zbiri, M. Johnson, H. Schober, S. Rols, N. Qureshi, S. Clarke, R. Mittal, Introduction to the density functional formalism and some illustrative applications to magnetism, École Thématique La Société Française La Neutron. 12 (2011) 77–104. doi:10.1051/sfn/201112005.

[30] D. Bohm, D. Pines, A Collective Description of Electron Interactions. I. Magnetic Interactions, Phys. Rev. 82 (1951) 625–634. doi:10.1103/PhysRev.82.625.

[31] D. Pines, D. Bohm, A Collective Description of Electron Interactions: II. Collective vs Individual Particle Aspects of the Interactions, Phys. Rev. 85 (1952) 338–353. doi:10.1103/PhysRev.85.338.

[32] D. Bohm, D. Pines, A Collective Description of Electron Interactions: III. Coulomb Interactions in a Degenerate Electron Gas, Phys. Rev. 92 (1953) 609–625. doi:10.1103/PhysRev.92.609.

[33] E. Fermi, E. Armaldi, Mem. della Cl. di Sci. Fis. Mat. e Nat, in: R. Accad. d'Italia, Rome, 1934: p. 119. https://scholar.google.com/scholar_lookup?hl=en&publication_year=1934&pages=119&author=E.+Fermiauthor=E.+Amaldi.

[34] J.P. Perdew, A. Zunger, Self-interaction correction to density-functional approximations for many-electron systems, Phys. Rev. B. 23 (1981) 5048–5079. https://journals.aps.org/prb/pdf/10.1103/PhysRevB.23.5048 (accessed May 20, 2019).

[35] M.J. Allen, D.J. Tozer, Helium dimer dispersion forces and correlation potentials in density functional theory, J. Chem. Phys. 117 (2002) 11113–11120. doi:10.1063/1.1522715.

[36] U. Zimmerli, M. Parrinello, P. Koumoutsakos, Dispersion corrections to density functionals for water aromatic interactions, J. Chem. Phys. 120 (2004) 2693–2699. doi:10.1063/1.1637034.

[37] S. Tsuzuki, H.P. Lüthi, Interaction energies of van der Waals and hydrogen bonded systems calculated using density functional theory: Assessing the PW91 model, J. Chem. Phys. 114 (2001) 3949–3957. doi:10.1063/1.1344891.

[38] J.M. Pérez-Jordá, A.D. Becke, A density-functional study of van der Waals forces: rare gas diatomics, 1995. doi:10.1016/0009-2614(94)01402-H.

[39] J.M. Pérez-Jordá, E. San-Fabián, A.J. Pérez-Jiménez, Density-functional study of van der Waals forces on rare-gas diatomics: Hartree-Fock exchange, J. Chem. Phys. 110 (1999) 1916–1920. doi:10.1063/1.477858.

[40] P. Hobza, J. šponer, T. Reschel, Density functional theory and molecular clusters, J. Comput. Chem. 16 (1995) 1315–1325. doi:10.1002/jcc.540161102.

[41] S. Kristyhn, P. Pulay, Can (semi) local density functional theory account for the London dispersion forces ?, (1994).

[42] N. Kurita, Ab initio and DFT studies for accurate description of van der Waals interaction between He atoms, 2001. doi:10.1016/S0009-2614(01)01089-2.

[43] J. Seponer, J. Leszczynski, P. Hobza, Base stacking in cytosine dimer. A comparison of correlatedab initio calculations with three empirical potential models and density functional theory calculations, J. Comput. Chem. 17 (2003) 841–850. doi:10.1002/(sici)1096-987x(199605)17:7<841::aid-jcc8>3.0.co;2-s.

[44] P. Taylor, B.G. Lippert, J. Hutter, M. Parrinello, Molecular Physics : An International Journal at the Interface Between Chemistry and Physics A hybrid Gaussian and plane wave density functional scheme, (2010) 37–41.

[45] O. Couronne, Y. Ellinger, An ab initio and DFT study of $(N_2)_2$ dimers, Chem. Phys. Lett. 306 (1999) 71–77. doi:10.1016/S0009-2614(99)00431-5.

[46] S. Grimme, Accurate description of van der Waals complexes by density functional theory including empirical corrections, J. Comput. Chem. 25 (2004) 1463–1473. doi:10.1002/jcc.20078.

[47] S. Grimme, Semiempirical GGA-type density functional constructed with a long-range dispersion correction, J. Comput. Chem. 27 (2006) 1787–1799. doi:10.1002/jcc.20495.

[48] S. Grimme, J. Antony, S. Ehrlich, H. Krieg, A consistent and accurate ab initio parametrization of density functional dispersion correction (DFT-D) for the 94 elements H-Pu, J. Chem. Phys. 132 (2010) 154104. doi:10.1063/1.3382344.

[49] S. Grimme, Density functional theory with London dispersion corrections, Ltd. WIREs Comput Mol Sci. 1 (2011) 211–228. doi:10.1002/wcms.30.

[50] S. Grimme, S. Ehrlich, L. Goerigk, Effect of the damping function in dispersion corrected density functional theory, J. Comput. Chem. 32 (2011) 1456–1465. doi:10.1002/jcc.21759.

[51] J. Gräfenstein, D. Cremer, An efficient algorithm for the density-functional theory treatment of dispersion interactions, J. Chem. Phys. 130 (2009) 124105. doi:10.1063/1.3079822.

[52] L. Goerigk, A Comprehensive Overview of the DFT-D3 London-Dispersion Correction, Non-Covalent Interact. Quantum Chem. Phys. Theory Appl. (2017) 195–219. doi:10.1016/B978-0-12-809835-6.00007-4.

[53] E.R. Johnson, I.D. Mackie, G.A. DiLabio, Dispersion interactions in density-functional theory, J. Phys. Org. Chem. 22 (2009) 1127–1135. doi:10.1002/poc.1606.

[54] T. Sato, H. Nakai, Local response dispersion method. II. Generalized multicenter interactions, J. Chem. Phys. 133 (2010) 224104. doi:10.1063/1.3503040.

[55] F. London, Zur Theorie und Systematik der Molekularkräfte, 1930. doi:10.1007/BF01421741.

[56] A.J. Stone, The Theory of Intermolecular Forces, Oxford University Press, 2013. doi:10.1093/acprof:oso/9780199672394.001.0001.

[57] I.G. Kaplan, Intermolecular Interactions: Physical Picture, Computational Methods and Model Potentials. www.wiley.com (accessed May 16, 2019).

[58] A.D. Becke, Density-functional exchange-energy approximation with correct asymptotic behavior, Phys. Rev. A. 38 (1988) 3098–3100. doi:10.1103/PhysRevA.38.3098.

[59] C. Lee, W. Yang, R.G. Parr, Development of the Colle-Salvetti correlation-energy formula into a functional of the electron density, Phys. Rev. B. 37 (1988) 785–789. doi:10.1103/PhysRevB.37.785.

[60] A.D. Becke, Density-functional thermochemistry. III. The role of exact exchange, J. Chem. Phys. 98 (1993) 5648. doi:10.1063/1.464913.

[61] S. Kristyán, P. Pulay, Can (semi)local density functional theory account for the London dispersion forces?, 1994. doi:10.1016/0009-2614(94)01027-7.

[62] G. Starkschall, R.G. Gordon, Calculation of Coefficients in the Power Series Expansion of the Long-Range Dispersion Force between Atoms, J. Chem. Phys. 56 (1972) 2801–2806. doi:10.1063/1.1677610.

[63] S. Grimme, J. Antony, S. Ehrlich, H. Krieg, A consistent and accurate ab initio parametrization of density functional dispersion correction (DFT-D) for the 94 elements H-Pu, J. Chem. Phys. 132 (2010). doi:10.1063/1.3382344.

[64] S. Grimme, Semiempirical GGA-type density functional constructed with a long-range dispersion correction, J. Comput. Chem. 27 (2006) 1787–1799. doi:10.1002/jcc.20495.

[65] G.A. Dilabio, A. Otero-De-La-Roza, Noncovalent Interactions in DensIty Functional theory, 2016. https://onlinelibrary.wiley.com/doi/pdf/10.1002/9781119148739.ch1 (accessed May 16, 2019).

[66] S. Grimme, Semiempirical GGA-type density functional constructed with a long-range dispersion correction, J. Comput. Chem. 27 (2006) 1787–1799. doi:10.1002/jcc.20495.

[67] J.P. Perdew, K. Burke, M. Ernzerhof, Generalized Gradient Approximation Made Simple, Phys. Rev. Lett. 77 (1996) 3865–3868. doi:10.1103/PhysRevLett.77.3865.

[68] J.P. Perdew, K. Burke, M. Ernzerhof, ERRATA Generalized Gradient Approximation Made Simple [Phys. Rev. Lett. 77, 3865 (1996)], Phys. Rev. Lett. 78 (1997) 1396.

https://journals.aps.org/prl/pdf/10.1103/PhysRevLett.78.1396 (accessed May 31, 2019).

[69] A.D. Becke, Density-functional thermochemistry. V. Systematic optimization of exchange-correlation functionals, J. Chem. Phys. 107 (1997) 8554–8560. doi:10.1063/1.475007.

[70] Y. Zhao, D.G. Truhlar, The M06 suite of density functionals for main group thermochemistry, thermochemical kinetics, noncovalent interactions, excited states, and transition elements: two new functionals and systematic testing of four M06-class functionals and 12 other function, Theor. Chem. Acc. 120 (2008) 215–241. doi:10.1007/s00214-007-0310-x.

[71] C. Adamo, V. Barone, Toward reliable density functional methods without adjustable parameters: The PBE0 model, J. Chem. Phys. 110 (1999) 6158–6170. doi:10.1063/1.478522.

[72] Y. Zhao, N.E. Schultz, D.G. Truhlar, Exchange-correlation functional with broad accuracy for metallic and nonmetallic compounds, kinetics, and noncovalent interactions, J. Chem. Phys. 123 (2005) 161103. doi:10.1063/1.2126975.

[73] J. Da Chai, M. Head-Gordon, Long-range corrected hybrid density functionals with damped atom-atom dispersion corrections, Phys. Chem. Chem. Phys. 10 (2008) 6615–6620. doi:10.1039/b810189b.

[74] K. Pernal, R. Podeszwa, K. Patkowski, K. Szalewicz, Dispersionless density functional theory, Phys. Rev. Lett. 103 (2009). doi:10.1103/PhysRevLett.103.263201.

[75] P. Jurečka, J. Černý, P. Hobza, D.R. Salahub, Density functional theory augmented with an empirical dispersion term. Interaction energies and geometries of 80 noncovalent complexes compared with ab initio quantum mechanics calculations, J. Comput. Chem. 28 (2007) 555–569. doi:10.1002/jcc.20570.

[76] J. Da Chai, M. Head-Gordon, Systematic optimization of long-range corrected hybrid density functionals, J. Chem. Phys. 128 (2008). doi:10.1063/1.2834918.

[77] B.M. Axilrod, E. Teller, Interaction of the van der Waals Type Between Three Atoms, J. Chem. Phys. 11 (1943) 299. doi:10.1063/1.1723844.

[78] Y. Muto, Force between nonpolar molecules, J. Phys. Math. Soc. Jpn. 17 (1943) 629–631.

[79] B. Jeziorski, R. Moszynski, K. Szalewicz, Perturbation Theory Approach to Intermolecular Potential Energy Surfaces of van der Waals Complexes, 1994. doi:10.1021/cr00031a008.

[80] P.-O. Löwdin, Twenty-five years of Sanibel symposia: A brief historic and scientific survey, Int. J. Quantum Chem. 28 (2009) 19–37. doi:10.1002/qua.560280805.

[81] C. Møller, M.S. Plesset, Note on an Approximation Treatment for Many-Electron Systems, Phys. Rev. 46 (1934) 618–622. doi:10.1103/PhysRev.46.618.

[82] L. Brillouin, Les problèmes de perturbations et les champs self-consistents, J. Phys. Le Radium. 3 (1932) 373–389. doi:10.1051/jphysrad:0193200309037300.

[83] D. Cremer, Møller-Plesset perturbation theory: from small molecule methods to methods for thousands of atoms, Ltd. WIREs Comput Mol Sci. 1 (2011) 509–530. doi:10.1002/wcms.58.

[84] R.J. Bartlett, J. Noga, The expectation value coupled-cluster method and analytical energy derivatives, Chem. Phys. Lett. 150 (1988) 29–36. doi:10.1016/0009-2614(88)80392-0.

[85] J.D. Watts, J. Gauss, R.J. Bartlett, Coupled-cluster methods with noniterative triple excitations for restricted open-shell Hartree-Fock and other general single determinant reference functions. Energies and analytical gradients, J. Chem. Phys. 98 (1993) 8718–8733. doi:10.1063/1.464480.

[86] J.F. Stanton, J. Gauss, Perturbative treatment of the similarity transformed Hamiltonian in equation-of-motion coupled-cluster approximations, J. Chem. Phys. 103 (1995) 1064–1076. doi:10.1063/1.469817.

[87] M. Nooijen, R.J. Bartlett, Equation of motion coupled cluster method for electron attachment Equation of motion coupled cluster method for electron attachment, 3629 (1995). doi:10.1063/1.468592.

[88] E. Fermi, E. Teller, The Capture of Negative Mesotrons in Matter, Phys. Rev. 72 (1947) 399–408. doi:10.1103/PhysRev.72.399.

[89] K.D. Jordan, F. Wang, Theory of Dipole-Bound Anions, Annu. Rev. Phys. Chem. 54 (2003) 367–396. doi:10.1146/annurev.physchem.54.011002.103851.

[90] D.M. Chipman, Gaussian basis sets for calculation of spin densities in first-row atoms, Theor. Chim. Acta. 76 (1989) 73–84. doi:10.1007/BF00532125.

[91] Y. Zhang, P.M. Weber, H. Jónsson, Self-Interaction Corrected Functional Calculations of a Dipole-Bound Molecular Anion, J. Phys. Chem. Lett. 7 (2016) 2068–2073. doi:10.1021/acs.jpclett.6b00742.

[92] J.A. Fournier, C.T. Wolke, M.A. Johnson, T.T. Odbadrakh, K.D. Jordan, S.M. Kathmann, S.S. Xantheas, Snapshots of Proton Accommodation at a Microscopic Water Surface: Understanding the Vibrational Spectral Signatures of the Charge Defect in Cryogenically Cooled H^+ $(H_2O)_{n=2-28}$ Clusters, (2015). doi:10.1021/acs.jpca.5b04355.

[93] D.J. Wales, OPTIM: A Program for Optimizing Geometries and Calculating Reaction Pathways, Univ. Cambridge Press. Cambridge, U.K. (2003). http://www-wales.ch.cam.ac.uk/OPTIM/.

[94] W.L. Jorgensen, J. Chandrasekhar, J.D. Madura, R.W. Impey, M.L. Klein, Comparison of simple potential functions for simulating liquid water, J. Chem. Phys. 79 (1983) 926. doi:10.1063/1.445869.

[95] E. Neria, S. Fischer, M. Karplus, Simulation of activation free energies in molecular systems, J. Chem. Phys. 105 (1996) 1902–1921. doi:10.1063/1.472061.

[96] U.W. Schmitt, G.A. Voth, Multistate Empirical Valence Bond Model for Proton Transport in Water, J. Phys. Chem. B. 102 (1998) 5547–5551. doi:10.1021/jp9818131.

[97] L.X. Dang, B.M. Pettitt, Simple intramolecular model potentials for water, J. Phys. Chem. 91 (1987) 3349–3354. doi:10.1021/j100296a048.

[98] U.W. Schmitt, G. a Voth, The computer simulation of proton transport in water, J. Chem. Phys. 111 (1999) 9361–9381. doi:10.1063/1.480032.

[99] V. Periquet, A. Moreau, S. Carles, J.P. Schermann, C. Desfrançois, Cluster size effects upon anion solvation of N-heterocyclic molecules and nucleic acid bases, J. Electron Spectros. Relat. Phenomena. 106 (2000) 141–151. doi:10.1016/S0368-2048(99)00072-9.

[100] S.Y. Han, J.K. Song, J.H. Kim, H. Bin Oh, S.K. Kim, Photoelectron spectroscopy of pyridine cluster anions, $(Py)_n^-$(n=4–13), J. Chem. Phys. 111 (1999) 4041–4050. doi:10.1063/1.480269.

[101] K. Aflatooni, G.A. Gallup, P.D. Burrow, Electron Attachment Energies of the DNA Bases, J. Phys. Chem. A. 102 (1998) 6205–6207. doi:10.1021/jp980865n.

[102] C. Desfrançois, H. Abdoul-Carim, J.-P. Schermann, Ground-State Dipole-Bound Anions, Int. J. Mod. Phys. B. 10 (1996) 1339–1395. doi:10.1142/S0217979296000520.

[103] J.P. Ziesel, I. Nenner, G.J. Schulz, Negative ion formation, vibrational excitation, and transmission spectroscopy in hydrogen halides, J. Chem. Phys. 63 (1975) 1943–1949. doi:10.1063/1.431527.

[104] P.D. Burrow, A.J. Ashe, D.J. Bellville, K.D. Jordan, Temporary anion states of phosphabenzene, arsabenzene, and stibabenzene. Trends in the .pi. and .pi.* orbital energies, J. Am. Chem. Soc. 104 (1982) 425–429. doi:10.1021/ja00366a009.

[105] D. Mathur, J.B. Hasted, Temporary negative-ion states in pyridine and diazine molecules, Chem. Phys. 16 (1976) 347–352. doi:10.1016/0301-0104(76)87030-9.

[106] K.D. Jordan, P.D. Burrow, Temporary anion states of polyatomic hydrocarbons, Chem. Rev. 87 (1987) 557–588. doi:10.1021/cr00079a005.

[107] J. Grimshaw, Electrochemical reactions and mechanisms in organic chemistry, Elsevier, 2000.

[108] V. Periquet, A. Moreau, S. Carles, J.P. Schermann, C. Desfrançois, Cluster size effects upon anion solvation of N-heterocyclic molecules and nucleic acid bases, J. Electron Spectros. Relat. Phenomena. 106 (2000) 141–151. doi:10.1016/S0368-2048(99)00072-9.

[109] K.D. Jordan, P.D. Burrow, Temporary anion states of polyatomic hydrocarbons, Chem.

Rev. 87 (1987) 557–588. doi:10.1021/cr00079a005.

[110] G.J. Schulz, Resonances in Electron Impact on Diatomic Molecules, Rev. Mod. Phys. 45 (1973) 423–486. doi:10.1103/RevModPhys.45.423.

[111] Y. Wang, X. Zhang, S. Lyapustina, M.M. Nilles, S. Xu, J.D. Graham, K.H. Bowen, J.T. Kelly, G.S. Tschumper, N.I. Hammer, The onset of electron-induced proton-transfer in hydrated azabenzene cluster anions, Phys. Chem. Chem. Phys. 18 (2016) 704–712. doi:10.1039/C5CP02746B.

[112] R.A. Relph, T.L. Guasco, B.M. Elliott, M.Z. Kamrath, A.B. McCoy, R.P. Steele, D.P. Schofield, K.D. Jordan, A.A. Viggiano, E.E. Ferguson, M.A. Johnson, How the shape of an H-bonded network controls proton-coupled water activation in HONO formation., Science. 327 (2010) 308–12. doi:10.1126/science.1177118.

[113] T. Sommerfeld, K.D. Jordan, Electron Binding Motifs of $(H_2O)_n^-$ Clusters, J. Am. Chem. Soc. 128 (2006) 5828–5833. doi:10.1021/ja0587446.

[114] T. Sommerfeld, A. DeFusco, K.D. Jordan, Model potential approaches for describing the interaction of excess electrons with water clusters: Incorporation of long-range correlation effects, J. Phys. Chem. A. 112 (2008) 11021–11035. doi:10.1021/jp806077h.

[115] J.M. Farrar, W.H. Saunders, Techniques for the study of ion-molecule reactions, Wiley, 1988. https://www.wiley.com/en-us/Techniques+for+the+Study+of+Ion+Molecule+Reactions-p-9780471848127 (accessed April 30, 2019).

[116] A. Sanov, R. Mabbs, Photoelectron imaging of negative ions, Int. Rev. Phys. Chem. 27 (2008) 53–85. doi:10.1080/01442350701786512.

[117] A.T.J.B. Eppink, D.H. Parker, Velocity map imaging of ions and electrons using electrostatic lenses: Application in photoelectron and photofragment ion imaging of molecular oxygen, Rev. Sci. Instrum. 68 (1997) 3477–3484. doi:10.1063/1.1148310.

[118] V. Dribinski, A. Ossadtchi, V.A. Mandelshtam, H. Reisler, Reconstruction of Abel-transformable images: The Gaussian basis-set expansion Abel transform method, Rev. Sci. Instrum. 73 (2002) 2634–2642. doi:10.1063/1.1482156.

[119] B.M. Elliott, L.R. McCunn, M.A. Johnson, Photoelectron imaging study of vibrationally mediated electron autodetachment in the type I isomer of the water hexamer anion, Chem. Phys. Lett. 467 (2008) 32–36. doi:10.1016/j.cplett.2008.11.008.

[120] H.K. Gerardi, K.J. Breen, T.L. Guasco, G.H. Weddle, G.H. Gardenier, J.E. Laaser, M.A. Johnson, Survey of Ar-Tagged Predissociation and Vibrationally Mediated Photodetachment Spectroscopies of the Vinylidene Anion, $C_2H_2^-$†, J. Phys. Chem. A. 114 (2010) 1592–1601. doi:10.1021/jp9095419.

[121] T. Clark, J. Chandrasekhar, G.W. Spitznagel, P.V.R. Schleyer, Efficient diffuse function-

augmented basis sets for anion calculations. III. The 3-21+G basis set for first-row elements, Li–F, J. Comput. Chem. 4 (1983) 294–301. doi:10.1002/jcc.540040303.

[122] P.C. Hariharan, J.A. Pople, The influence of polarization functions on molecular orbital hydrogenation energies, Theor. Chim. Acta. 28 (1973) 213–222. doi:10.1007/BF00533485.

[123] W.J. Hehre, R. Ditchfield, J.A. Pople, Self—Consistent Molecular Orbital Methods. XII. Further Extensions of Gaussian—Type Basis Sets for Use in Molecular Orbital Studies of Organic Molecules, J. Chem. Phys. 56 (1972) 2257–2261. doi:10.1063/1.1677527.

[124] M.J. Frisch, G.W. Trucks, H.B. Schlegel, M.A. Scuseria, M.A. Robb, J.R. Cheeseman, G. Scalmani, V. Barone, B. Mennucci, G.A. Petersson, H. Nakatsuji, M. Caricato, X. Li, H.P. Hratchian, A.F. Izmaylov, J. Bloino, G. Zheng, J.L. Sonnenberg, M. Hada, M. Ehara, K. Toyota, R. Fukuda, J. Hasegawa, M. Ishida, T. Nakajima, Y. Honda, O. Kitao, H. Nakai, T. Vreven, J.J.A. Montgomery, J.E. Peralta, F. Ogliaro, M. Bearpark, J.J. Heyd, E. Brothers, K.N. Kudin, V.N. Staroverov, R. Kobayashi, J. Normand, K. Raghavachari, A. Rendell, J.C. Burant, S.S. Iyengar, J. Tomasi, M. Cossi, N. Rega, J.M. Millam, M. Klene, J.E. Knox, J.B. Cross, V. Bakken, C. Adamo, J. Jaramillo, R. Gomperts, R.E. Stratmann, O. Yazyev, A.J. Austin, R. Cammi, C. Pomelli, J.W. Ochterski, R.L. Martin, K. Morokuma, A.D. Daniels, Ö. Farkas, J.B. Foresman, J. V. Ortiz, J. Cioslowski, D.J. Fox, GAUSSIAN 09,.

[125] The CP2K developers group (2013), CP2K is freely available from http://www.cp2k.org/,.

[126] C. Lee, W. Yang, R.G. Parr, Development of the Colle-Salvetti correlation-energy formula into a functional of the electron density, Phys. Rev. B. 37 (1988) 785–789. doi:10.1103/PhysRevB.37.785.

[127] S. Goedecker, M. Teter, J. Hutter, Separable dual-space Gaussian pseudopotentials, Phys. Rev. B. 54 (1996) 1703–1710. doi:10.1103/PhysRevB.54.1703.

[128] C. Hartwigsen, S. Goedecker, J. Hutter, Relativistic separable dual-space Gaussian pseudopotentials from H to Rn, Phys. Rev. B. 58 (1998) 3641–3662. doi:10.1103/PhysRevB.58.3641.

[129] G.J. Martyna, M.E. Tuckerman, A reciprocal space based method for treating long range interactions in *ab initio* and force-field-based calculations in clusters, J. Chem. Phys. 110 (1999) 2810–2821. doi:10.1063/1.477923.

[130] J.W. Shin, N.I. Hammer, E.G. Diken, M.A. Johnson, R.S. Walters, T.D. Jaeger, M.A. Duncan, R.A. Christie, K.D. Jordan, Infrared signature of structures associated with the $H^+(H2O)_n$ (n=6 to 27) clusters, Science (80-.). 304 (2004) 1137–1140. doi:10.1126/science.1096466.

[131] K.J. Breen, A.F. Deblase, T.L. Guasco, V.K. Voora, K.D. Jordan, T. Nagata, M.A. Johnson, Bottom-Up View of Water Network-Mediated CO 2 Reduction Using Cryogenic Cluster Ion Spectroscopy and Direct Dynamics Simulations, (2012) 903–912.

[132] R. Nakanishi, T. Nagata, Formation and photodestruction of dual dipole-bound anion

$(H_2O)_6\{e^-\}CH_3NO_2$, J. Chem. Phys. 130 (2009) 224309. doi:10.1063/1.3152636.

[133] H. Motegi, T. Takayanagi, T. Tsuneda, K. Yagi, R. Nakanishi, T. Nagata, Theoretical Study on the Excess Electron Binding Mechanism in the $[CH_3NO_2\cdot(H_2O)_n]^-$ (n = 1−6) Anion Clusters, J. Phys. Chem. A. 114 (2010) 8939–8947. doi:10.1021/jp1041124.

[134] L.A. Posey, M.A. Johnson, Photochemistry of hydrated electron clusters $(H_2O)_{-n}$ ($15 \leq n \leq 40$) at 1064 nm: Size dependent competition between photofragmentation and photodetachment, J. Chem. Phys. 89 (1988) 4807–4814. doi:10.1063/1.455674.

[135] P.J. Campagnola, D.M. Cyr, M.A. Johnson, Size-dependent collisional incorporation of D_2O into $(H_2O)_{-n}$ around n = 15: implications on the origin of magic numbers in the hydrated electron cluster distribution, Chem. Phys. Lett. 181 (1991) 206–212. doi:10.1016/0009-2614(91)90356-E.

[136] M.T. Bowers, Gas Phase Ion Chemistry, Academic Press, New York, 1979. https://books.google.com/books?hl=en&lr=&id=7Zf-BAAAQBAJ&oi=fnd&pg=PP1&dq=Gas+Phase+Ion+Chemistry%3B+(Academic+Press,+New+York,+1979)&ots=68dXjB5LDI&sig=cp53t3A95lglSDNs8bhKdPl7Xmw#v=onepage&q=Gas Phase Ion Chemistry%3B (Academic Press%2C New York%2C 1979 (accessed April 30, 2019).

[137] V. Dribinski, A. Ossadtchi, V.A. Mandelshtam, H. Reisler, Reconstruction of Abel-transformable images: The Gaussian basis-set expansion Abel transform method ARTICLES YOU MAY BE INTERESTED IN, Rev. Sci. Instrum. 73 (2002) 2634. doi:10.1063/1.1482156.

[138] J. Cooper, R.N. Zare, Angular Distribution of Photoelectrons, J. Chem. Phys. 48 (1968) 942–943. doi:10.1063/1.1668742.

[139] P.J. Campagnola, L.A. Posey, M.A. Johnson, The angular distribution of photoelectrons ejected from the hydrated electron cluster $(H_2O)^-_{18}$, J. Chem. Phys. 92 (1990) 3243–3245. doi:10.1063/1.457881.

[140] A.E. Bragg, J.R.R. Verlet, A. Kammrath, O. Cheshnovsky, D.M. Neumark, Electronic Relaxation Dynamics of Water Cluster Anions, J. Am. Chem. Soc. 127 (2005) 15283–15295. doi:10.1021/ja052811e.

[141] J. V. Coe, G.H. Lee, J.G. Eaton, S.T. Arnold, H.W. Sarkas, K.H. Bowen, C. Ludewigt, H. Haberland, D.R. Worsnop, Photoelectron spectroscopy of hydrated electron cluster anions, $(H_2O)_{-n=2-69}$, J. Chem. Phys. 92 (2002) 3980–3982. doi:10.1063/1.457805.

[142] J. Kim, I. Becker, O. Cheshnovsky, M.A. Johnson, Photoelectron spectroscopy of the `missing' hydrated electron clusters $(H_2O)_{-n}$, n=3, 5, 8 and 9: Isomers and continuity with the dominant clusters n=6, 7 and $\geqslant$11, Chem. Phys. Lett. 297 (1998) 90–96. doi:10.1016/S0009-2614(98)01109-9.

[143] J.R.R. Verlet, A.E. Bragg, A. Kammrath, O. Cheshnovsky, D.M. Neumark, Observation of

large water-cluster anions with surface-bound excess electrons., Science. 307 (2005) 93–6. doi:10.1126/science.1106719.

[144] J. V. Coe, S.T. Arnold, J.G. Eaton, G.H. Lee, K.H. Bowen, Photoelectron spectra of hydrated electron clusters: Fitting line shapes and grouping isomers, J. Chem. Phys. 125 (2006) 014315. doi:10.1063/1.2212415.

[145] P. Ayotte, C.G. Bailey, J. Kim, M.A. Johnson, Vibrational predissociation spectroscopy of the $(H_2O)_{6-}\cdot Ar_n$, $n \geqslant 6$, clusters, J. Chem. Phys. 108 (1998) 444–449. doi:10.1063/1.475406.

[146] N.I. Hammer, J.R. Roscioli, M.A. Johnson, E.M. Myshakin, K.D. Jordan, Infrared Spectrum and Structural Assignment of the Water Trimer Anion, J. Phys. Chem. A. 109 (2005) 11526–11530. doi:10.1021/jp053769c.

[147] W.H. Robertson, E.G. Diken, E.A. Price, J.-W. Shin, M.A. Johnson, Spectroscopic determination of the OH^- solvation shell in the $OH^-.(H_2O)_n$ clusters., Science. 299 (2003) 1367–72. doi:10.1126/science.1080695.

[148] M. Morita, H. Takahashi, S. Yabushita, K. Takahashi, Why does the IR spectrum of hydroxide stretching vibration weaken with increase in hydration?, Phys. Chem. Chem. Phys. 16 (2014) 23143–23149. doi:10.1039/C4CP03623A.

[149] B. Golec, P. Das, M. Bahou, Y.-P. Lee, Infrared Spectra of the 1-Pyridinium ($C_5H_5NH^+$) Cation and Pyridinyl (C_5H_5NH and 4-C_5H_6N) Radicals Isolated in Solid para-Hydrogen, J. Phys. Chem. A. 117 (2013) 13680–13690. doi:10.1021/jp407668z.

[150] K.N. Wong, S.D. Colson, The FT-IR spectra of pyridine and pyridine-d5, J. Mol. Spectrosc. 104 (1984) 129–151. doi:10.1016/0022-2852(84)90250-9.

[151] C.J. Johnson, L.C. Dzugan, A.B. Wolk, C.M. Leavitt, J.A. Fournier, A.B. McCoy, M.A. Johnson, Microhydration of Contact Ion Pairs in $M^{2+}OH^-(H_2O)_{n=1-5}$ (M = Mg, Ca) Clusters: Spectral Manifestations of a Mobile Proton Defect in the First Hydration Shell, J. Phys. Chem. A. 118 (2014) 7590–7597. doi:10.1021/jp504139j.

[152] J.R. Roscioli, E.G. Diken, M.A. Johnson, S. Horvath, A.B. McCoy, Prying Apart a Water Molecule with Anionic H-Bonding: A Comparative Spectroscopic Study of the $X^-\cdot H_2O$ (X = OH, O, F, Cl, and Br) Binary Complexes in the 600−3800 cm^{-1} Region, J. Phys. Chem. A. 110 (2006) 4943–4952. doi:10.1021/jp056022v.

[153] M. Head-Gordon, J.A. Pople, M.J. Frisch, MP2 energy evaluation by direct methods, Chem. Phys. Lett. 153 (1988) 503–506. doi:10.1016/0009-2614(88)85250-3.

[154] G.H. Gardenier, M.A. Johnson, A.B. McCoy, Spectroscopic Study of the Ion−Radical H-Bond in $H_4O_2^+$, J. Phys. Chem. A. 113 (2009) 4772–4779. doi:10.1021/jp811493s.

[155] S.A. Corcelli, J.A. Kelley, J.C. Tully, M.A. Johnson, Infrared Characterization of the Icosahedral Shell Closing in $Cl^-\cdot H_2O\cdot Ar_n$ ($1 \leq n \leq 13$) Clusters, J. Phys. Chem. A. 106 (2002) 4872–4879. doi:10.1021/jp013956k.

[156] S.G. Olesen, T.L. Guasco, J.R. Roscioli, M.A. Johnson, Tuning the intermolecular proton bond in the $H_5O_2^+$ 'Zundel ion' scaffold, Chem. Phys. Lett. 509 (2011) 89–95. doi:10.1016/J.CPLETT.2011.04.060.

[157] T.H. Dunning, Gaussian basis sets for use in correlated molecular calculations. I. The atoms boron through neon and hydrogen, J. Chem. Phys. 90 (1989) 1007–1023. doi:10.1063/1.456153.

[158] R.A. Kendall, T.H. Dunning, R.J. Harrison, Electron affinities of the first-row atoms revisited. Systematic basis sets and wave functions, J. Chem. Phys. 96 (1992) 6796–6806. doi:10.1063/1.462569.

[159] C.H. Lim, A.M. Holder, C.B. Musgrave, Mechanism of homogeneous reduction of CO_2 by pyridine: Proton relay in aqueous solvent and aromatic stabilization, J. Am. Chem. Soc. 135 (2013) 142–154. doi:10.1021/ja3064809.

[160] A.J. Morris, R.T. McGibbon, A.B. Bocarsly, Electrocatalytic Carbon Dioxide Activation: The Rate-Determining Step of Pyridinium-Catalyzed CO_2 Reduction, ChemSusChem. 4 (2011) 191–6. doi:10.1002/cssc.201000379.

[161] A.F. DeBlase, C.T. Wolke, G.H. Weddle, K.A. Archer, K.D. Jordan, J.T. Kelly, G.S. Tschumper, N.I. Hammer, M.A. Johnson, Water network-mediated, electron-induced proton transfer in $[C_5H_5N \cdot (H_2O)_n]^-$ clusters, J. Chem. Phys. 143 (2015). doi:10.1063/1.4931928.

[162] C. Desfrançois, H. Abdoul-Carime, J.-P. Schermann, Ground-state dipole-bound anions, Int. J. Mod. Phys. B. 10 (1996) 1339–1395. doi:10.1142/S0217979296000520.

[163] K.D. Jordan, F. Wang, Theory of dipole-bound anions., Annu. Rev. Phys. Chem. 54 (2003) 367–96. doi:10.1146/annurev.physchem.54.011002.103851.

[164] G. J. Nenner, I. Schultz, Temporary negative ions and electron affinities of benzene and N-heterocyclic molecules: pyridine, pyridazine, pyrimidine, pyrazine, and s-triazine, J. Chem. Phys. 62 (1975) 1747. doi:10.1063/1.430700.

[165] J.A. Pople, J.S. Binkley, R. Seeger, Theoretical models incorporating electron correlation, Int. J. Quantum Chem. 10 (1976) 1–19. doi:10.1002/qua.560100802.

[166] M.J. Frisch, M. Head-Gordon, J.A. Pople, A direct MP2 gradient method, Chem. Phys. Lett. 166 (1990) 275–280. doi:10.1016/0009-2614(90)80029-D.

[167] C.M. Aikens, S.P. Webb, R.L. Bell, G.D. Fletcher, M.W. Schmidt, M.S. Gordon, A derivation of the frozen-orbital unrestricted open-shell and restricted closed-shell second-order perturbation theory analytic gradient expressions, Theor. Chem. Accounts Theory, Comput. Model. (Theoretica Chim. Acta). 110 (2003) 233–253. doi:10.1007/s00214-003-0453-3.

[168] D. Jayatilaka, T.J. Lee, Open-shell coupled-cluster theory, J. Chem. Phys. 98 (1993) 9734–

9747. doi:10.1063/1.464352.

[169] J.F. Stanton, J. Gauss, Perturbative treatment of the similarity transformed Hamiltonian in equation-of-motion coupled-cluster approximations, J. Chem. Phys. 103 (1995) 1064. doi:10.1063/1.469817.

[170] P.G.S. J.F. Stanton, J. Gauss, M.E. Harding, and E. routines by A.V.M. and C. van W. with contributions from A.A. Auer, R.J. Bartlett, U. Benedikt, C. Berger, D.E. Bernholdt, Y.J. Bomble, L. Cheng, O. Christiansen, M. Heckert, O. Heun, C. Huber, T.-C. Jagau, D. Jonsson, J. Jusélius, K. Klein, W.J. Lauderdale, F. Lipparini, D.A. Matthews, CFOUR, a quantum chemical program package,. http://www.cfour.de.

[171] T.H. Dunning, Gaussian basis sets for use in correlated molecular calculations. I. The atoms boron through neon and hydrogen, J. Chem. Phys. 90 (1989) 1007–1023. doi:10.1063/1.456153.

[172] R.A. Kendall, T.H. Dunning, R.J. Harrison, Electron affinities of the first-row atoms revisited. Systematic basis sets and wave functions, J. Chem. Phys. 96 (1992) 6796. doi:10.1063/1.462569.

[173] V.P. Vysotskiy, L.S. Cederbaum, T. Sommerfeld, V.K. Voora, K.D. Jordan, Benchmark Calculations of the Energies for Binding Excess Electrons to Water Clusters, J. Chem. Theory Comput. 8 (2012) 893–900. doi:10.1021/ct200925x.

[174] V.P. Vysotskiy, L.S. Cederbaum, T. Sommerfeld, V.K. Voora, K.D. Jordan, Benchmark calculations of the energies for binding excess electrons to water clusters, J. Chem. Theory Comput. 8 (2012) 893–900. doi:10.1021/ct200925x.

[175] M.W. Schmidt, K.K. Baldridge, J.A. Boatz, S.T. Elbert, M.S. Gordon, J.H. Jensen, S. Koseki, N. Matsunaga, K.A. Nguyen, S. Su, T.L. Windus, M. Dupuis, J.A. Montgomery, General atomic and molecular electronic structure system, J. Comput. Chem. 14 (1993) 1347–1363. doi:10.1002/jcc.540141112.

[176] M.S. Gordon, M.W. Schmidt, Advances in electronic structure theory: GAMESS a decade later, in, in: G.E.S. Clifford E. Dykstra, Gernot Frenking, Kwang S. Kim (Ed.), Theory Appl. Comput. Chem. First Forty Years, Elsevier, Amsterdam, 2005: pp. 1167–1189. doi:http://dx.doi.org/10.1016/B978-044451719-7/50084-6.

[177] Y. Zhao, D.G. Truhlar, The M06 suite of density functionals for main group thermochemistry, thermochemical kinetics, noncovalent interactions, excited states, and transition elements: two new functionals and systematic testing of four M06-class functionals and 12 other function, Theor. Chem. Acc. 120 (2008) 215–241. doi:10.1007/s00214-007-0310-x.

[178] W.J. Hehre, R. Ditchfield, J.A. Pople, Self—Consistent Molecular Orbital Methods. XII. Further Extensions of Gaussian—Type Basis Sets for Use in Molecular Orbital Studies of Organic Molecules, J. Chem. Phys. 56 (1972) 2257. doi:10.1063/1.1677527.

[179] Y. Wang, X. Zhang, S. Lyapustina, M.M. Nilles, S. Xu, J.D. Graham, K.H. Bowen, J.T. Kelly, G.S. Tschumper, N.I. Hammer, The onset of electron-induced proton-transfer in hydrated azabenzene cluster anions., Phys. Chem. Chem. Phys. 18 (2015) 704–12. doi:10.1039/c5cp02746b.

[180] A.F. DeBlase, C.T. Wolke, G.H. Weddle, K.A. Archer, K.D. Jordan, J.T. Kelly, G.S. Tschumper, N.I. Hammer, M.A. Johnson, Water network-mediated, electron-induced proton transfer in $[C_5H_5N \cdot (H_2O)_n]^-$ clusters, J. Chem. Phys. 143 (2015) 144305. doi:10.1063/1.4931928.

[181] J.Q. Searcy, J.B. Fenn, Clustering of water on hydrated protons in a supersonic free jet expansion, J. Chem. Phys. 61 (1974) 5282–5288. doi:10.1063/1.1681876.

[182] M.P. Hodges, D.J. Wales, Global minima of protonated water clusters, (2000) 279–288.

[183] G.S. Fanourgakis, E. Aprà, S.S. Xantheas, High-level ab initio calculations for the four low-lying families of minima of $(H_2O)_{20}$. I. Estimates of MP2/CBS binding energies and comparison with empirical potentials, J. Chem. Phys. 121 (2004) 2655–2663. doi:10.1063/1.1767519.

[184] J.W. Shin, N.I. Hammer, E.G. Diken, M.A. Johnson, R.S. Walters, T.D. Jaeger, M.A. Duncan, R.A. Christie, K.D. Jordan, Infrared signature of structures associated with the $H^+(H_2O)_n$ (n = 6 to 27) clusters, Science (80-.). 304 (2004) 1137–1140. doi:10.1126/science.1096466.

[185] S.S. Iyengar, M.K. Petersen, T.J.F. Day, C.J. Burnham, V.E. Teige, G.A. Voth, The properties of ion-water clusters. I. the protonated 21-water cluster, J. Chem. Phys. 123 (2005). doi:10.1063/1.2007628.

[186] A. Khan, Theoretical studies of the clathrate structures of $(H_2O)_{20}$, $H^+(H_2O)_{20}$ and $H^+(H_2O)_{21}$, Chem. Phys. Lett. (1994). doi:10.1016/0009-2614(93)E1413-B.

[187] T.H. Choi, K.D. Jordan, Application of the SCC-DFTB method to $H^+(H_2O)_6$, $H^+(H_2O)_{21}$, and $H^+ (H_2O)_{22}$, J. Phys. Chem. B. (2010). doi:10.1021/jp912289e.

[188] M. Svanberg, J.B.C. Pettersson, Structure and Thermodynamics of $H^+(H_2O)_n$ (n = 9, 21, 40) Clusters between 0 and 300 K. A Monte Carlo Study, J. Phys. Chem. A. 102 (2002) 1865–1872. doi:10.1021/jp980052z.

[189] R.E. Kozack, P.C. Jordan, Structure of $H^+(H_2O)_n$ clusters near the magic number n = 21, J. Chem. Phys. 99 (1993) 2978–2984. doi:10.1063/1.465204.

[190] K. Mizuse, N. Mikami, A. Fujii, Infrared Spectra and Hydrogen-Bonded Network Structures of Large Protonated Water Clusters $H^+(H_2O)_n$ (n=20-200), Angew. Chemie - Int. Ed. 49 (2010) 10119–10122. doi:10.1002/anie.201003662.

[191] K. Mizuse, A. Fujii, Structural origin of the antimagic number in protonated water clusters $H^+(H_2O)_n$: Spectroscopic observation of the “missing” water molecule in the outermost

hydration shell, J. Phys. Chem. Lett. 2 (2011) 2130–2134. doi:10.1021/jz200996q.

[192] K. Mizuse, A. Fujii, Infrared spectroscopy of large protonated water clusters $H^+(H_2O)_{20-50}$ cooled by inert gas attachment, Chem. Phys. 419 (2013) 2–7. doi:10.1016/J.CHEMPHYS.2012.07.012.

[193] X. Yang, X. Zhang, A.W. Castleman, Kinetics and mechanism studies of large protonated water clusters, $H^+ (H_2O)_n$, n = 1-60, at thermal energy, Int. J. Mass Spectrom. Ion Process. 109 (1991) 339–354. doi:10.1016/0168-1176(91)85113-Z.

[194] S. Wei, Z. Shi, a W. Castleman, Mixed cluster ions as a structure probe: Experimental evidence for clathrate structure of $(H_2O)_{20}H^+$ and $(H_2O)_{21}H^+$, J. Chem. Phys. 94 (1991) 3268–3270. doi:10.1063/1.459796.

[195] C.C. Wu, C.K. Lin, H.C. Chang, J.C. Jiang, J.L. Kuo, M.L. Klein, Protonated clathrate cages enclosing neutral water molecules: $H^+(H_2O)_{21}$ and $H^+(H_2O)_{28}$, J. Chem. Phys. 122 (2005) 1–9. doi:10.1063/1.1843816.

[196] H. Wincel, E. Mereand, A.W.J. Castleman, Reactions of N_2O_5 with Protonated Water Clusters $H^+(H_2O)_n$, n = 3-30, J. Phys. Chem. 98 (1994) 8606–8610. doi:10.1021/j100086a003.

[197] Q.C. Nguyen, Yew-Soon Ong, J.L. Kuo, A hierarchical approach to study the thermal behavior of protonated water clusters $H^+(H_2O)$n, J. Chem. Theory Comput. 5 (2009) 2629–2639. doi:10.1021/ct900123d.

[198] K.A. Servage, J.A. Silveira, K.L. Fort, D.H. Russell, Evolution of hydrogen-bond networks in protonated water clusters $H^+(H_2O)_n$ (n = 1 to 120) studied by cryogenic ion mobility-mass spectrometry, J. Phys. Chem. Lett. 5 (2014) 1825–1830. doi:10.1021/jz500693k.

[199] T. Schindler, C. Berg, G. Niedner-Schatteburg, V.E. Bondybey, Reactions of water clusters $H^+(H_2O)_n$, n = 3−75, with diethyl ether, Chem. Phys. 201 (1995) 491–496. doi:10.1016/0301-0104(95)00288-X.

[200] M. Galvagno, D. Laria, J. Rodriguez, Structural and dynamical characteristics of mesoscopic $H^+[H_2O]_n$ clusters, J. Mol. Liq. 136 (2007) 317–322. doi:10.1016/J.MOLLIQ.2007.08.008.

[201] M.J. Ryding, R. Lzsak, P. Merlot, S. Reine, T. Helgaker, E. Uggerud, Geometry of the magic number $H^+(H_2O)_{21}$ water cluster by proxy, Phys. Chem. Chem. Phys. 17 (2015) 5466–5473. doi:10.1039/C4CP05246C.

[202] T. Kuś, V.F. Lotrich, A. Perera, R.J. Bartlett, An ab initio study of the $(H_2O)_{20}H^+$ and $(H_2O)_{21}H^+$ water clusters, J. Chem. Phys. 131 (2009) 104313. doi:10.1063/1.3231684.

[203] T. James, D.J. Wales, Protonated water clusters described by an empirical valence bond potential, J. Chem. Phys. 122 (2005) 1–11. doi:10.1063/1.1869987.

[204] T.S. Zwier, The Structure of Protonated Water Clusters, Science (80-.). 304 (2004).

[205] H. Yu, Q. Cui, The vibrational spectra of protonated water clusters: A benchmark for self-consistent-charge density-functional tight binding, J. Chem. Phys. 127 (2007) 234504. doi:10.1063/1.2806992.

[206] G.E. Douberly, A.M. Ricks, M.A. Duncan, Infrared Spectroscopy of Perdeuterated Protonated Water Clusters in the Vicinity of the Clathrate Cage, J. Phys. Chem. A. 113 (2009) 8449–8453. doi:10.1021/jp9052709.

[207] R. Kumar, R. a. Christie, K.D. Jordan, A Modified MSEVB force field for protonated water clusters, J. Phys. Chem. B. 113 (2009) 4111–4118. doi:10.1021/jp8066475.

[208] R. Ludwig, Protonated water clusters: The third dimension, ChemPhysChem. 5 (2004) 1495–1497. doi:10.1002/cphc.200400323.

[209] S.S. Iyengar, Further analysis of the dynamically averaged vibrational spectrum for the "magic" protonated 21-water cluster, J. Chem. Phys. 126 (2007) 2005–2007. doi:10.1063/1.2736694.

[210] M. Torrent-Sucarrat, J.M. Anglada, Anharmonicity and the Eigen-Zundel dilemma in the IR spectrum of the protonated 21 water cluster, J. Chem. Theory Comput. 7 (2011) 467–472. doi:10.1021/ct100692x.

[211] Z. Yang, S. Hua, W. Hua, S. Li, Structures of Neutral and Protonated Water Clusters Confined in Predesigned Hosts: A Quantum Mechanical/Molecular Mechanical Study, J. Phys. Chem. B. 115 (2011) 8249–8256. doi:10.1021/jp2030736.

[212] A. Lenz, L. Ojamäe, Theoretical IR spectra for water clusters $(H_2O)_n$ (n = 6-22, 28, 30) and identification of spectral contributions from different H-Bond conformations in gaseous and liquid water, J. Phys. Chem. A. 110 (2006) 13388–13393. doi:10.1021/jp066372x.

[213] M.W. Jurema, K.N. Kirschner, G.C. Shields, Modeling of magic water clusters $(H_2O)_{20}$ and $(H_2O)_{21}H^+$ with the PM3 quantum-mechanical method, J. Comput. Chem. 14 (1993) 1326–1332. doi:10.1002/jcc.540141109.

[214] U.W. Schmitt, G.A. Voth, Quantum properties of the excess proton in liquid water, Isr. J. Chem. 39 (1999) 483–492. doi:10.1002/ijch.199900053.

[215] Y. Wu, H. Chen, F. Wang, F. Paesani, G.A. Voth, An improved multistate empirical valence bond model for aqueous proton solvation and transport, J. Phys. Chem. B. 112 (2008) 467–482. doi:10.1021/jp076658h.

[216] A. Warshel, Computer simulations of enzymatic reactions., Curr. Opin. Struct. Biol. 2 (1992) 230–236. doi:10.1016/0959-440X(92)90151-V.

[217] J.A. Fournier, C.T. Wolke, M.A. Johnson, T.T. Odbadrakh, K.D. Jordan, S.M. Kathmann, S.S. Xantheas, Snapshots of Proton Accommodation at a Microscopic Water Surface:

Understanding the Vibrational Spectral Signatures of the Charge Defect in Cryogenically Cooled $H^+(H_2O)_{n=2-28}$ Clusters, J. Phys. Chem. A. 119 (2015) 9425–9440. doi:10.1021/acs.jpca.5b04355.

[218] S.A. Trygubenko, D.J. Wales, A doubly nudged elastic band method for finding transition states, J. Chem. Phys. 120 (2004) 2082–2094. doi:10.1063/1.1636455.

[219] S.S. Xantheas, Low-lying energy isomers and global minima of aqueous nanoclusters: Structures and spectroscopic features of the pentagonal dodecahedron $(H_2O)_{20}$ and $(H_3O)^+(H_2O)_{20}$, Can. J. Chem. Eng. 90 (2012) 843–851. doi:10.1002/cjce.21645.

[220] A.D. Becke, Density-fnnctional exchange-energy approximation with correct asymptotic behavior, 1988. https://journals.aps.org/pra/pdf/10.1103/PhysRevA.38.3098 (accessed May 16, 2019).

[221] A.D. Becke, Density-functional thermochemistry. III. The role of exact exchange, J. Chem. Phys. 98 (1993) 5648. doi:10.1063/1.464913.

[222] J. Nocedal, S. Wright, Numerical optimization, series in operations research and financial engineering, in: Springer, 2006. doi:10.1007/978-0-387-40065-5.

[223] M.J. Frisch, M. Head-Gordon, J.A. Pople, A direct MP2 gradient method, Chem. Phys. Lett. 166 (1990) 275–280. doi:10.1016/0009-2614(90)80029-D.

[224] M. Head-Gordon, J.A. Pople, M.J. Frisch, MP2 energy evaluation by direct methods, Chem. Phys. Lett. 153 (1988) 503–506. doi:10.1016/0009-2614(88)85250-3.

[225] M. Head-Gordon, T. Head-Gordon, Analytic MP2 frequencies without fifth-order storage. Theory and application to bifurcated hydrogen bonds in the water hexamer, Chem. Phys. Lett. 220 (1994) 122–128. doi:10.1016/0009-2614(94)00116-2.

[226] S. Sæbø, J. Almlöf, Avoiding the integral storage bottleneck in LCAO calculations of electron correlation, Chem. Phys. Lett. 154 (1989) 83–89. doi:10.1016/0009-2614(89)87442-1.

[227] B.R. Brooks, R.E. Bruccoleri, B.D. Olafson, D.J. States, S. Swaminathan, M. Karplus, CHARMM: A program for macromolecular energy, minimization, and dynamics calculations, J. Comput. Chem. 4 (1983) 187–217. doi:10.1002/jcc.540040211.

[228] E.W. Dijkstra, A note on two problems in connexion with graphs, Numer. Math. 1 (1959) 269–271. doi:10.1007/BF01386390.

[229] G. Zundel, H. Metzger, Energiebänder der tunnelnden Überschuß-Protonen in flüssigen Säuren. Eine IR-spektroskopische Untersuchung der Natur der Gruppierungen H5O2+, Zeitschrift Fur Phys. Chemie. 58 (1968) 225–245. doi:10.1524/zpch.1968.58.5_6.225.

[230] NIST Chemistry WebBook,. https://webbook.nist.gov/chemistry/ (accessed December 12, 2018).

[231] H. Okamoto, N. Kawasaki, Y. Kaji, Y. Kubozono, A. Fujiwara, M. Yamaji, Air-assisted High-performance Field-effect Transistor with Thin Films of Picene, J. Am. Chem. Soc. 130 (2008) 10470–10471. doi:10.1021/ja803291a.

[232] E.A. Silinsh, Organic Molecular Crystals, Springer Berlin Heidelberg, Berlin, Heidelberg, 1980. doi:10.1007/978-3-642-81464-8.

[233] R. Mitsuhashi, Y. Suzuki, Y. Yamanari, H. Mitamura, T. Kambe, N. Ikeda, H. Okamoto, A. Fujiwara, M. Yamaji, N. Kawasaki, Y. Maniwa, Y. Kubozono, Superconductivity in alkali-metal-doped picene, Nature. 464 (2010) 76–79. doi:10.1038/nature08859.

[234] Y. Kubozono, H. Goto, T. Jabuchi, T. Yokoya, T. Kambe, Y. Sakai, M. Izumi, L. Zheng, S. Hamao, H.L.T. Nguyen, M. Sakata, T. Kagayama, K. Shimizu, Superconductivity in aromatic hydrocarbons, Phys. C Supercond. Its Appl. 514 (2015) 199–205. doi:10.1016/J.PHYSC.2015.02.015.

[235] S. Heguri, M. Kobayashi, K. Tanigaki, Questioning the existence of superconducting potassium doped phases for aromatic hydrocarbons, Phys. Rev. B. 92 (2015) 014502. doi:10.1103/PhysRevB.92.014502.

[236] G. Giovannetti, M. Capone, Electronic correlation effects in superconducting picene from *ab initio* calculations, Phys. Rev. B. 83 (2011) 134508. doi:10.1103/PhysRevB.83.134508.

[237] K. Teranishi, X. He, Y. Sakai, M. Izumi, H. Goto, R. Eguchi, Y. Takabayashi, T. Kambe, Y. Kubozono, Observation of zero resistivity in K-doped picene, Phys. Rev. B - Condens. Matter Mater. Phys. 87 (2013) 60505. doi:10.1103/PhysRevB.87.060505.

[238] S. Heguri, M. Kobayashi, K. Tanigaki, Questioning the existence of superconducting potassium doped phases for aromatic hydrocarbons, Phys. Rev. B. 92 (2015) 014502. doi:10.1103/PhysRevB.92.014502.

[239] G.A. Artioli, L. Malavasi, Superconductivity in metal-intercalated aromatic hydrocarbons, J. Mater. Chem. C. 2 (2014) 1577. doi:10.1039/c3tc32326a.

[240] D. Hillesheim, K. Gofryk, A.S. Sefat, On the nature of filamentary superconductivity in metal-doped hydrocarbon organic materials, Nov. Supercond. Mater. 1 (2015). doi:10.1515/nsm-2015-0001.

[241] T. Dutta, S. Mazumdar, Theory of metal-intercalated phenacenes: Why molecular valence 3 is special, Phys. Rev. B. 89 (2014) 245129. doi:10.1103/PhysRevB.89.245129.

[242] S.S. Naghavi, M. Fabrizio, T. Qin, E. Tosatti, Electron-doped organics: Charge-disproportionate insulators and Hubbard-Fröhlich metals, Phys. Rev. B. 88 (2013) 115106. doi:10.1103/PhysRevB.88.115106.

[243] Y. Yoshida, H.-H. Yang, H.-S. Huang, S.-Y. Guan, S. Yanagisawa, T. Yokosuka, M.-T. Lin, W.-B. Su, C.-S. Chang, G. Hoffmann, Y. Hasegawa, Scanning tunneling microscopy/spectroscopy of picene thin films formed on Ag(111), J. Chem. Phys. 141

(2014) 114701. doi:10.1063/1.4894439.

[244] J.B. Neaton, M.S. Hybertsen, S.G. Louie, Renormalization of Molecular Electronic Levels at Metal-Molecule Interfaces, Phys. Rev. Lett. 97 (2006) 216405. doi:10.1103/PhysRevLett.97.216405.

[245] Y. Wang, R. Yamachika, A. Wachowiak, M. Grobis, K.H. Khoo, D.-H. Lee, S.G. Louie, M.F. Crommie, Novel Orientational Ordering and Reentrant Metallicity in $K_x C_{60}$ Monolayers for $3 \leq x \leq 5$, Phys. Rev. Lett. 99 (2007) 086402. doi:10.1103/PhysRevLett.99.086402.

[246] J. VandeVondele, M. Krack, F. Mohamed, M. Parrinello, T. Chassaing, J. Hutter, Quickstep: Fast and accurate density functional calculations using a mixed Gaussian and plane waves approach, Comput. Phys. Commun. 167 (2005) 103–128. doi:10.1016/j.cpc.2004.12.014.

[247] DFT with Hybrid Functionals. https://www.cp2k.org/_media/events:2015_cecam_tutorial:ling_hybrids.pdf (accessed November 23, 2018).

[248] J. VandeVondele, J. Hutter, Gaussian basis sets for accurate calculations on molecular systems in gas and condensed phases, J. Chem. Phys. 127 (2007) 114105. doi:10.1063/1.2770708.

[249] J.F. Stanton, Why CCSD(T) works: a different perspective, Chem. Phys. Lett. 281 (1997) 130–134. doi:10.1016/S0009-2614(97)01144-5.

[250] T.H. Dunning, Gaussian basis sets for use in correlated molecular calculations. I. The atoms boron through neon and hydrogen, J. Chem. Phys. 90 (1989) 1007. doi:10.1063/1.456153.

[251] M.F. Falcetta, K.D. Jordan, Assignments of the temporary anion states of the chloromethanes, J. Phys. Chem. 94 (1990) 5666–5669. doi:10.1021/j100378a012.

[252] R. Boschi, E. Clart, W. Schmidt, Photoelectron spectra of polynuclear aromatics. III. the effect of nonplanarity in sterically overcrowded aromatic hydrocarbons, J. Chem. Phys. 60 (1974) 4406–4418. doi:10.1063/1.1680919.

[253] C.A. Coulson, G.S. Rushbrooke, Note on the method of molecular orbitals, Math. Proc. Cambridge Philos. Soc. 36 (1940) 193. doi:10.1017/S0305004100017163.

[254] J. Fraxedas, S. García-Gil, S. Monturet, N. Lorente, I. Fernández-Torrente, K.J. Franke, J.I. Pascual, A. Vollmer, R.-P. Blum, N. Koch, P. Ordejón, Modulation of Surface Charge Transfer through Competing Long-Range Repulsive versus Short-Range Attractive Interactions, J. Phys. Chem. C. 115 (2011) 18640–18648. doi:10.1021/jp2050838.

[255] X. Crispin, V. Geskin, A. Crispin, J. Cornil, R. Lazzaroni, W.R. Salaneck, J.-L. Brédas, Characterization of the Interface Dipole at Organic/ Metal Interfaces, J. Am. Chem. Soc. 124 (2002) 8131–8141. doi:10.1021/ja025673r.

[256] D.B. Dougherty, P. Maksymovych, J. Lee, M. Feng, H. Petek, J.T. Yates, Tunneling spectroscopy of Stark-shifted image potential states on Cu and Au surfaces, Phys. Rev. B. 76 (2007) 125428. doi:10.1103/PhysRevB.76.125428.

[257] A. De, R. Ghosh, S. Roychowdhury, P. Roychowdhury, Structural analysis of picene, $C_{22}H_{14}$, Acta Crystallogr. Sect. C Cryst. Struct. Commun. 41 (1985) 907–909. doi:10.1107/s0108270185005959.

[258] Y. Yoshida, H.-H. Yang, H.-S. Huang, S.-Y. Guan, S. Yanagisawa, T. Yokosuka, M.-T. Lin, W.-B. Su, C.-S. Chang, G. Hoffmann, Y. Hasegawa, Scanning tunneling microscopy/spectroscopy of picene thin films formed on Ag(111), J. Chem. Phys. 141 (2014) 114701. doi:10.1063/1.4894439.

[259] K. Giesen, F. Hage, F.J. Himpsel, H.J. Riess, W. Steinmann, Binding energy of image-potential states: Dependence on crystal structure and material, Phys. Rev. B. 35 (1987) 971–974. doi:10.1103/PhysRevB.35.971.

[260] A. Ruff, M. Sing, R. Claessen, H. Lee, M. Tomić, H.O. Jeschke, R. Valentí, Absence of metallicity in K-doped picene: Importance of electronic correlations, Phys. Rev. Lett. 110 (2013). doi:10.1103/PhysRevLett.110.216403.

[261] S. Heguri, M. Kobayashi, K. Tanigaki, Questioning the existence of superconducting potassium doped phases for aromatic hydrocarbons, Phys. Rev. B. 92 (2015) 14502. doi:10.1103/PhysRevB.92.014502.

[262] A. Ruff, M. Sing, R. Claessen, H. Lee, M. Tomić, H.O. Jeschke, R. Valentí, Absence of metallicity in K-doped picene: Importance of electronic correlations, Phys. Rev. Lett. 110 (2013) 216403. doi:10.1103/PhysRevLett.110.216403.

[263] D. Heskett, Correlation of alkali metal-induced work function changes on semiconductor and metal surfaces, J. Vac. Sci. Technol. B Microelectron. Nanom. Struct. 7 (1989) 915. doi:10.1116/1.584580.

[264] S. Laurent, k-means++ - File Exchange - MATLAB Central,. https://www.mathworks.com/matlabcentral/fileexchange/28804-k-means (accessed April 30, 2019).

[265] E.P. Wigner, On the Behavior of Cross Sections Near Thresholds, Phys. Rev. 73 (1948) 1002–1009. doi:10.1103/PhysRev.73.1002.